Towards a Mechanistic Model for Stress Corrosion Cracking in Nuclear Fuel Elements

Vers un Modèle Mécanique de la Fissuration par Corrosion dans les Éléments de Combustible Nucléaire

A Thesis Submitted to the
Division of Graduate Studies of the Royal Military College of Canada
by

Andrew Oussoren, B. Eng.

In Partial Fulfillment of the
Requirements for the Degree of

Master of Applied Science

April 2015

ACKNOWLEDGEMENTS

I wish to acknowledge the following people without whom this work would not have been possible.

I would like to thank my supervisors Dr. Chan and Dr. Wowk for their guidance and advice. I also want to acknowledge the former students of Dr. Lewis, on whose work this model is built, especially Dr. Andrew Prudil for his explanations of the FAST model and advice and assistance with COMSOL.

Thanks to my fellow students at RMCC for their support along the way. Thanks also to the Canadian Nuclear Safety Commission for providing the opportunity to participate in their co-op program, which has been a valuable and enriching experience.

I would like to acknowledge the generous financial support of Cameco Corporation and the Natural Science and Engineering Research Council under grant CRDPJ#415247-11.

Finally, thank you to my wife Rebecca for putting up with me being a student again.

ABSTRACT

Oussoren, Andrew, MASc. Candidate (Nuclear Engineering). Royal Military College of Canada (RMCC), April, 2013. Towards a Mechanistic Model for Stress Corrosion Cracking in Nuclear Fuel Elements. Supervisors: Dr. Paul Chan and Dr. Diane Wowk

The sheath of a nuclear fuel element is an important barrier to prevent fission product release in nuclear reactors. During increases in power the fuel sheath can be compromised due to iodine-induced Stress Corrosion Cracking (SCC). A mechanistic model of this process would assist in better characterizing operating margins and informing future changes in fuel manufacturing and design.

This thesis develops a new model for SCC in nuclear fuel using the COMSOL finite element analysis platform. It builds on the model of Kleczek and Lewis, previously developed at Royal Military College of Canada (RMCC). The fuel performance model FAST has been integrated into the model to provide mechanical analysis of the fuel sheath. The iodine transport methodology of the Kleczek/Lewis model has been modified to utilize the more robust diffusion model in FAST, and a surface multiplier term has been derived to equate predicted iodine release rates with measured release rate from in-reactor sweep gas tests.

A fracture mechanics analysis has been implemented using threshold stress intensity values and crack growth rates reported in literature. A correlation to predict crack initiation has been derived by mechanical analysis of a database of power histories with known SCC defects. This correlation is based on the change in sheath hoop strain during a power ramp and is shown to be more accurate at discerning failure vs. non-failure than the correlations used in the previous Kleczek/Lewis model.

Failure time prediction of the model is compared against power ramp test FFO-104 performed at the NRX reactor. Under prediction of failure time is explored in a series of sensitivity studies to suggest areas for further development. Together, these model improvements represent a step forward in the mechanistic modelling of SCC in nuclear fuel.

Keywords: stress corrosion cracking, nuclear fuel, CANDU fuel, fracture mechanics, COMSOL

RÉSUMÉ

Oussoren, Andrew, M.Sc.A. Candidat (Génie nucléaire). Collège militaire royal du Canada (CMRC), avril, 2015.

Vers un Modèle Mécanique de la Fissuration par Corrosion dans les Éléments de Combustible Nucléaire. Directeurs: Dr. Paul Chan et Dr. Diane Wowk.

La gaine d'un élément de combustible nucléaire constitue une barrière importante pour empêcher le relâchement des produits de fission dans le réacteur. Durant des hausses de la puissance, la gaine du combustible peut être affectée par la fissuration par corrosion induite par l'iode (FCII). Un modèle mécanique de ce processus contribuerait à une meilleure caractérisation des marges opérationnelles et à suggérer des changements futurs dans la fabrication et la conception du combustible.

Cette thèse développe un nouveau modèle de la fissuration par corrosion dans le combustible nucléaire et utilise la plateforme COMSOL pour l'analyse par éléments finis. Ce modèle est basé sur le modèle de fissuration par corrosion induite par l'iode de Kleczek et Lewis, développé dans le passé au CMRC. Le code de performance du combustible FAST a été intégré au modèle afin de d'effectuer l'analyse mécanique de la gaine du combustible. La méthodologie du transport de l'iode dans le modèle FCII a été modifiée afin d'utiliser le modèle de diffusion dans FAST qui est plus robuste, et un terme de multiplication de surface a été dérivé pour rendre les taux de relâchement de l'iode prédits égaux aux taux de relâchement mesurés à partir de tests de balayage de gaz dans le réacteur.

On a mis en œuvre une analyse de la mécanique de fissuration utilisant des valeurs des seuils de l'intensité de la contrainte mécanique et des taux de croissance des fissures rapportés dans la littérature. Une analyse mécanique d'une base de données d'historiques de puissance ayant des défaillances connues dues aux fissures par corrosion a permis d'établir une corrélation pouvant prédire le début de la fissuration. Cette corrélation est basée sur le changement de contrainte circonférentielle lors d'une montée

en puissance et a été démontrée comme étant plus précise à discerner les défaillances des non-défaillances que les corrélations utilisées dans le modèle FCII précédent.

On a comparé le temps de défaillance prédit par le modèle à celui du test de montée en puissance FFO-104. La sous-prédiction du temps de défaillance est explorée dans une série d'études de sensitivité afin de suggérer des domaines pour développement futur. Ensemble, ces améliorations au modèle représentent un pas en avant pour la modélisation mécanique de la fissuration par corrosion dans le combustible nucléaire.

Mots-clefs: Fissuration par corrosion, combustible nucléaire, combustible CANDU, mécanique de fissuration, COMSOL.

TABLE OF CONTENTS

LIST OF TABLES

LIST OF FIGURES

LIST OF ABBREVIATIONS

AECL	Atomic Energy of Canada Limited
CANDU	CANadian DUeterium reactor
DHC	Delayed Hydride Cracking
EPRI	Electric Power Research Institute
FAST	Fuel and Sheath Modelling Tool
IST	Industry Standard Toolset
LZC	Liquid Zone Controller
NOC	Normal Operating Conditions
NPGS	Nuclear Power Generating Station
NRU	National Research Universal
NRX	National Research eXperimental
ODE	Ordinary Differential Equation
PDE	Partial Differential Equation
RMCC	Royal Military College of Canada
SCC	Stress Corrosion Cracking
SEM	Scanning Electron Microscope
PIE	Post Irradiation Examination
PRAISE	Pipe Reliability Analysis Including Seismic Events

LIST OF SYMBOLS

A_{burnup}	burnup correction factor to surface multiplier
A_{Na}	atomic weight of sodium
B	burnup
C^0_v	vacancy concentration of unirradiated UO_2
C_i	fuel grain concentration of isotope i
$C_{gap,i}$	gap concentration of isotope i
C_{Na}	concentration of sodium impurity in the CANLUB
$C_{surf,i}$	surface concentration of isotope i
$C_{surf,T}$	total iodine concentration on surface
D	diffusion coefficient
D_{AB}	binary diffusion coefficient in the gap
$D_{athermal}$	diffusion coefficient due to athermal processes
D_{irr}	diffusion coefficient due to irradiation
D_0	single atom diffusion coefficient for a full density UO_2 crystal
$D_{thermal}$,	diffusion coefficient due to thermal processes
E	Young's modulus
F	geometric factor
F_v	volumetric fission rate
H_0	uniform loading weighting factor
H_1	linear loading weighting factor
H_2	quadratic loading weighting factor
H_3	cubic loading weighting factor
J_i	flux of fission products onto grain boundary
K	Strength coefficient
K_I	stress intensity factor
K_{IC}	fracture toughness
K_{ISCC}	model 1 critical stress intensity for SCC
M_{absorb}	gap absorption term
M_{CsI}	molar mass of CsI
M_{He}	molar mass of helium
M_{I2}	molar mass of I_2
M_{react}	reaction rate multiplier term
M_{recoil}	radiolysis multiplier term
M_{surf}	surface multiplier term
M_U	molar mass of natural uranium
M_{Zr}	molar mass of zirconium
N_A	Avogadro's number
P	linear power
P_{fg}	volumetric fission gas production rate
P_i	isotopic production term
P_{max}	final power at power ramp

Q	crack shape term
$\mathfrak{R}/B$	release to birth ratio
R_{in}	inner radius of a cylinder
R_B	average radius of the intragranular pores
$R_{crack,i}$	rate of isotope i reaching crack site
$R_{crack,T}$	total rate of iodine reaching crack site
$R_{element,Xe138}$	release rate to element for Xe-138 in fission gas benchmarking study
R_g	ideal gas constant
$R_{gb,i}$	volumetric release rate
$R_{gap,i}$	release rate to gap per unit length for isotope i
R_I	release rate for all isotopes to gap
$R_{I,T}$	cumulative iodine released through radiolysis
$R_{measured,\ Xe138}$	measure release rate per element from sweep gas test
R_{rec}	release rate of recoil fission products from element surface
$R_{surf,i}$	release rate to fuel surface for isotope i
R_{Zr}	zirconium mass removal rate at crack site
SA	surface area fuel stack
T	temperature
T_g	temperature of gap gas
U	apparent activation energy divided by the ideal gas constant
V_{crack}	volume of intergranular crack
Y_i	fission yield for isotope i
Z_0	average range of the impact of a fission spike
Z_n	average number of sites available for recombination around defect
a_c	COMSOL ODE absorption coefficient
a/c	depth to width ratio of crack
a_{crack}	total crack length
$a_{crack,TG}$	length of transgranular portion of crack
$a_{crack,IG}$	length of intergranular portion of crack
b'	intergranular resolution rate
c	COMSOL ODE diffusion coefficient
d_a	COMSOL ODE damping coefficient
dE/dx	energy deposition per unit path length
da/dt	transgranular crack growth rate
e	COMSOL ODE mass coefficient
f	COMSOL ODE source term
g_a	trapping rate
g_r	grain radius
l_f	average distance travelled by a fission fragment in the fuel
l_e	element length
n	strain hardening exponent
n_{crack}	number of active crack sites
p	pressure

r_{out}	outer radius of a cylinder
r_{pellet}	radius of fuel pellet
$r_{sheath\_initial}$	initial inside sheath position
t	current time
t_{CANLUB}	thickness of CANLUB
t_{dwell}	power ramp dwell time
t_{ramp}	time at start of power ramp
t_{sheath}	sheath thickness
u	radial position
v_v	vacancy jump frequency
w	width of the crack
x_{CsI}	thickness of CsI surface deposit
y_{ff}	fission fragment yield
α	COMSOL ODE conservative flux convection coefficient
α_{fgb}	number of fission gas bubbles which are nucleated by each fission event
β	COMSOL ODE convection coefficient
γ	COMSOL ODE conservative flux source term
$\Delta\varepsilon_{\phi}$	change in hoop strain over the power ramp
$\Delta\varepsilon_{\phi c}$	critical change in hoop strain for SCC initiation
ΔP	size of power ramp
ε_{ϕ}	hoop strain
$\varepsilon_{\phi,c}$	critical hoop strain
$\varepsilon_{\phi,lowT}$	low temperature creep
$\varepsilon_{\phi,irr}$	irradiation creep
ϕ_{Fflux}	fast neutron flux
λ_i	isotopic decay constant
η	normalized fuel grain radius
μ	fission fragment average range in UO_2
μ_s	sink strength for crystallographic point defect
π	pi ≈ 3.141
ρ_{CANLUB}	density of CANLUB
ρ_{CsI}	density of CsI
ρ_{STPUO2}	density of UO_2 at STP
ρ_{Zr}	density of zirconium
σ_{AB}	average collision distance in binary diffusion
σ_y	yield stress
σ_{ϕ}	hoop stress
$\sigma_{\phi,c}$	critical hoop stress
$\sigma_{\phi,FAST}$	hoop stress predicted by FAST (uncorrected for yield stress)
ω_{Na}	measured content by weight of sodium in CANLUB
Ω	atomic volume

Ω_{AB}	collision integral

1 INTRODUCTION

Nuclear power is ideally suited for providing reliable, carbon-free base-load electricity for power grids. In 2014, 18 operating Nuclear Power Generating Stations (NPGSs) in Ontario accounted for 38% of installed generating capacity and produced 62% of the electricity consumed in the province [1].

All NPGSs operating in Canada are of the CANDU design. The basic design of a CANDU reactor involves a calandria vessel containing heavy water moderator at low temperature and pressure, penetrated by pressure tubes which contain natural uranium dioxide fuel bundles and pressurized heavy water coolant. Heat generated by fission in the fuel is transported by the coolant to a set of steam generators, which create high pressure steam. This steam is directed to a series of turbines, which are coupled to a generator to produce electricity. A simplified diagram of a CANDU station is illustrated in Figure 1.

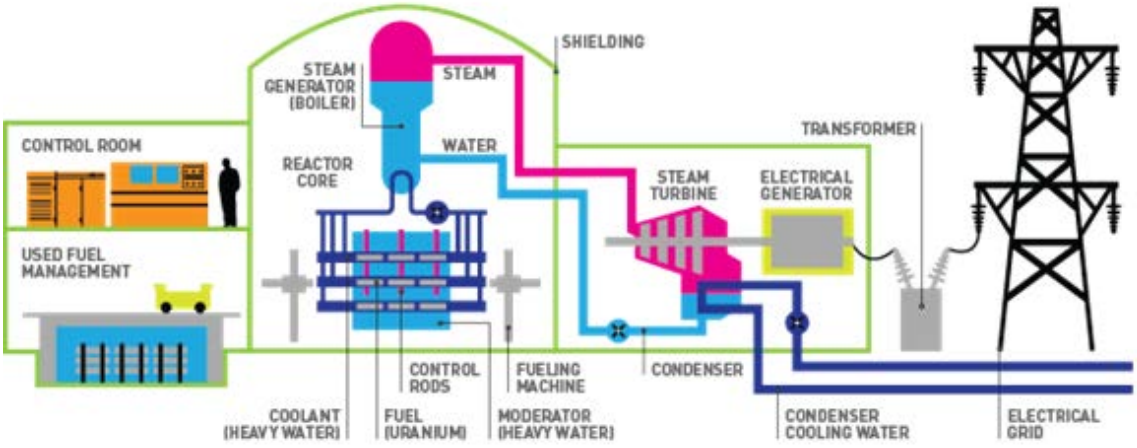

Figure 1: Schematic of a CANDU power plant, reproduced from the Canadian Nuclear Association [2]

A major advantage of the CANDU reactor design is the ability to utilise natural uranium dioxide as fuel without the need for enrichment, which is both expensive and politically undesirable due to proliferation concerns. CANDU reactors are also able to

refuel online, eliminating the need to shutdown the reactor for refuelling, as is typical of Light Water Reactors (LWRs).

CANDU fuel consists of pellets of uranium dioxide arranged in stacks approximately 0.5 m long. The stack of fuel pellets is encased in a sheath composed of Zircaloy-4, which separates the fuel from the surrounding coolant and contains the radioactive elements produced by the fissioning of uranium. The fuel pellets and sheath together are referred to as a fuel element. The elements are arranged in bundles of 37 (28 for the Pickering reactors) and held together by two end plates. An illustration of a Pickering fuel bundle is shown in Figure 2.

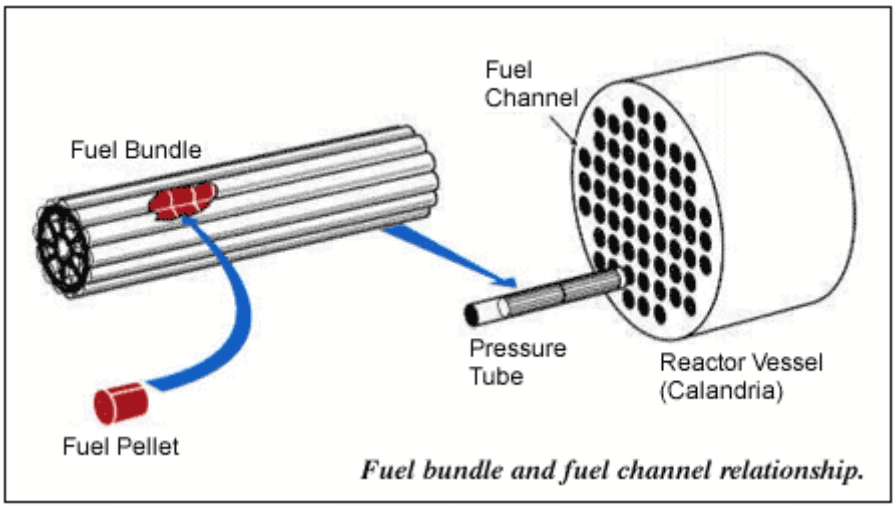

Figure 2: CANDU fuel pellet, bundle and fuel channel [3]

Nuclear safety is based on the concept of defence-in-depth, where there exists multiple barriers to prevent release of radioactive fission products into the environment. The fuel sheath, as a barrier to fission product release, is an integral component of the safe operation of an NPGS, and the prevention of fuel sheath failure during accident scenarios is an important safety goal. However it is also possible for sheath failures to occur during Normal Operating Conditions (NOC). The resulting contamination of the primary side coolant leads to increased dose to workers as well as undesirable changes in coolant chemistry. Additionally, radiological contamination beyond regulatory limits

necessitates reactor shutdown, which represents an enormous economic penalty to reactor operators.

The most significant causes of fuel failures in CANDU reactors during NOC are listed below.

1) *Debris fretting* is caused by solid particles in the coolant, which may be introduced during plant construction, maintenance work or by failure of another component. This debris is carried in the coolant at high speeds and has the potential to impact and damage the fuel sheath, which can lead to sheath failure [4]. Debris fretting can be controlled through a foreign material exclusion program, which involves the use of temporary coverings on system openings and establishing controlled work areas with a material control log for entering and exiting the area [5].

2) *Manufacturing defects* in fuel can lead to fuel failures. In CANDU fuels the most common site of manufacturing related defects is in the element end cap weld. Improper weld geometry or an incomplete weld can cause high levels of stress in the end cap, leading to rupture. These defects are minimised through rigorous quality assurance standards in fuel fabrication [4].

3) *Delay Hydrogen Cracking* (DHC) typically occurs near the end cap welds, as high stresses and lower temperatures may increase diffusion of hydrogen to this location. DHC has been minimised by strict control over the total hydrogen content of the sheath, pellets and fill gas during manufacturing [6]. The weld geometry is also being improved to reduce stress concentration.

4) *Stress Corrosion Cracking* (SCC) is a failure mode resulting from a combination of stress, a susceptible material, sufficient time, and a corrodent. SCC defects may occur in fuels undergoing increases in power level (power ramps). Fuels with higher burnup (more energy released per unit mass) are more susceptible to SCC than fresh fuels [7]. SCC is mitigated in CANDU reactors by

limiting the exposure of high burnup bundles to power ramps and through a protective coating called CANLUB on the inside of the fuel sheath.

The focus of this thesis is to build a model for the prediction of SCC in nuclear fuels. There has been ongoing work at the Royal Military College of Canada (RMCC) to develop tools to predict the behaviour of nuclear fuel and fission products in reactor. Two efforts in particular form an excellent basis to develop a model of the SCC process:

- Fuel And Sheath modelling Tool (FAST), a fuel performance code developed by A. Prudil [8] [9] [10]
- ISCC, an iodine production and transport model developed by M. Kleczek and B. Lewis [11] [12]

These models are both developed on the COMSOL Multiphysics platform. COMSOL is a versatile finite element solver which allows the user to input custom Ordinary and Partial Differential Equations (ODE's and PDE's) for simultaneous solution. In the past, most codes used in nuclear safety analysis have been custom built, typically in the FORTRAN programming language, which requires the developer to exert a significant effort in developing efficient and robust numerical solving algorithms. By providing a generic equation solver, COMSOL allows the researcher to focus on model development while still leveraging the latest developments in numerical solving techniques as well as rich pre-and-post processing tools.

Utilising the COMSOL platform, this thesis presents a methodology for prediction of SCC in nuclear fuel. Building on previous models developed at RMCC, it includes more of the physical processes and parameters which are believed to contribute to SCC.

2 BACKGROUND

SCC is a process by which failure of a metal can occur under smaller loads than would be expected based on mechanical considerations alone. When an SCC susceptible metal is placed in an environment with a corrodent while under load, corrosion can weaken the metal in regions of high stress, such as in the vicinity of a defect or small crack, which causes cracking to propagate. There are four factors required for SCC [13]:

1) A susceptible material

2) A corrosive environment

3) Mechanical stress

4) Time

SCC is a concern for the design of many engineering structures including gas pipelines, boilers and turbines [13].

An accepted model of the process of SCC is the ‘film rupture model’. In this process a passive surface film, usually an oxide, protects an underlying metal from a corrosive environment. An applied strain causes the film to rupture, exposing the underlying metal to corrosion. Film rupture will occur preferentially in regions of strain concentration such as a small crack or flaw. Weakening of chemical bonds and removal of the metal due to corrosion weakens the material in the region of the flaw, allowing the crack to grow at stress levels lower than the bulk strength of the material. [14]

Under certain circumstances the Zircaloy-4 fuel sheath of an operating nuclear fuel element can meet all the above criteria for SCC.

1) Zircaloy-4 is composed primarily of zirconium, which is susceptible to corrosion by iodine.

2) Iodine is produced in the fuel as a product of fission and builds up as the fuel is irradiated. While the bulk of gaseous fission products remain trapped in the UO_2

fuel matrix, a portion diffuses out to the fuel-sheath gap, which is then available to participate in an SCC process.

3) Conditions in the reactor can place significant stresses on the sheath, both due to the external pressure from the coolant and the internal pressure of the fuel pellet.

4) In a CANDU reactor, fuel typically remains in the reactor for a period of 12-20 months, allowing ample time for SCC to occur

A thin oxide layer is grown on the inner surface of the sheath during the manufacturing process. This layer is believed to act as a barrier to iodine reaching the surface of the Zircaloy-4 sheath. [12]

SCC can occur in nuclear fuel following an increase in the operating power of the fuel, called a power ramp. When the fuel power increases there is a corresponding increase in the temperature of pellets. This causes the pellets to expand outward into the sheath, generating tensile stresses which can create the conditions necessary to break the oxide layer and allow SCC to occur.

In CANDU reactors power ramps may arise from three scenarios:

1) *Refuelling*: CANDU fuel bundles are arranged horizontally in the core, and are inserted and removed by fueling machines located on each end of the fuel channel. The axial power profile of the core is not uniform; power is higher in the centre of the core than at the peripheries. Refuelling is performed online in CANDU reactors, which causes bundles to be shifted to regions with different power levels. For example, a bundle which is initially operating in the first position (in the periphery) may later be shifted through the centre of the core, where it may experience a large power ramp [7].

2) *Localized power fluctuations*: Within a CANDU reactor there are two regulating devices which can affect local power. The liquid zone controllers (LZC) are columns of light water (H_2O) which are used to make fine adjustments

to reactor power. Due to these adjustments, a bundle placed next to a LZC experiences frequent small power variations not felt by other bundles in the core. This represents a series of small power ramps [15]. The core also contains absorber rods which reduce regional power levels and are used to flatten the power profile of the core. If the absorbers are removed from the core to increase power, bundles adjacent to absorbers experience a larger power increase than the other bundles in the core. Local power increases can also occur due to refuelling of adjacent fuel channels.

3) *Rise in overall reactor power*: Where a reactor is in a shutdown state or operating at reduced power, a return to full power results in a small and controlled power ramp of every bundle in the reactor.

Power ramp fuel failures were observed early in the development of both CANDU and Boiling Water Reactors (BWRs). Outside of the CANDU industry the phenomenon is referred to as Pellet Cladding Interaction (PCI) failure. In BWRs, PCI failures were observed to occur following movement of control blades, which results in localized power ramps. PCI failures have been less common in Pressurized Water Reactors (PWRs) due to the use of dissolved boron in the coolant as the primary means of reactivity control, which limits the need for control rod movement [16].

A great deal of research was conducted in order to understand the process of power ramp failures and to develop mitigation strategies. These strategies included changes to both operating practices and fuel design. Operational changes have involved limits to the size and speed of power ramps in order to limit the exposure of high burnup fuel to large changes in power [17]. While these measures reduce the risk of SCC failures they also constrain reactor performance, particularly the ability to operate nuclear reactors in a load-following mode, which requires daily power ramps to adjust reactor output to match electricity demand.

On the fuel design side, the BWR industry pursued the development of ‘liner claddings’ which employ a thin layer pure zirconium on the inner surface of the cladding.

This softer inner layer reduces the stresses associated with pellet fragment interaction with the cladding and absorbs the bulk of the radiation dose arising from recoiling fission products from the fuel surface. The effectiveness of liner claddings in mitigating PCI failures has been shown to be almost the same as that of CANLUB coated fuels discussed below [17].

In the CANDU industry, in addition to limits to power maneuvers described above, mitigation strategies for SCC included changes to refuelling patterns by increasing the number of bundles moved in a single fueling run. This ensures that only fresh bundles are placed in high power positions in the core and prevents high burnup fuel from experiencing large sustained power ramps [7]. On the fuel design side, a graphite coating was applied to the inside of the fuel sheath. This coating was intended to act as a lubricant between the fuel pellets and the sheath to reduce stresses, therefore it was named CANLUB.

These strategies have been effective in virtually eliminating SCC occurrence in CANDU reactors. However, restrictions on power maneuvers limit operational flexibility, and changes in fuel manufacturing may have unintentional negative impacts on the SCC susceptibility of fuel. In the future it is also desirable to develop advanced CANDU fuel capable of higher burnups than present mitigation strategies allow. A sound mechanistic model would enable engineers to better understand SCC in nuclear fuel and characterize the risk of fuel failure.

3 CURRENT MODELLING CAPABILITIES

Early methods for predicting SCC in CANDU fuels relied heavily upon empirical models based on previous SCC failures in operating reactors. These empirical models are still in use by industry and have been effective in mitigating SCC in current reactor operations. Due to the limited range of applicability of these empirical models, subsequent efforts have been made to develop more mechanistic models of SCC, although their use has so far been restricted to the domain of research. Below is a summary of the main developments in the CANDU industry.

FUELOGRAMS/FULOMO: After the first major occurrence of SCC power ramp fuel defects at the Douglas Point and Pickering A reactors in the early 1970's the CANDU industry developed models to predict fuel failure [7]. These define an operating envelope of power ramp size (ΔP), and maximum ramped power (P_{max}) for CANDU fuel based on fuel burnup, and predict a probability of fuel failure if fuel is operated outside that envelope. Two different models were developed: an empirically based model called FUELOGRAMS used by Atomic Energy of Canada Limited (AECL), and FULOMO, a model derived from statistical considerations used at Ontario Hydro. Similar models were developed by the BWR industry [17].

CAFÉ: In response to the need for a predictive tool for CANLUB coated fuel, daSilva developed the first CAnlub Fulomo Extended (CAFÉ) model in 1986 [18]. This initial formulation of CAFÉ did not find widespread use. However, a power ramp fuel defect experience at Pickering A in 1988 provided important new data on the performance of CANLUB coated fuel elements. This data was used to revise the CAFÉ formulation and a new tool for the calculation of power ramp fuel defect probabilities for CANLUB fuel elements was issued in 1990 [19]. Figure 3 shows an example of a defect probability curve from CAFÉ.

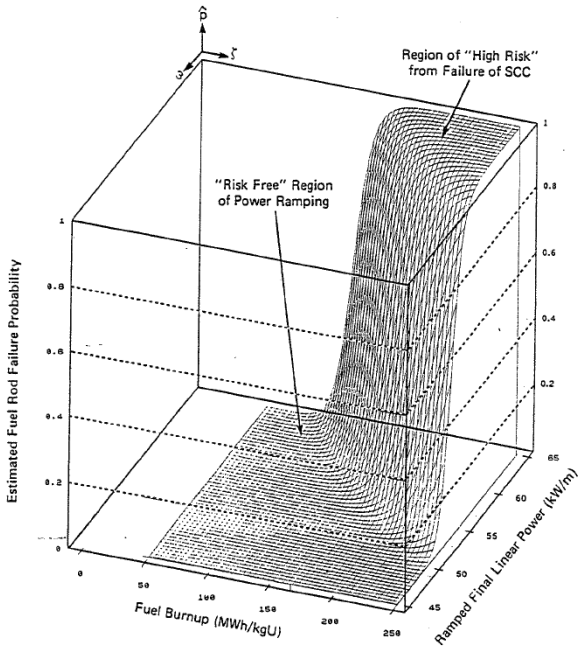

Figure 3: A failure probability curve generated by CAFÉ as a function of final linear power [18]

INTEGRITY: This semi-mechanistic code was developed by AECL in the 1990's in an effort to extend the applicability of the existing SCC correlations to burnup levels beyond the range of available power reactor data. It uses the industry standard tool (IST) code ELESTRES, a 1D/2D finite difference fuel performance code, to calculate fission gas release and fuel strain, and the FEAST code to determine stress, strain and work density in the sheath. A 'damage index' is calculated based on iodine concentration and sheath work density. A large database of SCC power histories was evaluated to determine a failure probability for a given index value [20]. While SCC prediction is based on fuel mechanical parameters instead of power levels, no attempt is made to explicitly model the cracking process. The INTEGRITY code has found limited use in industry. A similar damage index methodology has been used in Light Water Reactor (LWR) codes such as the FALCON fuel performance model developed by the Electric Power Research Institute (EPRI) [21].

Kleczek/Lewis ISCC model: This model was developed at RMCC by M. Kleczek and B. Lewis to predict SCC failure in fuel elements [11] [12]. Focusing on the thermochemistry of iodine, it models iodine production and diffusion in the fuel based on an empirical diffusion coefficient, and predicts iodine release to the fuel-sheath gap after a power ramp through radiolysis of CsI on the fuel surface. The released iodine diffuses towards a single crack site located at the centre of the element, and failure time is predicted based on mass removal of zirconium as ZrI_4. Owing to the many simplifications in the model, failure times are significantly under predicted; however this model represents an important step towards developing a mechanistic model of the behaviour of SCC in nuclear fuel elements. It forms the basis of the iodine transport methodology developed in the present model. The Kleczek/Lewis model does not explicitly calculate the mechanical conditions of the fuel sheath; the prediction of crack initiation is based on the FUELOGRAM correlations described above. Therefore as a predictive tool this model produces similar results as existing methods.

4 MOTIVATION AND THESIS GOAL

While incidents of SCC in CANDU reactors are rare today, a mechanistic model could offer several advantages over the current empirically-based models. First, it could support station operations by better characterizing safety margins, potentially allowing for greater flexibility in power maneuvers and extending bundle burnup compared to existing correlations. Second, it could help engineers ensure that future changes to fuel design or manufacturing supply chain do not adversely affect fuel performance by directly modelling the impact of the proposed changes. Third, it may be adapted to model advanced fuel designs such as DUPIC, MOX, thorium-based fuels and slightly enriched fuel bundles for which the current SCC correlations may not be relevant.

The goal of this thesis is to develop a more mechanistic model for prediction of SCC in nuclear fuel, including threshold mechanical parameters for crack initiation and the modelling of the physical processes involved in crack growth. This model will represent an important step in the development towards a fully mechanistic model for prediction of SCC in nuclear fuels.

The model builds on previous work at RMCC. Sheath mechanical performance values are derived from the FAST model. FAST is a robust finite element fuel performance model developed at RMCC which uses fewer simplifying assumptions compared to current industry codes such as ELESTRES. The Kleczek/Lewis ISCC model (see previous chapter) forms the basis of an iodine transport model to predict iodine availability in the fuel-sheath gap. This methodology has been significantly modified to utilize the more theoretically rigorous fission gas diffusion model employed in the FAST code; this new model for iodine releasewas benchmarked against in-reactor sweep gas tests of operating fuel elements.

The initiation of SCC at power ramps is predicted based on sheath mechanical response. Several different parameters suggested in literature have been evaluated to determine threshold criterion for SCC initiation by benchmarking against a power history database of known SCC failure cases. This represents a more generic SCC threshold

criterion than the FUELOGRAM correlations used in the Kleczek/Lewis model, which are based on power ramp characteristics.

The growth of an SCC crack is modeled based on intergranular and transgranular growth mechanisms. Intergranular growth is predicted by mass removal of iodine diffusing to the crack site. A fracture mechanics analysis of the crack has been implemented to predict the transition to transgranular growth based on threshold values and growth rates reported in literature. Failure time prediction is benchmarked against power ramp test FFO-104 which had a well-defined SCC failure time of 20 minutes. A series of multiplying parameters were implemented to perform sensitivity studies investigating the impact of the different simplifying assumptions in the model. The results of these studies provide a metric for identifying the relative impact of different assumptions, and suggest focus areas for future development.

5 MODEL DESCRIPTION

This chapter presents the methodology and equations used to develop the model. The model is implemented using the finite element analysis software COMSOL. Full details of the model implementation are given in Chapter 7.

The finite element model consists of three components. The first is a 2D axi-symmetric geometry representing the pellet-sheath domain. Most of the equations in the FAST code are solved on this geometry. The second component is a 2-D rectangular geometry representing idealized fuel grain radius in the y-axis and pellet radial position in the x-axis; fission product diffusion to grain boundaries is solved on this domain. The third geometry is a 1D representation of one half length of the fuel element; iodine diffusion in the gap to a crack site is solved on this domain. The three component geometries are illustrated in Figure 4.

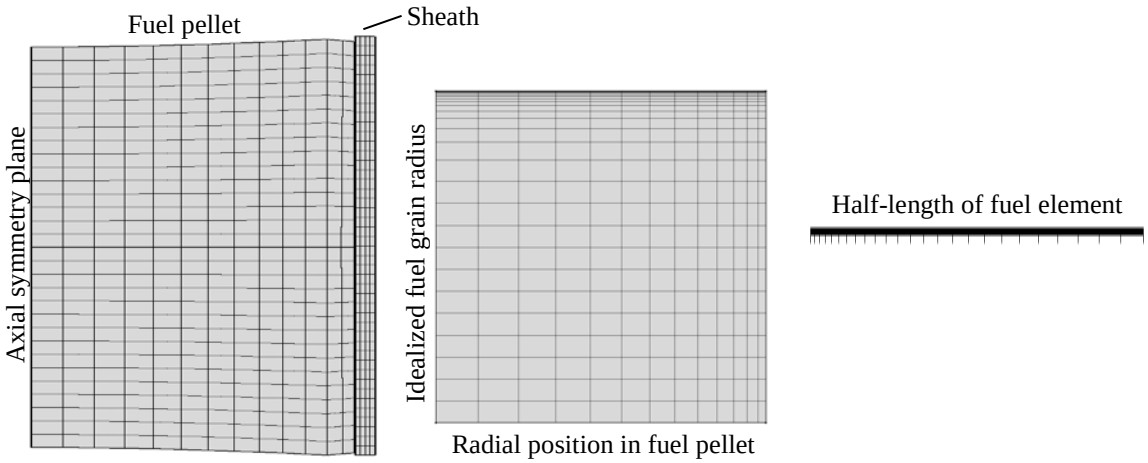

Figure 4: Component geometries 1, 2 and 3 for the finite element implementation of the model, showing solution mesh. Geometries are not to scale

A flow chart of the model is presented in Figure 5. The critical step is the crack initiation step, which determines if SCC will occur based on the mechanical conditions in the sheath required to crack the oxide layer. If SCC initiation is predicted the model

calculates a time to failure based on intergranular and transgranular crack growth, which will be described in Section 5.5.

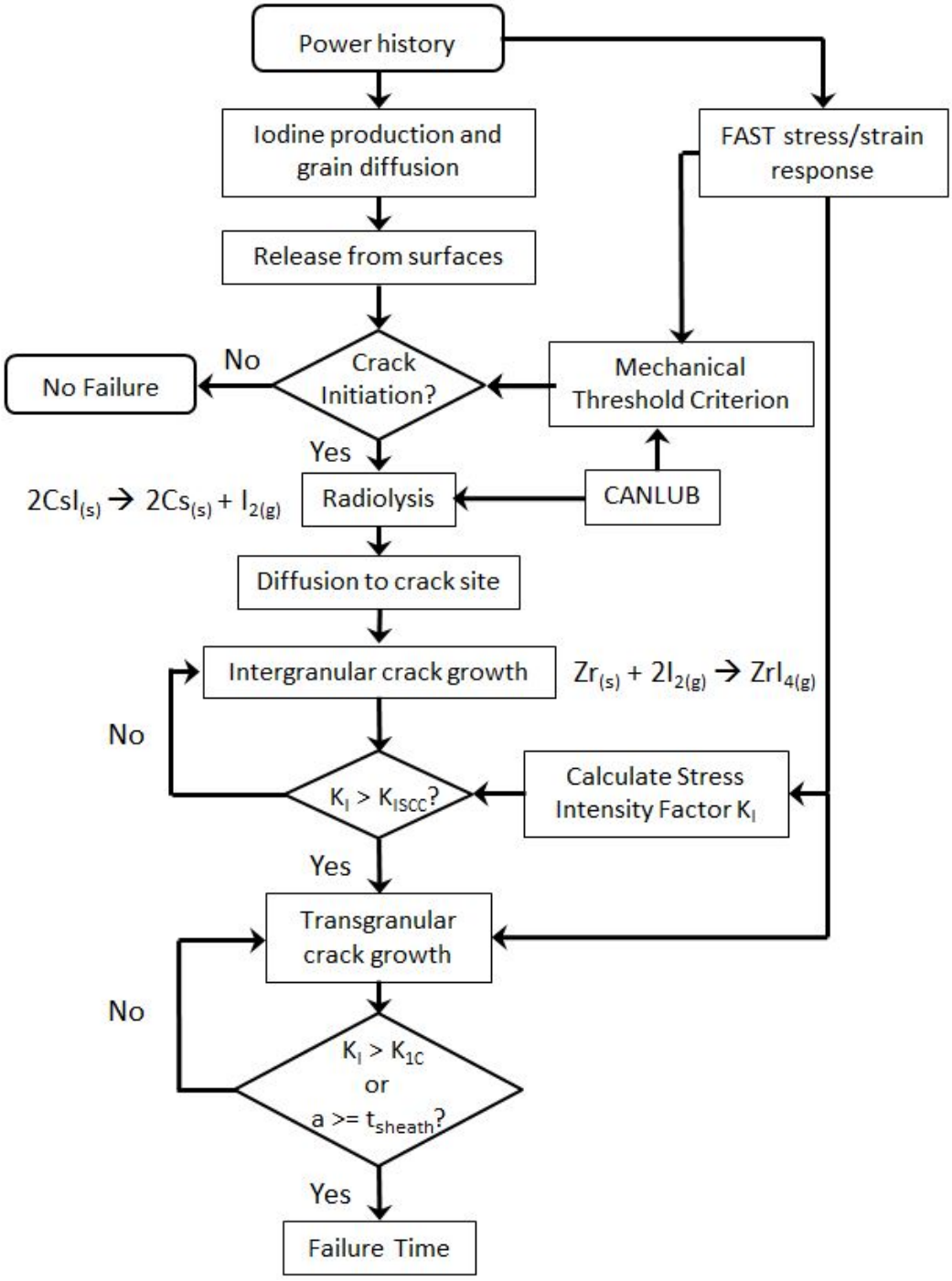

Figure 5: Flow chart of the model, K_I = stress intensity factor, K_{ISCC} = SCC threshold stress intensity K_{IC} = fracture toughness, a = crack length, t_{sheath} = sheath thickness

5.1 IODINE DIFFUSION AND RELEASE TO GAP

Several isotopes of iodine are produced by fission in nuclear fuel. As irradiation progresses iodine builds up in the UO_2 fuel and diffuses to the grain boundaries, where it collects in small intergranular bubbles. Under normal operating conditions the bulk of this gas remains within the UO_2 matrix. The portion of iodine which is produced near the fuel pellet surfaces is released directly to the fuel-sheath gap where it is available to participate in SCC. To predict the concentration of iodine in the gap region, the model calculates production of iodine in the fuel grains, its diffusion to the grain boundaries, then predicts the portion which is released directly to the fuel surface, and uses a radiolysis model for the release from a surface layer of cesium iodide. These equations are solved in component 2 of the finite element model.

5.1.1 IODINE PRODUCTION AND DIFFUSION IN FUEL GRAIN

The model for fission product iodine diffusion is based on the methodology used in the FAST code, which models a dispersed intragranular gas migrating towards the grain boundary. This model assumes that fission products are produced uniformly within an idealized spherical UO_2 grain of radius g_r. A Fickian diffusion model, which assumes that flux is proportional to the gradient of concentration, gives the concentration C_i (atoms m^{-3}) of a gaseous fission product isotope within this idealised grain as:

$$\frac{\partial C_i}{\partial t} = -D\nabla^2 C_i + P_i - \lambda_i C_i \qquad (1)$$

where ∇^2 is the Laplacian operator in 2-D spherical coordinates ($\frac{1}{r^2}\frac{\partial}{\partial r} r^2 \frac{\partial}{\partial r}$), D is the diffusion coefficient ($m^2\ s^{-1}$), $P_i = Y_i F_v$ is the volumetric fission gas production rate (atoms $m^{-3}\ s^{-1}$), λ_i is the isotopic decay constant (s^{-1}), Y_i is the fission yield for a given isotope (atoms/fission) and F_v is the volumetric fission rate (fissions $m^{-3}\ s^{-1}$).

The surface of the sphere is assumed to be a perfect sink, and fission products reaching the surface ($r = g_r$) are released to the grain boundary region. Fresh fuel contains no fission product; therefore the initial concentration is zero. These assumptions are expressed by the following boundary and initial conditions:

$$C_i(r = g_r, t) = 0 \tag{2}$$

$$C_i(r, 0) = 0 \tag{3}$$

The flux of fission products from the sphere onto the grain boundary, J_i (atoms m^{-2} s^{-1}) is proportional to the concentration gradient at the surface:

$$J_i = -D \frac{\partial C_i}{\partial r}\Big]_{r=g_r} \tag{4}$$

The rate of escape of fission products from the sphere is then given by integrating over the surface area of the sphere:

$$\int_0^{r=g_r} J_i da = -4\pi g_r^2 D \frac{\partial C_i}{\partial r}\Big]_{r=g_r} \tag{5}$$

where da is a unit area of the sphere's outer surface.

A volumetric release rate $R_{gb,v}$ (atoms $m^{-3}s^{-1}$) is then obtained by dividing Equation (5) by the volume of the fuel grain:

$$R_{gb,i} = -\frac{4\pi g_r^2}{\frac{4}{3}\pi g_r^3} D \frac{\partial C_i}{\partial r}\Big]_{r=g_r} = -\frac{3}{g_r} D \frac{\partial C_i}{\partial r}\Big]_{r=g_r} \tag{6}$$

Implementation of the diffusion model in this form is complicated by the fact that the idealized grain radius is variable with time and radial position in the fuel pellet. To solve the equation in this form would require a solution domain with changing geometry. To simplify the implementation, the radius is normalized using the factor $\eta = r/g_r$ and Equation (1) becomes:

$$\eta^2 g_r^2 \frac{\partial C_i}{\partial t} = \frac{\partial}{\partial \eta}\left(-D\eta^2 \frac{\partial C_i}{\partial \eta}\right) + \eta^2 g_r^2 P_i - \eta^2 g_r^2 \lambda_i \mathrm{C} \tag{7}$$

Equation (6) becomes:

$$\left.\frac{\partial C_i}{\partial r}\right]_{r=gr} = \frac{1}{g_r}\left.\frac{\partial C_i}{\partial \eta}\right]_{\eta=1} \tag{8}$$

$$R_{gb,i}(t) = -\frac{3}{g_r^2} D \left.\frac{\partial C_i}{\partial \eta}\right]_{\eta=1} \tag{9}$$

These equations are implemented in the model on a rectangular geometry shown in Figure 4, where the y-axis represents normalized radial position in the fuel grain, η, and the x-axis represents radial position in the fuel pellet. This allows the model to account for the change in the fission rate F_v, grain radius g_r and diffusion coefficient D with radial position in the fuel pellet.

There are several isotopes of iodine produced in fission of U-235. These include one stable isotope, I-129, and six principle unstable isotopes, I-127 and I-131 through 135. In the Kleczek/Lewis model all seven of these isotopes are tracked individually. However due to short half-lives the relative concentrations of some of these isotopes are very small. In order to reduce complexity and run time in the present model only I-127, I-129, I-131 and I-133 are tracked, which account for more than 99% of all iodine for most power histories analysed.

The diffusion coefficient *D* follows the methodology of Turnbull *et al.* [22] [23] [24] and White and Tucker [25]. The diffusion coefficient is based on xenon, which exhibits similar diffusion characteristics to iodine [26]. It is calculated as the sum of three separate models for the effects of thermal processes, irradiation-induced vacancies and athermal processes. Details on the calculation of *D* are presented in Appendix A.

5.1.2 Release from Fuel Surfaces

The fission gas release model in FAST was developed to predict bulk fission gas release from the fuel; this is used to assess the impact of fission gas on internal pressure in the fuel element and the heat transfer coefficient of the pellet-to-sheath gap. Bulk fission gas release is typically encountered in high burnup and/or high temperature conditions, therefore this model will predict no fission gas release for lower burnup conditions.

While the bulk of fission gas produced in the UO_2 fuel will remain in the fuel matrix or on the internal grain boundaries for NOC, fission gas produced in fuel grains at or near the surface of the pellet may be released directly to the gap. This portion of release is generally quite small and not necessarily significant for determining fission gas pressure, however it is important for predicting iodine availability to cause SCC.

Factors which impact the amount of fission gas released to the gap include:

1. Pellet surface area. While a new fuel pellet has a well-defined surface area based on its manufactured geometry, in the reactor thermal gradients resulting from fission heating and the low thermal conductivity of UO_2 causes the pellet to crack, increasing the surface area which is open to the pellet-sheath gap. The pattern of cracking has complicated dependency on power history, texture, local lattice defects and more, which makes the deterministic prediction of pellet cracking a complex problem [27].
2. Depth into the pellet surface which releases gaseous fission products directly to the gap, as opposed intergranular bubble sites.

Rather than attempting to mechanistically model the individual factors listed above, their combined effect can be derived by benchmarking the fission gas release model against release data from in-reactor elements. The difference between the predicted and measured release rates are captured in a surface multiplier term M_{surf}, so that the release rate to the fuel surface $R_{surf,i}$ (atoms m^{-2} s^{-1}) is defined as:

$$R_{surf,i} = M_{surf}\, R_{gb,i}\Big]_{r=pellet\ radius} \tag{10}$$

M_{surf} has units of meters. The surface multiplier is derived based on experimental results of sweep gas tests where the fission gas release from the fuel surface was measured in-reactor. The derivation is presented in Section 6.1. It is a function of power P (kW m^{-1}) and burnup B (MWh kg(U)$^{-1}$) and is defined as:

$$M_{surf} = A_{burnup} e^{(-10.0754 - 0.05P + 0.0012\,P^2)} \tag{11}$$

where:

$$A_{burnup} = 1.0, \qquad B \leq 40.8$$

$$A_{burnup} = 1.0 + \frac{(B - 40.8)}{(72.4 - 40.8)} 2.82, \qquad 40.8 < B < 72.4$$

$$A_{burnup} = 3.82, \qquad B \geq 72.4$$

The iodine released from the fuel surface is assumed to accumulate in a surface deposit of CsI as described in the next section. The total surface concentration of iodine $C_{surf,,i}$ (atoms m^{-2}) is given by the following equation

$$\frac{\partial C_{surf,i}}{\partial t} = R_{surf,i} - \lambda_i C_{surf,i} \tag{12}$$

Fresh fuel contains no fission products, therefore the initial condition for Equation (12) is:

$$C_{surf,i}(t = 0) = 0 \quad (13)$$

5.1.3 RADIOLYSIS MODEL FOR IODINE RELEASE TO THE GAP

Sweep gas tests performed on in-reactor elements do not detect fission product iodine directly [26]. Iodine is believed to deposit on surfaces within the fuel element. The release of iodine from the fuel surface is predicted based on the radiolysis methodology of the Kleczek/Lewis model [11].

Cesium is another fission product which is produced in nuclear fuel in much larger quantities than iodine. Cesium reacts with iodine to produce the very thermos-chemically stable cesium iodide. Based on thermochemical considerations alone all iodine escaping to the gap region would be expected to be thermodynamically unavailable (i.e., 'locked up' in the form of CsI) [28]. This iodine may be released by the impact of recoiling fission products, which provide sufficient energy to break apart the CsI molecule, resulting in "free" iodine being released to the gap [29].

In the model it is assumed that, before a power ramp, the gap inventory of iodine accumulates as a surface deposit of CsI. Post-ramp, this iodine can be released when recoiling fission products break apart the CsI molecule.

To determine the thickness of the surface CsI deposit, the total iodine concentration in the element, $C_{surf,T}$ (atoms m^{-2}), is calculated by summing the concentrations of individual iodine isotopes:

$$C_{surf,T}(t) = \sum_i C_{surf,i}\,(t) - C_{Na} - \frac{R_{I,T}}{2\pi r_{pellet} l_e} \quad (14)$$

where C_{Na} (atoms m^{-2}) is the concentration of sodium impurity in the CANLUB layer. The sodium impurity in CANLUB is proposed to react with and immobilise a portion of the iodine at the fuel-sheath interface (in a similar manner to CsI) [12]. The effects of

CANLUB are discussed further in Section 6.5. The cumulative iodine release through radiolysis, $R_{I,T}$ (atoms), is subtracted from the surface concentration, as released iodine is assumed not to re-depositing into the CsI layer.

The thickness x_{CsI} (m) of the CsI deposit is then determined based on the mass and density of CsI [12]:

$$x_{CsI} = \frac{C_{surf,T} M_{CsI}}{\rho_{CsI} N_A} \tag{15}$$

where M_{CsI} = 259.8 (g mol^{-1}) is the molar mass of CsI, ρ_{CsI} 4500 (kg m^{-3}) is the density of CsI and N_A (atoms mol^{-1}) is Avogadro's number.

Release of iodine from the CsI layer is assumed to occur through collision by fission fragments. The model for release rate of recoil fission fragments from an element's surface, R_{rec} (particles s^{-1}), is developed by Lewis [30] and has been adapted to the volumetric fission rate F_v predicted by FAST [12]:

$$R_{rec} = \frac{1}{4} \mu \, SA \, F_v y_{ff} \tag{16}$$

where μ = 7.7 μm is the fission fragment average range in UO_2, SA = surface area fuel stack (m^2), F_v is the volumetric fission rate evaluated at the fuel surface (fissions m^{-3}), and y_{ff} is fission fragment yield (2 per fission).

The radiolysis model predicts iodine release based on the energy deposition per unit path length dE/dx = 460eV Å^{-1}. This is obtained by Stopping Range of Ions in Matter (SRIM) analysis for fission fragments in CsI for 'average' light and heavy fission product, details of which are given in Lewis *et al.* [12]. The release rate of iodine from the fuel surface, R_I (atoms s^{-1}) is given as:

$$R_I = R_{rec} Y_I \frac{dE}{dx} x_{CsI} \quad (17)$$

where Y_I = 0.230 atoms eV^{-1} $particle^{-1}$ is the energy required to break apart one CsI molecule.

The cumulative iodine release from the surface, $R_{I,T}$ (atoms), is evaluated by integrating the iodine release rate over time as shown in Equation (18). This value is subtracted from the total iodine on the fuel surface in Equation (14) to reflect the loss of iodine with radiolysis.

$$R_{I.T} = \int_{t=0}^{t} R_I \, dt \quad (18)$$

The model assumes no radiolysis release before the power ramp and therefore a zero initial gap concentration. As there is no active crack site before the power ramp, iodine released by radiolysis would be expected to eventually redeposit on fuel surfaces. At the power ramp, if the mechanical conditions for crack initiation are met, iodine released from the surface through radiolysis may diffuse to a crack site to participate in SCC. Modelling of diffusion of iodine within the gap is described in Section 5.5.1.

5.2 STRESS/STRAIN

The fuel sheath is exposed to significant mechanical forces during operation. Upon initial insertion in the reactor, the fuel sheath is compressed into contact with the fuel pellets by external pressure of the coolant, generating compressive stresses in the sheath. Heat generation from fission then causes the fuel pellets to expand, pressing outward resulting in a tensile hoop stress in the sheath. The large thermal gradient in the fuel causes the pellet to crack and to develop an “hourglass” shape, shown in Figure 6,

generating stress concentrations at the circumferential ridges between pellets and at the edges of pellet fragments [31].

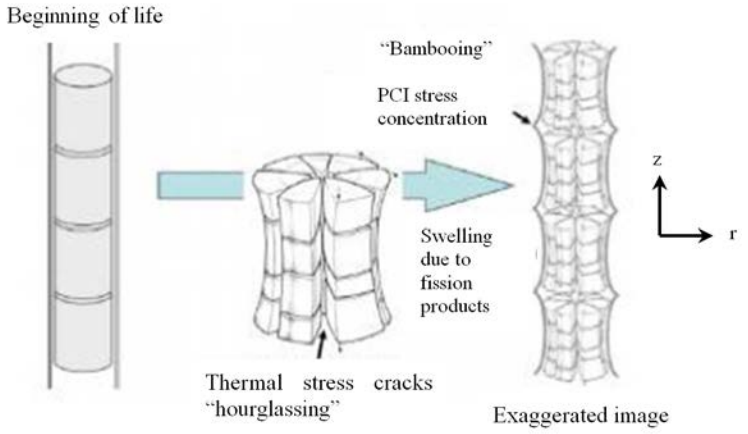

Figure 6: Illustration of bambooing effect of pellet swelling [31]

As irradiation progresses the fuel undergoes densification as the porosity decreases, which causes the pellet to shrink. As irradiation continues, swelling due to the accumulation of fission products causes the pellet to increase in size again. An example of a radial displacement profile for a fuel pellet during a constant power irradiation is shown in Figure 7.

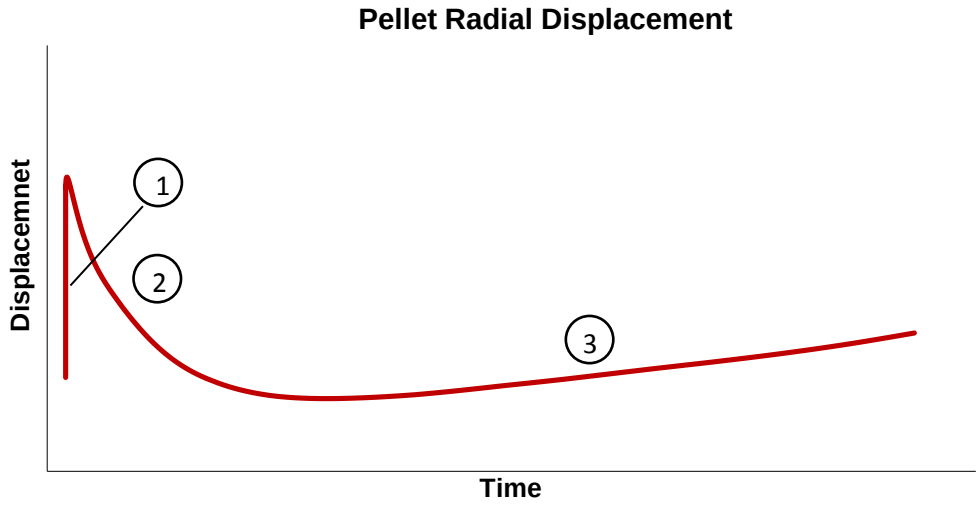

Figure 7: A sample pellet radial displacement plot from FAST showing the impacts of 1) thermal expansion, 2) densification, and 3) swelling

At a power ramp, the increased heat generation in the pellet causes further thermal expansion, which increases hoop strain in the sheath.

The sheath mechanical response to reactor conditions is predicted by the FAST model. The equations for FAST are solved in component 1 of the finite element model, with the exception of the bulk fission gas release equations, which are solved in component 2. A full description of the equations, correlations and implementation methodology of the model is too lengthy to repeat here; the reader is referred to Prudil *et al.* [9] , [10]. The relevant phenomena included in the model and their impact on the fuel-sheath system are summarised below.

- *Heat transfer,* including generation of heat in the fuel pellet, conduction in the pellet, conduction and radiative heat transfer across the fuel-sheath gap, conduction through the sheath and convective heat transfer to the coolant at the sheath outside surface. Heat transfer determines the temperature of the pellet and the magnitude of thermal expansion. The heat generation model includes the effects of neutron flux depression across the pellet.
- *Contact* between the pellet and sheath using a penalty method, which allows a small interpenetration of the contacting surfaces and then applies an artificial contact pressure to push them apart
- *Thermal expansion* of the pellet, which increases the pellet volume.
- *Fuel densification* resulting from high temperature, pressure, and irradiation which reduces the porosity of the fuel and results in a decrease in pellet volume.
- *Gaseous and solid fission product swelling,* which results from the production of two fission products in a volume which previously contained a single uranium atom. This effect increases the volume of the fuel pellet, particularly at high burnups.
- *Bulk fission gas release,* resulting from saturation of grain boundaries. Bulk fission gas release occurs at high burnups and/or high temperatures. The modelling of iodine discussed in Section 5.1 is built on the same framework as the fission gas model in FAST.

- *Internal gas pressure* which increases sheath hoop and axial strain.
- *External sheath oxidation* where at high temperature the external surface of the sheath reacts with the coolant water. This reduces the thickness of the sheath and increases the fuel temperature due to both direct heating and the increased thermal resistance of the oxide layer. For CANDU fuel external sheath oxidation is only expected to be significant during transient conditions.
- *Sheath creep*, a form of time and temperature dependant plastic flow which occurs at stresses below yield stress. In FAST, creep is separated into low temperature creep, irradiation creep and high temperature creep. The first two impact operations in NOC while the latter is encountered in transient conditions. As sheath expansion in constrained, creep strain results in a reduction of elastic strain over time, an effect known as stress relaxation. Low temperature creep is defined as [9]:

$$\frac{\partial \varepsilon_{\phi,lowT}}{\partial t} = 5x10^{-23}\sigma_\phi^2\left(3.47x10^{-23}\frac{\sigma_\phi^3}{|\sigma_\phi|}\left(\frac{-U}{T}\right) - \varepsilon_\phi\right)exp\left(\frac{-U}{T}\right) \qquad (19)$$

where σ_ϕ is the hoop stress (Pa), ε_ϕ is the fractional creep strain, T is temperature in Kelvin and U is the apparent activation energy divided by the ideal gas constant given by [9]:

$$U = 212.7 - 0.5324T + 1.17889x10^{-4}T^2 + 3.3486x10^{-7}T^3 \qquad (20)$$

Irradiation creep is defined as [9]:

$$\frac{\partial \varepsilon_{\phi,ir}}{\partial t} = \frac{2.2x10^{-7}\sigma_\phi exp\left(\frac{-5000}{T}\right)\phi_{Fflux}^{0.65}}{T^7} \qquad (21)$$

where $\phi_{Fflux}$is the fast neutron flux ($m^{-2}\,s^{-1}$)

An important limitation in the FAST model is the model of plastic deformation during power ramps. The only plastic deformation calculated by the model is the creep strain; the plastic deformation which would occur due to exceeding the yield stress is not modelled. The implication is that, at a power ramp when the expanding pellet pushes outward on the sheath, FAST interprets the increased strain as almost purely elastic, which can result in non-physically high stress levels (in excess of the yield or the tensile strength) for a short period of time. In reality stresses in excess of the yield stress would be relaxed by plastic deformation.

In the long term the impact of this simplification is limited; because the creep rate is dependent on stress, very high stress levels cause very high rates of creep, which eventually reduce the elastic strain to more reasonable levels. However for short term behaviour, such as immediately following a power ramp, non-physically high values for stress may be calculated. This is particularly significant for the calculation of the stress intensity factor in Section 5.6.2.

A simple correction is implemented in the model whereby the sheath stress is capped at the yield stress, which is given by Equation (22), derived from MATPRO [32]:

$$\sigma_y = \left(\frac{K}{E^n}\right)^{\left(\frac{1}{1-n}\right)} \tag{22}$$

where K is the strength coefficient, E is Young's modulus (Pa), and n is the strain hardening exponent assuming fully anneal, isotropic material (n ranges from of 0.09881 at T = 290 °C to 0.17345 at T = 2100 °C). The yield stress is temperature dependant; a table of yield strength values for Zircaloy-4 is presented in Appendix D. The hoop stress in the model, $\sigma_\phi$is then defined as:

$$\sigma_\phi = \min\left(\sigma_y, \sigma_{\phi,FAST}\right) \tag{23}$$

where $\sigma_{\phi,FAST}$ is the hoop stress as calculated by FAST.

Using this model the stress may rise to the yield stress σ_y and will remain at that value until creep reduces the value of $\sigma_{\phi,FAST}$ to below the yield stress.

Compared to the real case, where the sheath stress would rise slightly above the yield stress and then begin to relax fairly quickly, the present model results in a constant stress at the yield stress which requires a longer time before stress relaxation occurs. This results in higher predicted stress intensity and faster crack growth, which is conservative.

The sample plot in Figure 8 shows the development of the total, elastic and creep hoop strains following a power ramp. The elastic strain rises rapidly following the ramp. Over time the creep strain increases which decreases the elastic strain.

The validation plot in Figure 9 compares post irradiation sheath strain measurements for several fuel elements against the predictions of FAST, along with predictions by the ELESTRES and ELESIM codes. The discrepancy between model predictions and experimental measurements is evidence of difficulty of modeling the complex behaviour of nuclear fuel. However, while FAST tends to under predict sheath strain for these cases, it shows consistently better agreement with experimental results compared to the other codes [8]. This provides confidence in the calculations of sheath mechanical parameters in the model.

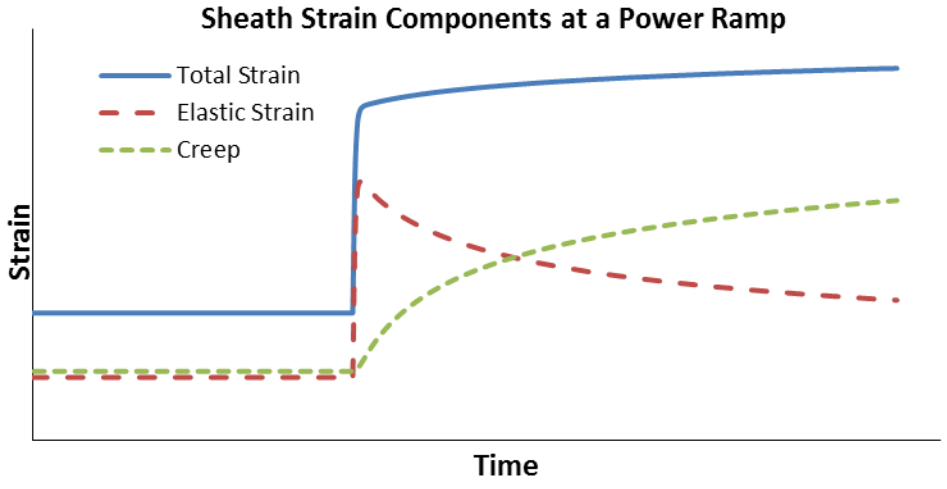

Figure 8: Components of sheath hoop strain for a sample power ramp, showing relaxation of elastic strain due to creep

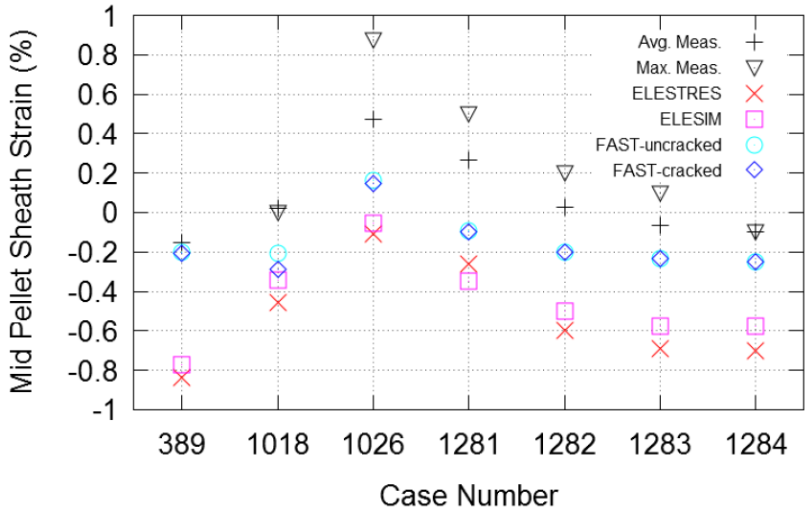

Figure 9: FAST sheath strain predictions compared to measurements and prediction by other codes [8]

5.3 Crack Initiation

The critical step in the film rupture model of SCC is the cracking of the protective oxide layer, which exposes the underlying metal to corrosion. Despite a large body of research, there is not complete agreement in literature as to which mechanical parameters are critical to SCC initiation. Based on power reactor evidence and laboratory experiments various authors have suggested different crack initiation criterion. A description and analysis of these parameters is presented in Section 6.2.

Based on the aforementioned analysis, the total change in hoop strain over the power ramp, $\Delta\varepsilon_\phi$, was selected as the threshold parameter to determine crack initiation. The model calculates the change in strain during the power ramp as the integral of the strain rate between the ramp time and the end of the dwell time:

$$\Delta\varepsilon_\phi = \int_{t_{ramp}}^{t_{ramp}+t_{dwell}} \frac{\partial\varepsilon_\phi}{\partial t}\, dt \tag{24}$$

where t_{ramp} is the time at the start of the ramp and t_{dwell} is the dwell time at power. If $\Delta\varepsilon_{\phi}$ exceeds the critical value $\Delta\varepsilon_{\phi c}$, crack initiation is predicted and the model proceeds to calculate a time to failure.

The presence of CANLUB influences the threshold change in strain at which SCC failures are observed. Therefore two threshold curves are developed in Section 6.4, one for CANLUB and one for non-CANLUB:

For non-CANLUB: $$\Delta\varepsilon_{\phi,c} = -1.06\text{x}10^{-1} + \frac{67.7}{B} \quad (25)$$

For CANLUB: $$\Delta\varepsilon_{\phi,c} = 3.12x10^{-1} + \frac{50.3}{B} \quad (26)$$

where B is fuel burnup in MWh kg(U)$^{-1}$.

When evaluated against the database of SCC power histories these equations have an overall failure/intact prediction accuracy of 63% (see Appendix B), which represents an improvement over the FUELOGRAM-based correlations used in the Kleczek/Lewis model [12] which have a failure/intact prediction accuracy of 55%.

The threshold equations are valid up to a burnup of 250 MWh kg(U)$^{-1}$. Beyond this burnup level the database contains no instances of SCC failure; therefore it is not possible to determine whether the same trend continues. Cases of non-failure at higher burnup suggest that an extrapolation up to at least 500 MWh kg(U)$^{-1}$ may be acceptable.

Post Irradiation Examination (PIE) of fuel elements has shown that the CANLUB coating begins to disperse at burnups greater than 300 MWh kg(U)$^{-1}$ [33], as detailed in Section 6.5. To account for this effect and its potential negative impact on the protective effects of the coating, the crack initiation threshold for CANLUB coated elements is scaled down to match the non-CANLUB threshold value via a linear weighting function between 250 and 500 MWh kg(U)$^{-1}$.

$$\Delta\varepsilon_{\phi c} = \left(2 - \frac{B}{250}\right)\Delta\varepsilon_{\phi c,CANLUB} + \left(\frac{B}{250} - 1\right)\Delta\varepsilon_{\phi c,non-CANLUB}, 250 \leq B \leq 500 \quad (27)$$

5.4 Incubation Time

An incubation time has been suggested in both laboratory and reactor instances of SCC. The incubation time is believed to be related to the time required to establish the correct chemical conditions at the crack tip. This theory is supported by experimental observation: when stressed Zircaloy samples are placed in an iodine environment there is a delay before SCC commences. However, unstressed Zircaloy samples preconditioned in an iodine environment begin cracking almost immediately on introduction of stress [34].

There is also evidence of an incubation time from CANDU reactor experience. It has been observed during refuelling operations that when irradiated fuel bundles are shifted through the high power centre region of the core the hold time in the high power region correlates to the occurrence of SCC. Examination of intact elements often reveal no incipient cracks, therefore the incubation time is believed to constitute a significant portion of the time required for element failure [35].

The initiation stage of SCC, including the incubation time, remains poorly understood [36], and therefore cannot be modeled in a mechanistic manner at this time. In the model the incubation time is assumed to be captured as the time required to reach $\Delta\varepsilon_{\phi c}$ following the ramp and as part of the crack growth time.

5.5 Crack Growth

If crack initiation is predicted based on Equations (25) and (27) the following portion of the model predicts the time for a through-wall failure to develop. These equations are solved in component 3 of the model.

Examination of fuel sheaths with SCC failures show two separate regions of crack growth: intergranular (IG) growth, which takes place along the grain boundaries, and transgranular (TG) growth, which takes place across grains. The scanning electron microscope (SEM) image of a stress corrosion crack in Figure 10 shows the distinct regions of intergranular and transgranular cracking.

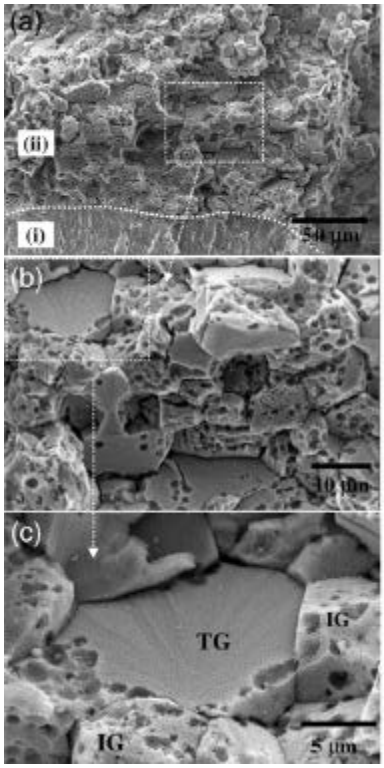

Figure 10: SEM image of a stress corrosion crack in a sheath containing a pre-introduced flaw (region i), showing intergranular (IG) and transgranular (TG) regions [37]

Acoustic emissions tests of Zircaloy-4 samples undergoing SCC in iodine give insight into the mechanisms of the two processes. In these tests, sensitive piezo-electric sensors are attached to the samples which ‘listen’ to the cracking process. It has been observed that intergranular cracking does not result in increased acoustic emissions from the sample. This is suggestive of a growth mechanism involving the chemical dissolution of zirconium at the grain boundaries. Transgranular cracking, by contrast, produces a measureable increase in acoustic emissions which is expected for a mechanism of iodine adsorption-induced embrittlement leading to transgranular cleavage [38]. A cleavage

mechanism for transgranular growth is further supported by the observation of 'fluting' patterns in some post irradiation examinations of the transgranular region [34].

.

Both intergranular and transgranular growth regions may be present along the length of a through-wall crack. However, intergranular cracking is observed to be more prevalent close to the crack initiation site than in the crack propagation region. It is has been proposed that intergranular crack growth takes place in the early phase of crack growth, until a crack of sufficient size is reached to produce a stress intensity sufficient to induce transgranular growth [34]. The modelling of the transition from intergranular to transgranular cracking is made more tractable in the model by assuming pure intergranular crack propagation in the early phase of growth, giving way to pure transgranular growth above a threshold stress intensity.

5.5.1 INTERGRANULAR CRACK GROWTH

Intergranular crack growth occurs along the boundaries between the grains. The grain boundary is a region of stress concentration, which assists iodine in reacting with the zirconium metal.

Zirconium removal from the crack site is proposed via a Van Arkel Process [34]. In this process, iodine reacts with zirconium to form ZrI_4 at relatively low temperatures, and decomposes into I_2 and Zr at higher temperatures. In nuclear fuel, it is proposed that ZrI_4 could form at a crack tip, (near coolant, lower temperature) and migrate towards the fuel (higher temperature) where it dissociates, depositing zirconium at the base of the crack or on the fuel surface, leaving iodine gas to diffuse back to the crack tip in a perpetual cycle. Oxygen in the gap may assist in this process via a $ZrI_4 + O_2 \rightarrow ZrO_2 + 2I_2$ reaction [29]. Removal of zirconium from the crack site may be assisted by the stress in that region, which weakens the Zr-Zr bonds [17].

In the model, the intergranular growth regime is similar to the methodology proposed in the Kleczek/Lewis model, which is illustrated in Figure 11 [12]. After the

crack initiation criterion is met, iodine released to the gap through radiolysis diffuses along the element length to a crack site located at the centre of the element. Iodine reaching the crack site reacts immediately with zirconium to form ZrI_4. Crack growth is modelled based on mass balance of the zirconium reacting with iodine.

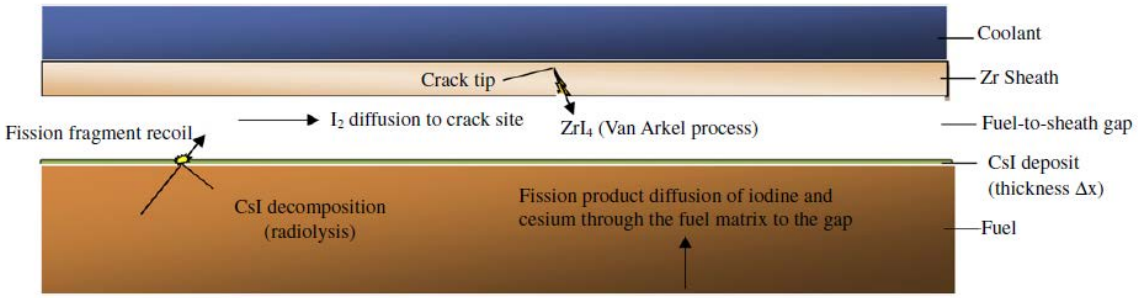

Figure 11: A schematic of the crack growth model in the Kleczek/Lewis model (not to scale) [12]

The iodine release rate to the gap calculated by the radiolysis model from Equation (17) is converted back to individual isotopes and divided by the element length l_e (m) to give release rate per unit length $R_{gap,i}$ (atoms $m^{-1}s^{-1}$):

$$R_{gap,i} = \frac{R_I}{2l_e}\left(\frac{C_{fs,i}}{C_{fs,T}}\right) \tag{28}$$

where the factor of two accounts for two iodine atoms per molecule of I_2.

Once released from the fuel surface, iodine diffuses through the gap to a crack site. As a simplifying assumption the recombination of iodine into CsI is assumed to be negligible. Diffusion of iodine along a 1-dimensional gap length is given by:

$$\frac{\partial C_{gap,i}}{\partial t} = D_{AB}\frac{\partial^2 C_{gap,i}}{\partial x^2} - \lambda_i C_{gap,i} + R_{gap,i} \tag{29}$$

where D_{AB} is a binary diffusion coefficient ($cm^2\ s^{-1}$) based on Chapman Enskog kinetic theory [12]. The binary diffusion coefficient for diffusion of I_2 in the helium fill gas is given by [12]:

$$D_{AB} = 0.0018583 \frac{\sqrt{T_g^3 \left(\frac{1}{M_{He}} + \frac{1}{M_{I2}}\right)}}{p\sigma_{AB}^2 \Omega_{AB}} \quad (30)$$

where Tg is the gap gas temperature (K), M_{He} = 4.003 g mol^{-1} and M_{I2} = 253.8 g mol^{-1} are the molar masses of helium and iodine gas, respectively, p is pressure in the gap (atm), σ_{AB} = 3.78 Å is the average collision diameter and Ω_{AB} =1 is the collision integral.

A single crack site is assumed at the centre of the element. This represents a worst case scenario because it provides the shortest diffusion distance. Symmetry is used to define Equation (29) on a domain equal to half the element length, therefore x = 0 represents the crack site. Zero concentration is imposed at the crack site as the iodine is assumed to react immediately. The initiation concentration of iodine in the gap is assumed to be zero. These assumptions are expressed by the initial and boundary conditions:

$$C_{gap,i}(x = 0, t) = 0 \quad (31)$$

$$C_{gap,i}(x, t = 0) = 0 \quad (32)$$

The amount of iodine reaching the crack site, $R_{crack,i}$ (atoms s^{-1}) is:

$$R_{crack,i} = 2\, D_{AB} \frac{\partial C_{g,i}}{dx}(x = 0) \quad (33)$$

The factor of 2 accounts for symmetry. Summing the isotopes, the total iodine reaching the crack site is:

$$R_{crack,T} = \sum_{I127 \rightarrow I135} R_{crack,i} \quad (34)$$

Diffusion from the crack surface to the crack tip is assumed to occur instantaneously, based on the small diffusion time constant for a path length equal to the sheath thickness:

$$\tau = \frac{t_{sheath}^2}{D_{AB}} = \frac{(0.43x10^{-3}m)^2}{0.106x10^{-3}m^2s^{-1}} = 0.02s \tag{35}$$

where D_{AB} is calculated by Equation 32 assuming T_g = 640 K and p = 10 atm. Assuming I_2 removes Zr in the form of ZrI_4, the rate of removal of Zr from the crack site is:

$$R_{Zr} = \frac{1}{2} R_{crack,T} \tag{36}$$

where the ½ term accounts for 2 I_2 molecules per ZrI_4 molecule.

The region of intergranular cracking is reported to be almost circular in shape. Assuming the crack grows with a semi-circular shape the intergranular crack length $a_{crack,IG}$ (m) is related to the volume of the crack and is determined by a mass balance equation by integrating the removal rate R_{Zr} over time:

$$V_{crack} = \frac{M_{Zr}}{\rho_{Zr} N_A} \int_{t,ramp}^{t,dwell} R_{Zr}\, dt = w \frac{\pi}{2} a_{crack,IG}^2$$

$$a_{crack,IG} = \left(\frac{2}{\pi w} \frac{M_{Zr}}{\rho_{Zr} N_A} \int_{t,ramp}^{t,dwell} R_{Zr}\, dt \right)^{0.5} \tag{37}$$

where M_{Zr} is the molar mass of zirconium (kg mol^{-1}), ρ_{Zr} is the density of zirconium (kg m^3) and w is the width of the crack. A width of 0.5 μm is assumed in the model based on the measurement of corrosion pits observed in SCC tests [37].

Experiments with SCC suggest that the intergranular crack growth rates are slow relative to transgranular growth rates [17] [39]. However based on the model described above, sufficient quantities of iodine are available for a typical power history that

intergranular crack growth would progress rapidly. The model makes several conservative assumptions regarding iodine release and diffusion to the crack site. A series of sensitivity studies were performed to assess the relative impact of these assumptions on intergranular crack growth rate. These studies were performed for a power history with a known SCC failure time and are presented in Section 8.2.

5.5.2 TRANSGRANULAR CRACK GROWTH

In transgranular cracking the crack path penetrates through the grain structure, preferentially travelling along the Basal planes. Transgranular growth during SCC is believed to occur due to a localized reduction in fracture toughness due to iodine adsorbing onto the surface of the crack. The iodine weakens the Zr-Zr bonds, reducing the fracture toughness and allowing crack propagation at stress intensity levels below the fracture toughness of the bulk alloy [29] [40].

A number of different methodologies exist for predicting crack growth. The stress intensity approach was chosen for this analysis because it is consistent with the majority of the literature on stress corrosion cracking. In this approach the stress intensity factor, K_I, defines conditions at the crack tip. The conditions for stress corrosion transgranular cracking are achieved when the value of K_I exceeds a critical value K_{ISCC} of 1.5 MPa $m^{0.5}$ [39] as discussed in Section 6.4.1. To determine when the conditions for transgranular crack growth are achieved, a linear elastic fracture mechanics analysis of the growing crack is used to determine K_I.

There are three modes of mechanical loading which relate to the orientation of a crack relative to the applied force, as shown in Figure 12.

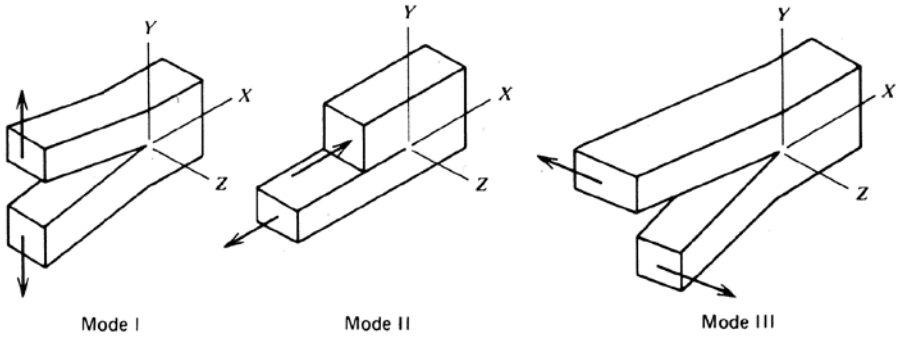

Figure 12 Modes of mechanical loading [14]

Mode I) Tensile or opening mode, where the crack surfaces move directly away from one other

Mode II) In-plane shear or sliding mode, where the crack surfaces slide over one another

Mode III) Anti-plane shear or tearing mode, where the crack surfaces move away from one another parallel to the minor axis of the crack

Mode I loading is encountered in most engineering problems. For the fuel sheath, where the largest stresses are in the hoop direction, Mode I loading is encountered if the crack is assumed to be oriented axially (aligned with the long axis of the fuel element). In the case of Mode I loading the stress intensity factor is denoted as K_I. The critical stress intensity for crack extension, without considering the effects of corrosion, is called fracture toughness and is denoted as K_{IC} [14].

A large body of analytical solutions exists for determination of stress intensity factors in different geometries. The generic equation for K_I is: [41]

$$K_I = F\sigma(\pi\, a)^{0.5} \tag{38}$$

where F is a geometric factor dependant on the body geometry and crack shape and a is the crack depth. For an axially oriented crack σ for K_I is the hoop stress σ_ϕ. The value of F for a semi-elliptical partial through-thickness crack in a cylinder is given by the weighted functions method as [41]:

$$F = Q^{0.5} \frac{t_{sheath}}{R_{in}} \frac{{r_{out}}^2}{{r_{out}}^2 - {R_{in}}^2} \left[2H_0 - 2H_1 \left(\frac{a}{R_{in}} \right) + 3H_2 \left(\frac{a}{R_{in}} \right)^2 - 4H_3 \left(\frac{a}{R_{in}} \right)^3 \right] \quad (39)$$

where r_{out} is the cylinder outer radius, R_{in} is the cylinder inner radius, t_{sheath} is the wall thickness, H_0 through H_3 are weighting functions correspond to uniform, linear, quadratic and cubic loading distributions and Q is a function of crack shape. Values for the weighting functions and Q are determined for a given geometry by comparison to reference solutions. Further details and tables of values for F are given in Appendix D. In the analysis the crack is assumed to maintain the same semi-circular shape as in the intergranular growth region. Sensitivity to crack shape is explored in Section 8.2.5.

The stress intensity increases with the depth of the crack. When the threshold value K_{ISCC} is exceeded, the stress intensity is sufficient for transition from intergranular to transgranular crack growth to occur.

Several experimental programs have studied transgranular crack growth rates as a function of K_I for iodine SCC of Zircaloy tubes. These experiments are discussed in detail in Section 6.4. Crack velocity da/dt (m s^{-1}) is calculated as [39]:

$$\frac{da}{dt} = 3.0x10^{-7} \ln(K1) - 1x10^{-8} \quad (40)$$

Crack extension in the transgranular growth region is calculated as the time integral of the growth rate:

$$a_{crack,TG} = a_{crack,IG} + \int_{t_{TG}}^{t} \frac{da}{dt} dt \quad (41)$$

In this model it is assumed that if sufficient iodine is present to develop an intergranular crack to the point of K_{ISCC}, sufficient iodine will remain available to propagate the transgranular crack.

5.5.3 DUCTILE FRACTURE

As the crack deepens the stress intensity increases. When the stress intensity factor exceeds the local fracture toughness K_{IC} of the material, rapid ductile failure of the sheath occurs. In the model failure is conservatively assumed to occur instantaneously when K_{IC} is reached.

The fracture toughness of Zircaloy-4 is strongly dependant on the concentration of dissolved hydrogen. In the presence of water Zircaloy-4 slowly takes up hydrogen (or deuterium in CANDU reactors) over time. The fracture toughness of Zircaloy-4 for T > 280 °C is given by EPRI as a function of hydrogen concentration as: [42]

$$\begin{aligned} K_{IC} &= 50\ MPa\ m^{0.5} && H < 100ppm \\ &= 30\ MPa\ m^{0.5} && 100 < H < 500ppm \\ &= 20\ MPa\ m^{0.5} && 500 < H < 750ppm \\ &= 12\ MPa\ m^{0.5} && H > 1000ppm \end{aligned} \tag{42}$$

The average hydrogen concentration in a typical discharged CANDU fuel bundle is reported to be in the range of 45-85 ppm [43], therefore K_{IC} = 50 MPa $m^{0.5}$ is employed in the model, which is conservative.

6 MODEL COMPONENTS

6.1 FISSION GAS SURFACE MULTIPLIER

As detailed in Section 5.1.2, as part of the fission gas release model a surface multiplier term was developed to relate the fission gas release rate calculated at the fuel surface to the release rate for the entire element. This factor accounts for the depth within the fuel surface which releases directly to the gap as well as the increased pellet surface area due to cracking. The multiplying factor has been derived by modelling a series of sweep gas experiments in which the fission gas release rate was measured. By comparing the experimental and predicted release rates for elements at different power levels and fuel burnups a correlation is derived for the fission gas surface multiplier.

Several sweep gas experiments were performed in the 1980's in the NRX reactor at Chalk River Laboratories using specially equipped fuel elements. In these tests, a carrier gas of helium with 2% hydrogen was continuously circulated through the operating fuel elements to sweep the fission product gases released from the fuel matrix. The gas was passed through a gamma spectrometer to measure isotopic concentrations of various short-lived fission gas species. These measurements were used to determine the rate of short lived fission product release from the fuel surface, and by comparing this to the fission rate in the element a release-to-birth ratio (R/B) was determined for each of several short lived species.

In the sweep gas tests iodine was never measured directly; it is assumed that iodine deposits on the fuel and sheath surfaces. Iodine diffusion behaviour was inferred by the diffusion of xenon, which exhibits similar diffusion properties [26].

The value of the surface multiplier is expected to be dependent on both element power and burnup. The fuel linear power rating determines the rate of fission product generation in the fuel, as well as the fuel temperature, which strongly impacts the diffusion behaviour. Fuel burnup determines the fission gas inventory within the fuel.

6.1.1 LINEAR POWER DEPENDENCE

The release dependence on power level is determined by modelling the sweep gas experiment FIO-141 [44], which measured release of short-lived gas species during reactor start-up. Reactor power was stepped from 17 to 56 kW m^{-1} at intervals of 9-10 kW m^{-1}, with hold times of one hour at each intermediate power level. The element burnup at the start of the test was approximately 25 MWh $kg(U)^{-1}$. As iodine was not measured directly during the test, iodine release rate was inferred from the release of Xe-138, which has a half-life ~15 minutes and therefore came close to equilibrium during the hold period. The release-to-birth ratio, $\mathfrak{R}/B$, for Xe-138 during the test is shown in Figure 13.

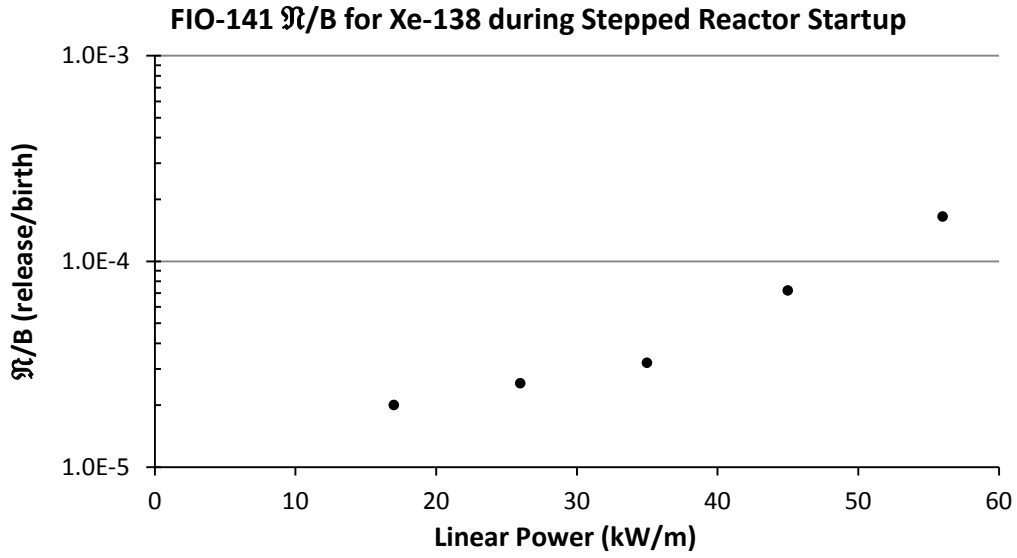

Figure 13: Release to birth ratio for stepped reactor startup in test FIO-141 [44]

The release-to-birth ratio is converted to a release rate per element, $R_{measured,Xe138}$ (atoms s^{-1}):

$$R_{measured,Xe138} = \frac{\mathfrak{R}}{B} Y_{Xe138} (1.489x10^{13}) \quad (43)$$

where Y_{Xe138} = 0.0642 (atoms fission^{-1}) is the isotopic yield of Xe-138 for fission of U-235, P (kW m^{-1}) is the fuel linear power rating and 1.489x10^{13} converts power in kW m^{-1} to fission rate assuming 200 MeV per fission.

The power history of test FIO-141 was run in the model to obtain fission gas release predictions for Xe-138 at the fuel surface. The model produces a volumetric release rate $R_{gb,v,Xe138}$ (atoms m^{-3} s^{-1}) as per Equation (7). This was multiplied by the surface area of the fuel to give release rate $R_{element,Xe138}$ (atoms m^{-1} s^{-1}):

$$R_{element,Xe138} = 2\,\pi\, r_{pellet} l_e R_{gb,v,Xe138} \tag{44}$$

where r_{pellet} (m) is the radius of the fuel pellet, l_e is the length of the fuel stack. The m^{-1} unit represents distance in the radial direction, or the depth into the fuel grain from which fission gas is released to the gap. Ideally this value would be quantified by integrating over the radial distance where the gas is released directly to the gap. However since this value is not known explicitly, it is captured in the fission gas surface multiplier term, which therefore has units of meters.

The multiplier value for each power level is calculated as:

$$M_{surf}(P) = \frac{R_{measured,Xe138}}{R_{element,Xe138}} \tag{45}$$

The multiplier values calculated for FIO-141 are shown in Figure 14. The multiplier is relatively constant below powers of 35 kW m^{-1}, while at higher powers it grows rapidly.

A possible explanation for the shape of the multiplier curve is that between 17 and 35 kW m^{-1} there was relatively little cracking in the fuel pellet. The increase in gas release in this interval would then be due mostly to the change in diffusion rate, which is captured in the model. As the power is increased above 35 kW m^{-1} cracking

exposes additional pellet surface area and increases the release rate. Since this effect is not inherently captured by the fission gas diffusion model, the multiplier value increases.

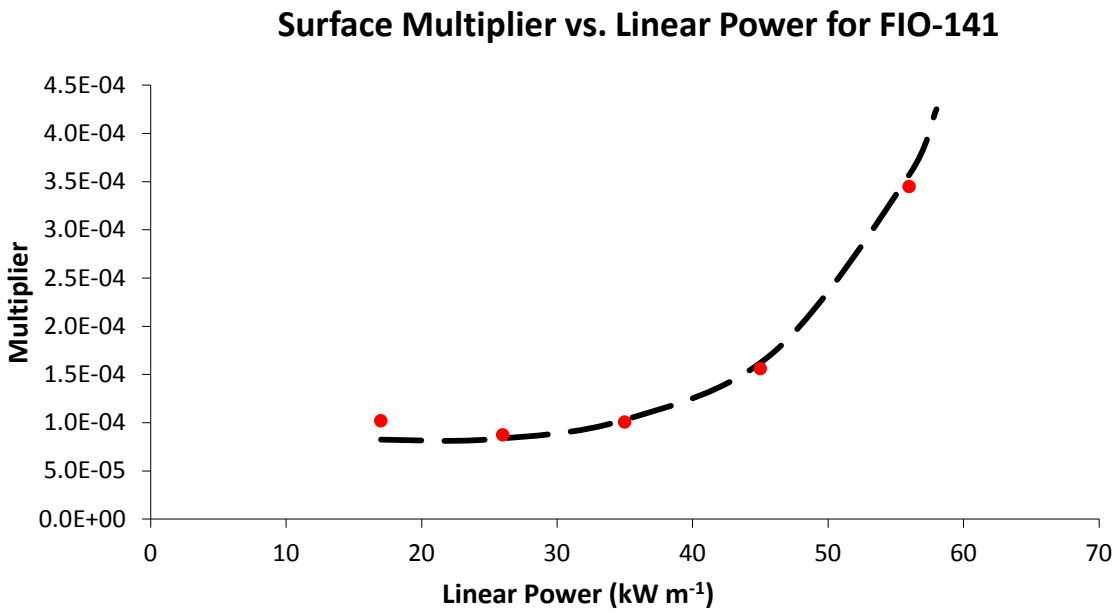

Figure 14: Release multiplier as a function of linear power based on FIO-141 tests

The linear power dependence of the surface multiplier is defined by an exponential polynomial fit to the data in Figure 14.

$$M_{surf} = e^{(-8.9-0.05P+0.0012\,P^2)}, \quad P > 20\ kW\ m^{-1}$$
$$M_{surf} = 8.1x10^{-5}, \quad P \leq 20kW\ m^{-1} \tag{46}$$

6.1.2 Burnup Dependence

Several sweep gas tests are available to determine the dependence of the fission gas multiplier on burnup. Tests FIO-122, FIO-124, FIO-133 and FIO-134 were performed at different power levels with elements at different burnups; the power levels and fuel properties for the tests are listed in Table 1. These test conditions were run in the

model to determine a multiplier value for each test; the multiplier values are plotted in Figure 15.

Table 1 Sweep Gas Tests Data [26], [12]

Characteristic	FIO-122	FIO-124	FIO-133	FIO-134
Fuel Type	UO_2	UO_2	UO_2	UO_2
Enrichment wt% U235	5.02	4.50	1.38	5.98
Density (Mg m^{-3})	10.71	10.65	10.65	10.64
Pellet Diameter (mm)	12.16	12.16	18.09	11.63
Fuel Stack Length (mm)	477	477	379	466
Sheath Material	Zircaloy-4	Zircaloy-4	304L SS	304L SS
Sheath Outside Diameter (mm)	13.11	13.11	19.85	13.06
Wall Thickness (mm)	0.43	0.43	0.82	0.635
Coolant Pressure (MPa)	8.5	8.5	8.5	8.5
Coolant Inlet Temp. (°C)	240	240	260-275	260
Linear Power (kW m^{-1})	38.2	53.4	50.7	53.6
Burnup	64.1	40.8	34.9	72.4
R/B Xe-133	7.06×10^{-4}	2.05×10^{-3}	1.42×10^{-3}	5.51×10^{-3}
R/B Xe-135m	5.37×10^{-5}	4.08×10^{-4}	1.35×10^{-4}	9.73×10^{-4}
R/B Xe-138	8.82×10^{-5}	1.54×10^{-4}	1.13×10^{-4}	1.30×10^{-3}

Tests FIO-124 and FIO-134 are particularly useful in establishing burnup dependence, as they were conducted at nearly the same power with different burnup levels. Therefore these two tests are used to benchmark the change in release rate with burnup.

The trend line from FIO-141 is re-plotted in Figure 15. The curve is scaled to intersect the data points for FIO-124 and FIO-134 to create two new curves. The lower curve represents a multiplier value for a burnup of 40.8 MWh $kg(U)^{-1}$, while the higher curve represents a burnup of 72.4 MWh $kg(U)^{-1}$. For intermediate burnups the multiplier is linearly interpolated between these curves. No extrapolation is made beyond the bounding curves; for example at burnup of 120 MWh $kg(U)^{-1}$ the multiplier is evaluated on the 72.4 MWh $kg(U)^{-1}$ curve at the appropriate linear power level.

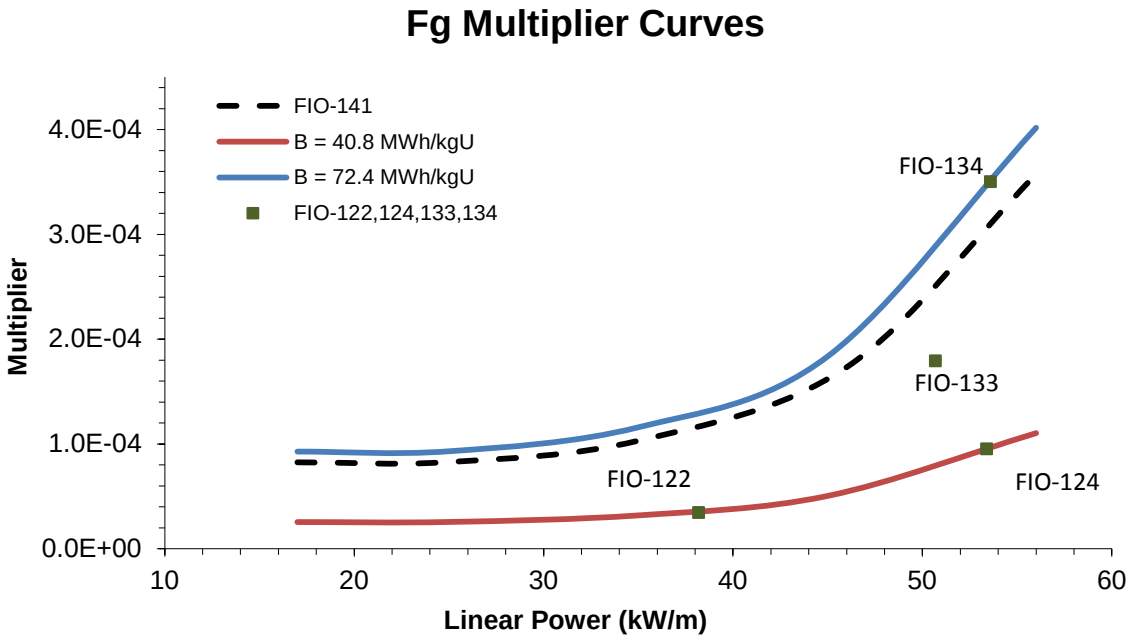

Figure 15: Fission gas multiplier curves. The upper and lower curve are scaled for data points FIO 124 and 134. FIO 122 and 133 are provided for comparison

The burnup dependence of the surface multiplier is then given as:

$$M_{surf} = A_{burnup} e^{(-10.0754 - 0.05P + 0.0012\,P^2)} \tag{47}$$

where:

$$\begin{aligned} A_{burnup} &= 1.0, && B \le 40.8 \\ A_{burnup} &= 1.0 + \frac{(B - 40.8)}{(72.4 - 40.8)} 2.82, && 40.8 < B < 72.4 \\ A_{burnup} &= 3.82, && B \ge 72.4 \end{aligned} \tag{48}$$

From Figure 15 the values for fission gas release for the FIO-141 test are higher than most of the data points from the other tests, although at 25 MWh kg(U)$^{-1}$ the burnup for FIO-141 was lower than for all other data points. The multiplier values for FIO-122

and FIO-133 also do not correlate well with respect to the burnup correlation in Equation (48).

Fission gas release prediction is a complex problem and prediction within a factor of 2 is considered reasonably accurate, based on the uncertainty in many of the parameters involved [45]. An important parameter which has not been captured in the model is the effect of the total power history on cracking. Pellet cracking occurs due to temperature gradients in the fuel, particularly during cool down periods [27], therefore an element which has undergone several shutdowns and startups or power level changes would be expected to have more cracking, and hence more fission gas release, than an element which is operated at a uniform power for its entire life in-reactor.

The model uncertainty notwithstanding all data points fall with the upper and lower burnup curves for the surface multiplier, which therefore bound the results of all experiments.

The available data for fission gas release benchmarking extends to 72.4 MWh $kg(U)^{-1}$. Average discharge burnup for a CANDU6 fuel bundle is approximately 170 MWh $kg(U)^{-1}$ [46]. The extrapolation of the fission gas multiplier using burnup values beyond the benchmarking range is not considered to be appropriate, as it is unclear to what extend the trend of increasing fission gas release continues at higher burnup. The use of the 72.4 MWh $kg(U)^{-1}$ curve as an upper limit results in a lower availability of iodine than if the burnup trend were extrapolated, therefore the use of the FIO-134 curve is a non-conservative assumption. However the impact is likely more than offset by other assumptions in the iodine transport model which results in higher than anticipated iodine availability as detailed in section 8.1.

6.2 Crack Initiation Criteria

The oxide layer on the inside surface of the fuel sheath is believed to act as a barrier to prevent gaseous iodine species in the gap region from causing corrosion of the

underlying metal. Therefore the first step in SCC is the development of a crack in this protective layer.

Post SCC examination of reactor fuel sheaths sometimes show cracks initiating at pits, hydrides or small defects on the sheath inner surface [17]. These create regions of elevated stress where the oxide layer would be expected to crack preferentially during a power ramp. However in other samples cracking is observed to initiate from a smooth surface [47]. Therefore an initial crack does not appear to be a pre-requisite for SCC, although failure would be more likely to occur as such a location.

The following sections explore several different mechanical parameters proposed as threshold failure criteria for SCC. These include the sheath hoop stress, hoop strain, hoop strain rate and net change in hoop strain during the power ramp. A database of CANDU and research reactor fuel elements power histories containing known cases of SCC defects was used to assess these different parameters. This database is available in the open literature [12] and is reproduced in Appendix B.

The FAST code was used to model the mechanical parameters for each of the power histories in this database. For each of the proposed failure criteria the parameter vs. burnup at the power ramp has been plotted in the following sections showing failed and intact elements. Fuels containing a CANLUB coating are plotted separately from the data for uncoated elements to show the difference in performance between the two. A failure threshold equation is plotted for each parameter to delineate the apparent threshold for failure, which is burnup dependant. The accuracies of each equation in terms of correctly predicting failure cases and the total rate of correct prediction are presented for each case.

A number of data points in the power history database were excluded from the analysis. Fuel elements with a ‘thin’ coating of CANLUB (~2.5 μm) are excluded as there are too few of these data points to draw meaningful conclusions about their performance. The CANLUB power histories analysed all contain a ‘thick’ (>5 μm) coating. Also excluded are a set of defects from the Pickering reactor which occurred due

to very small power ramps resulting from refuelling of an adjacent fuel channel, and a similar set of three elements for Douglas Point which also failed. The cause of these defects is unknown and they are not representative of a typical SCC process as it generally occurs in reactor.

6.2.1 HOOP STRESS FAILURE CRITERION

Several laboratory studies report a minimum hoop stress required for SCC. This is commonly obtained by internal pressurization tests of Zircaloy sheaths section filled with inert gas and iodine. This loading configuration results in a stress state where the hoop stress is equal to twice the longitudinal stress; the results are typically expressed in terms of the hoop stress. Internal pressurization tests by Schuster [39] showed no SCC below 300 MPa hoop stress for Zircaloy-4 claddings pre-irradiated in a research reactor. A similar series of tests conducted by EPRI on irradiated claddings removed from commercial BRWs and PWRs fuel elements found the lowest failure hoop stress in the range of 160 – 195 MPa [48]. Minimum failure hoop stress values reported by Garlick [35] and Cox [49] using different testing techniques fall within the range of these two tests. In all cases higher stress resulted in a shorter failure time.

From a theoretical perspective, Rossi [36] shows through mechanical analysis that the sheath stress required for oxide cracking would be expected to be in the region of 300 MPa.

A threshold hoop stress could be defined as a criterion for crack initiation as:

$$\sigma_{\phi} \geq \sigma_{\phi,c}(B) \tag{49}$$

where σ_{ϕ} is the maximum hoop stress calculated along the inside surface of the sheath and $\sigma_{\phi,c}(B)$ is the burnup dependant critical hoop stress. Burnup dependence is expected based on the reduction in the threshold hoop stress seen in experiments between

irradiated and unirradiated samples [39] , [48]. The experimental values listed above would suggest a threshold value in the range of 160 – 300 MPa.

As noted in Section 5.2 the hoop stress value used to calculate the stress intensity at the crack tip is capped at the yield stress. This prevents the prediction of non-physically high stress that may occur shortly after a power ramp due to limitations in the plastic deformation model in FAST, and provides more reasonable values for the calculation of stress intensity factors.

The yield strength of Zircaloy-4 at 300°C is approximately 380 MPa. For the maximum hoop stress analysis that follows, if the yield stress limit were observed most of the data points would evaluate to the yield stress and very little comparison could be made between the different power histories. For failure criterion calculations, the stress is not capped at the yield stress in order to allow a more meaningful comparison of data. The values in excess of yield could be viewed as the extent of yielding plastic deformation which would occur in the sheath.

It should be noted that the assumption of a fully elastic material is shared by many of the experiments listed above, which also report the hoop stresses in excess of the yield stress and even the ultimate tensile strength of Zircaloy for some tests.

The maximum hoop stress for elements in the power history database are plotted for non-CANLUB coated elements in Figure 16 and for CANLUB coated elements in Figure 17. Best fit lines delineating the apparent threshold stress for element failure are given in Equations (50) and (51).

For non-CANLUB coated fuels the minimum stress at which failure is observed is approximately 200 MPa, which is within the range reported by experiments on irradiated sheaths. However this threshold value is reached only at a burnup of approximately 220 MWh $kg(U)^{-1}$; at lower burnups the threshold stress is much higher than experimental values. Similarly, for CANLUB coated fuels the stress threshold is much higher than experimentally reported values, with no failures below 530 MPa.

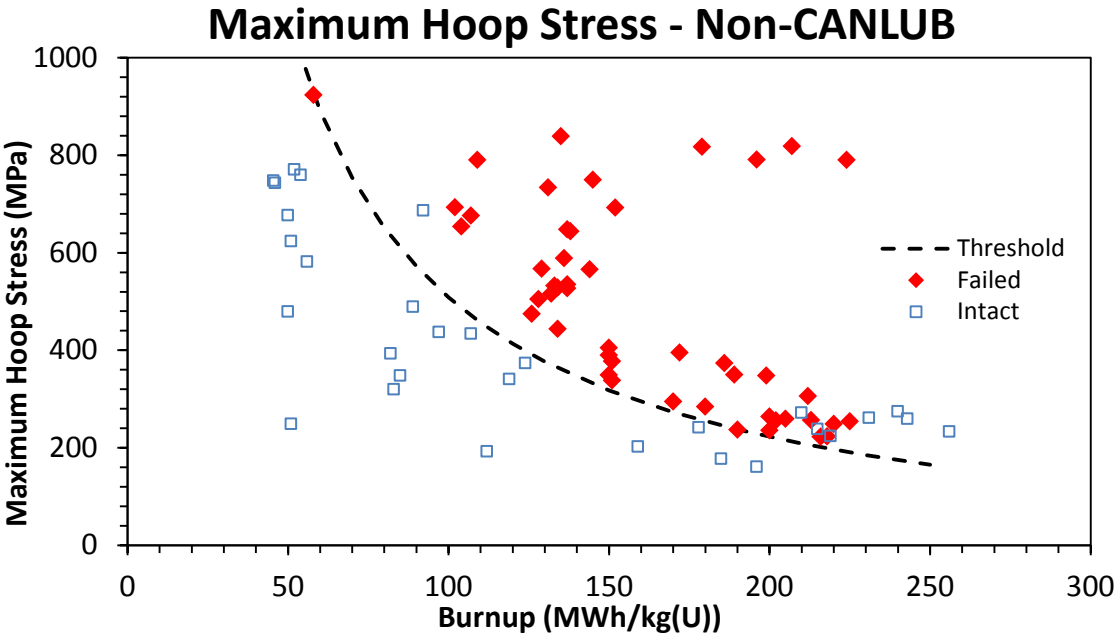

Figure 16: Maximum Hoop Stress for non-CANLUB coated elements showing failed and intact elements

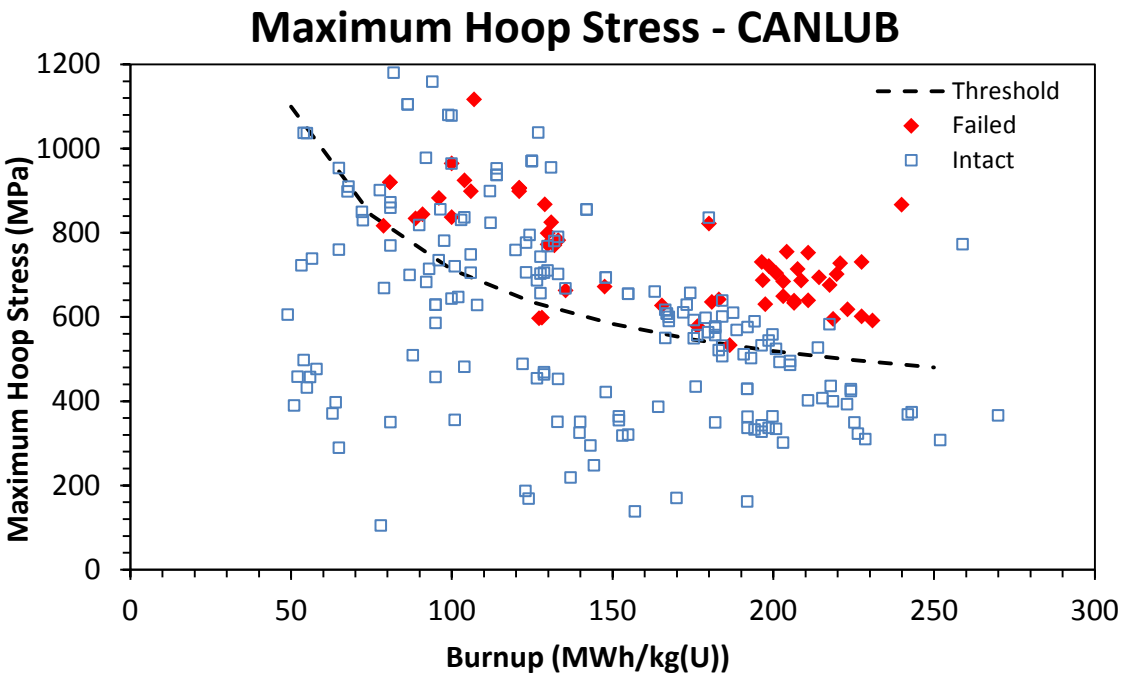

Figure 17: Maximum Hoop Stress for CANLUB coated elements showing failed and intact elements

Recall that the four conditions required for SCC are stress, corrodent, a susceptible material, and time. If sufficient stress is present at the time of the ramp to propagate a crack, as suggested by experiments, then the higher limit for SCC in lower burnup and CANLUB-coated fuels must be due to:

1. Lack of a sufficient quantity of corrodent. CANLUB is believed to reduce the amount of iodine available in the gap to participate in SCC, however this would not explain the threshold values for non-CANLUB fuels.
2. Lack of a susceptible material, i.e. at lower burnups the passive oxide layer requires higher stress to break or is able to repair itself more quickly
3. Insufficient time for SCC to propagate an incipient crack to a through-wall failure.

The threshold stress for non-CANLUB elements is:

$$\sigma_{\phi,c} = 6.425x10^{7} + \frac{5.723x10^{10}}{B} \tag{50}$$

The threshold stress for CANLUB elements is:

$$\sigma_{\phi,c} = 3.253x10^{8} + \frac{3.873x10^{10}}{B} \tag{51}$$

The effectiveness of the threshold hoop stress correlations is evaluated in Table 2, which shows the percentage of correct prediction of failure vs. intact (i.e. the percentage of the points in Figure 16 and Figure 17 which fall on the correct side of the threshold line).

For the CANLUB power histories there is a pair of failure cases which fall below the threshold correlation as seen in Figure 17. These failure cases are also incorrectly predicted by the FUELOGRAM-based correlations in the Kleczek/Lewis model and the threshold delta hoop strain correlations described in Section 6.2.4. They represent two of only three points in the database from the Bruce NGS. Because they represent a unique

subset of data which is incorrectly predicted by multiple correlations they have been treated as outliers.

Table 2: Accuracy of maximum hoop stress correlations for predicting SCC failure (representing the percentage of power histories which fall on the correct side of the threshold line)

	Failed vs intact prediction accuracy
Non-CANLUB	89%
CANLUB	60%
Database Total	66%

6.2.2 HOOP STRAIN FAILURE CRITERION

The power ramp correlations such as the FUELOGRAMS define the maximum power as a critical parameter for determining the probability of SCC [7]. The maximum power strongly influences thermal swelling and the hoop strain in the sheath. Therefore the maximum sheath hoop strain is evaluated as a threshold criterion.

The percent engineering hoop strain is used for this analysis. It is defined in terms of the radial deformation as:

$$\varepsilon_{\phi} = \frac{2\pi u}{2\pi r_{sheath,initial}} x100 = \frac{u}{r_{sheath,initial}} x100 \tag{52}$$

Where u is radial displacement and $r_{sheath,initial}$ is the initial inner radius of the sheath. A threshold sheath strain could be defined as:

$$\varepsilon_{\phi} \geq \varepsilon_{\phi,c}(B) \tag{53}$$

The hoop strain values calculated for the power history database are presented in Figure 18 and Figure 19. The hoop strain is defined as the maximum hoop strain on the inside surface of the sheath at the end of the power ramp dwell time. Best fit lines are calculated to delineate the lower bound of strain at which failure was observed. For non-

CANLUB elements no failures are observed below a hoop strain of 0.45%. CANLUB coated fuels appear to require a significantly higher strain for SCC failure, with only one failure below a strain of 1.2%. The best fit lines delineating the apparent threshold stress for element failure are given in Equations (54) and (55).

The threshold hoop strain for non-CANLUB elements is:

$$\varepsilon_{\phi,c} = 0.135 + \frac{66.9}{B} \tag{54}$$

The threshold hoop strain for CANLUB elements is:

$$\varepsilon_{\phi,c} = 0.527 + \frac{104.7}{B} \tag{55}$$

The accuracy of the threshold hoop strain correlations in terms of correctly predicting failure or non-failure is presented in Table 3. These accuracies are compared to those of the other parameters in Section 6.2.5.

Table 3: Accuracy of hoop strain correlations for predicting SCC failure (representing the percentage of power histories which fall on the correct side of the threshold line)

	Failed vs. intact prediction accuracy
Non-CANLUB	86%
CANLUB	51%
Database Total	58%

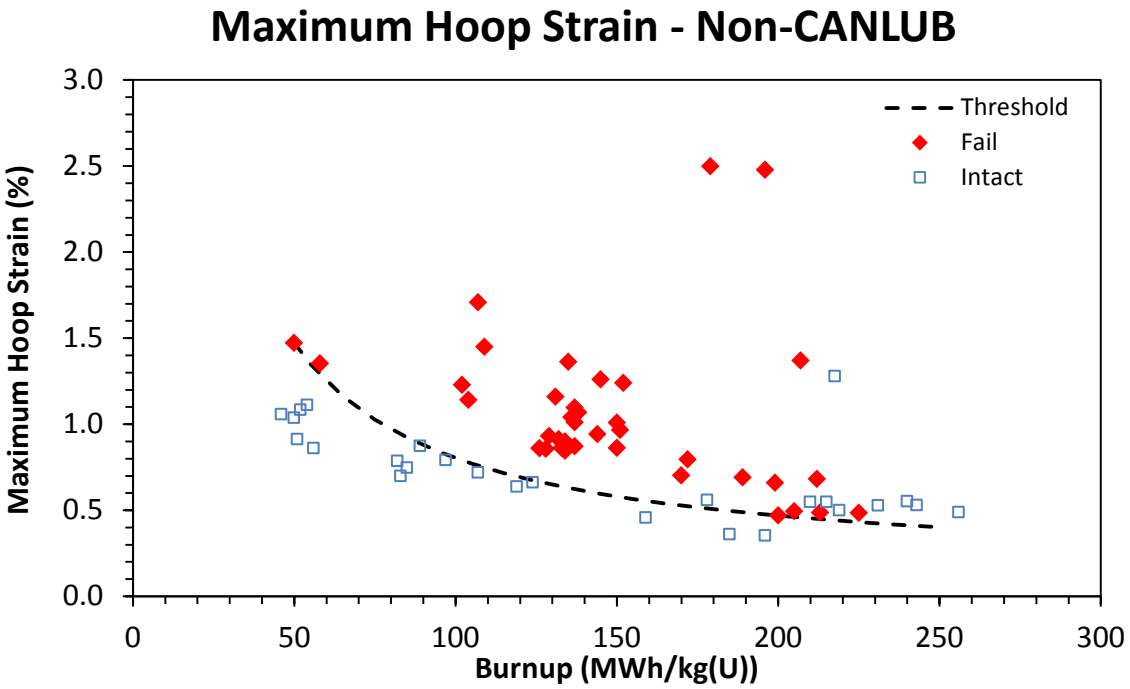

Figure 18: Maximum Hoop Strain for non-CANLUB coated elements showing failed and intact elements

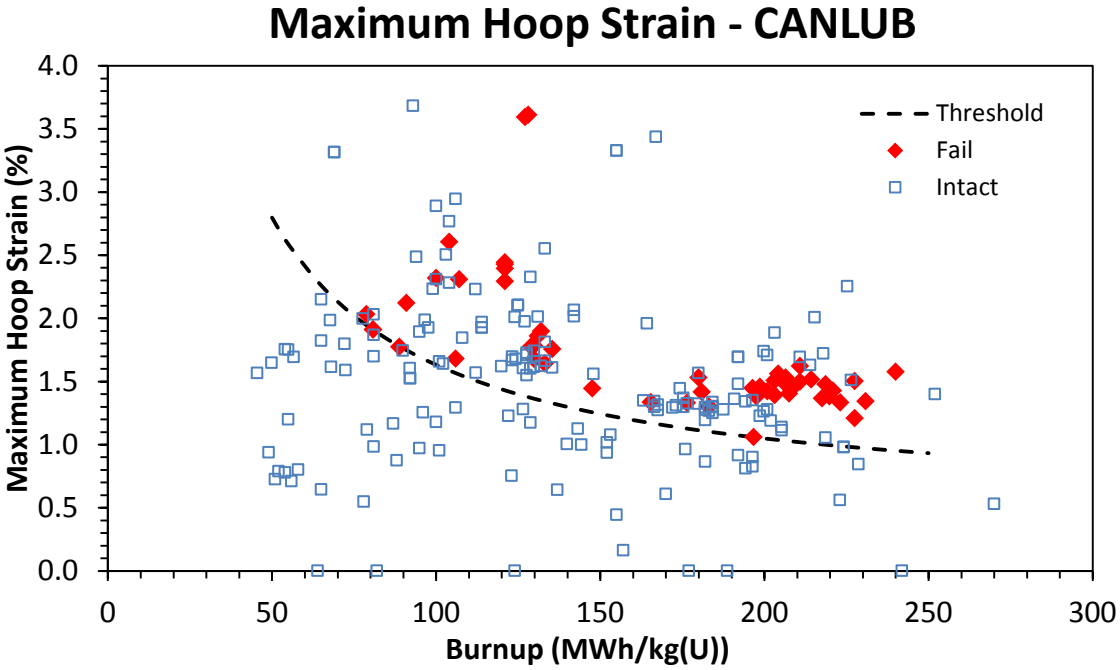

Figure 19: Maximum Hoop Strain for CANLUB coated elements showing failed and intact elements

6.2.3 HOOP STRAIN RATE FAILURE CRITERION

Hoop strain rate has been proposed as an important factor in determining initiation of SCC [50]. It is suggested that the strain rate determines the time available for the oxide layer to regrow [51] and time for stress relaxation to occur in the sheath [52].

A critical strain rate for SCC is supported by laboratory experiments. Pressurization tests conducted by EPRI with unirradiated cladding material showed that SCC was confined to hoop strain rates between 2×10^{-6} %/s^{-1} and 5×10^{-3} %/s^{-1} [53]. It is suggested that strain rates below this critical range allow time for the passive oxide layer to regrow more quickly than cracking can progress, while strain rates above this range cause nucleated SCC cracks to become blunted, growing wider rather than deeper [54].

A critical strain rate criterion is not supported by reactor experience. A series of tests conducted in the NRX reactor with power ramping rates between 0.5 and 300% full power per minute showed no change in the rate of SCC failure [52]. The strain rate is strongly dependant on the ramping rate; therefore these tests suggest that the strain rate is not the critical factor for SCC initiation.

The determination of the strain rate from the power history database is complicated by the fact that the rate of change of linear power (ramp rate), which strongly influences sheath strain rate, is not known in most cases. While the ramp size ΔP is defined, the time period of over which that ramp occurred, Δt, is not. For the power reactor cases a rough estimate of ramp rate can be made given the known speed of the refuelling machine ram [7] and assuming that the change in power reported in the database occurs over a single, two bundle shift of one meter. For the power histories from research reactors the ramp rates are not as simple to estimate; these ramps may occur due to manual repositioning of the fuel or by controlled change to reactor power and frequently occur in a series of steps as opposed to a single ramp.

Due to the lack of appropriate data, the strain rate was not evaluated as a threshold parameter.

6.2.4 DELTA HOOP STRAIN FAILURE CRITERION

As discussed in the previous section, SCC appears to be relatively insensitive to ramping rate ΔP/Δt. However, the size of the power ramp, ΔP, is known to be an important parameter in occurrence of SCC [7]. This would suggest that change in hoop strain over the ramp, $\Delta\varepsilon_\phi$, is the important parameter.

For the following analysis the change in hoop strain is taken as the difference between the pre-ramp hoop strain and the hoop strain at the end of the power ramp dwell time. The maximum hoop strain along the inside surface of the sheath is evaluated, which typically occurs at the circumferential ridge between pellets. The threshold change in hoop strain is defined as:

$$\Delta\varepsilon_\phi = \varepsilon_\phi\left(t_{ramp} + t_{dwell}\right) - \varepsilon_{\phi,}(t_{ramp}) \tag{56}$$

where t_{ramp} is the time at the start of the power ramp and t_{dwell} is the length of time the element spends at power following the ramp.

For a number of the power history in the database dwell time is reported as ">2.5 h", which is a catch-all category for any long dwell time. For these cases the dwell time in the model is assumed to be 2.5 hours. This introduces a truncation error; the value of $\Delta\varepsilon_\phi$ is cut off at 2.5 hours, whereas if the real dwell time were longer the value of $\Delta\varepsilon_\phi$ would continue to rise. This assumption is necessary owing to the lack of more specific data on dwell times; however its impact is limited because for most cases the strain rate at 2.5 hours after a power ramp is quite low. For example for power history FFO-104, $\Delta\varepsilon_\phi$ increases by 7% for a 10 hour dwell time compared to a 2.5 hour dwell time, and 11% for a 48 hour dwell time.

The maximum change in hoop strain for elements in the power history database are plotted for non-CANLUB coated elements in Figure 20 and for CANLUB coated elements in Figure 21. Best fit lines delineating the apparent threshold for element failure are given in Equations (57) and (58).

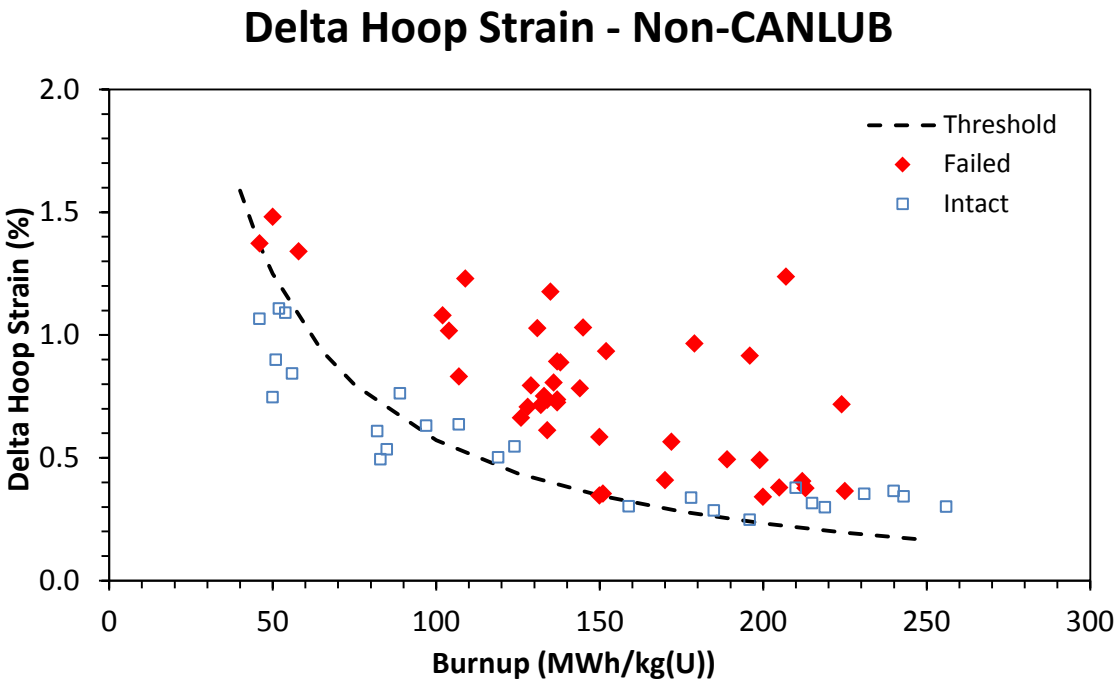

Figure 20: Change in hoop strain at power ramp for non-CANLUB elements showing failed and intact elements

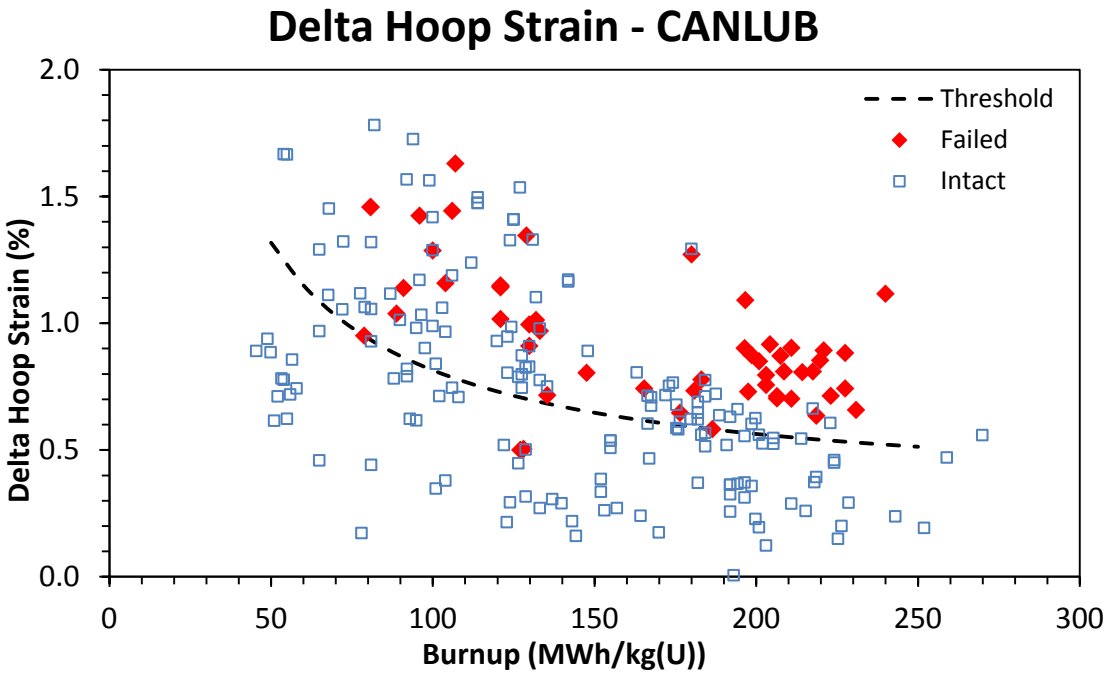

Figure 21: Change in hoop strain at power ramp for CANLUB coated elements showing failed and intact elements

The threshold change in hoop strain for non-CANLUB elements is:

$$\Delta\varepsilon_{\phi,c} = -1.06\text{x}10^{-1} + \frac{67.7}{B} \quad (57)$$

The threshold change in hoop strain for CANLUB elements is:

$$\Delta\varepsilon_{\phi,c} = 3.12\text{x}10^{-1} + \frac{50.3}{B} \quad (58)$$

The accuracy of these correlations in predicting failure or non-failure is presented in Table 4.

For the CANLUB power histories there are two instances of fuel failure which fall below the threshold line. As discussed in Section 6.2.1 these points are from a limited group of data from the Bruce NPGS and are also outliers for both the hoop stress threshold correlation and the FUELOGRAM-based correlations of the Kleczek/Lewis model.

Table 4: Accuracy of change in hoop strain correlations for predicting SCC failure

	Failed vs. intact prediction accuracy
Non-CANLUB	77%
CANLUB	60%
Database Total	63%

6.2.5 Comparison of Parameter Thresholds

The accuracy of the various correlations presented in the previous sections is compared with the FUELOGRAM-based methodology used in the Kleczek/Lewis model [12] in Table 5 This comparison shows that the hoop stress $\sigma_{\phi,c}$ and the change in hoop strain $\Delta\varepsilon_{\phi,c}$ correlations have similar accuracy as predictors of SCC failure. The hoop stress correlation is slightly more accurate overall due to better prediction of the non-CANLUB cases. As discussed in Section 5.2 the prediction of hoop stress in the model

assumes an almost perfectly elastic sheath response due to the lack of prediction of yielding plastic deformation. The hoop strain is more robustly defined, therefore in the model the change in hoop strain threshold correlation is implemented to predict whether conditions are met for SCC initiation. This correlation accurately predicts 63% of cases in the power history database; this represents an improvement over the FUELOGRAM-based correlations which were used in the Kleczek/Lewis model.

Table 5: Accuracy in predicting failure or non-failure for different parameters

	ISCC FUELOGRAM-based model	$\sigma_{\phi,c}$	$\varepsilon_{\phi,c}$	$\Delta\varepsilon_{\phi,c}$
Non-CANLUB	78%	89%	86%	77%
CANLUB	49%	60%	51%	60%
Database total	55%	66%	58%	63%

6.3 INTERGRANULAR CRACK GROWTH

Growth rates for intergranular cracking are not well defined in literature. One method for estimating intergranular growth rate is through post-test measurement of the size of the intergranular cracking region. By subtracting the estimated transgranular growth time (described in the next section) from the total failure time an 'initiation time' can be determined, which includes the time for intergranular crack growth and an incubation period for the correct chemical conditions to be achieved [39]. The last two phenomena are difficult to separate as the test methodology precludes direct observation of crack growth.

Estimates in literature for SCC intergranular cracking growth rates cover a fairly wide range of values. Cox proposes a rather high value of approximately $2x10^{-7}$ m s^{-1} [17] while Schuster suggests a much lower stress-dependant value of $5x10^{-9}$ m s^{-1} at 300 MPa and $2x10^{-8}$ m s^{-1} at 400 MPa [39]. Burst test conducted by Park *et al.* suggest average velocities in a similar range to Schuster [37].

The iodine transport model described in Section 5.5.1 predicts very fast intergranular growth rates. For the power ramp test FFO-104, which had a failure time of

approximately 20 minutes, the model predicts intergranular growth rates on the order of $1x10^{-5}$ m s^{-1}. For the above estimates in literature a growth rate in the range of $5x10^{-9}$ m s^{-1} to $2x10^{-7}$ m s^{-1} is expected. Therefore the model assumptions are reviewed and a series of sensitivity studies are conducted in order to determine the impact of the key parameters related to those assumptions. The sensitivity studies are presented in Section 8.2. The results of these studies indicate possible areas for future investigation for model improvement.

6.4 TRANSGRANULAR CRACK GROWTH

6.4.1 THRESHOLD STRESS INTENSITY

The threshold stress intensity factor, K_{ISCC}, is typically measured through internal pressurization tests of fuel sheath specimens with cracks pre-introduced on the inside surface of the sheath. Following failure, the samples are cut in half and the size of the initial crack surface is measured to calculate the stress intensity at the crack tip at the start of the test. By determining the smallest K_I at which SCC was observed the threshold value K_{ISCC} can be determined. K_{ISCC} values reported using this test method range from 3.3 – 6.0 MPa $m^{0.5}$ for unirradiated sheath material [37] [39] and 1.5 - 3.7 MPa $m^{0.5}$ for irradiated material [39] [48]. K_{ISCC} for the model is conservatively set at the minimum reported value for irradiated material of 1.5 MPa $m^{0.5}$.

6.4.2 GROWTH RATE EXPERIMENTS

Ideal growth rate data would provide the crack growth rate for the instantaneous value of K_I in a test. However the internal pressurization tests relevant to fuel sheath SCC are not able to directly measure the growth rate of the crack during the test. Instead, post-test examination measures the depth of the cracking region, and based on the failure time an average crack growth rate is correlated to the stress intensity factor at the beginning of

the test. The average crack growth rates for four series of experiments are shown in Figure 22.

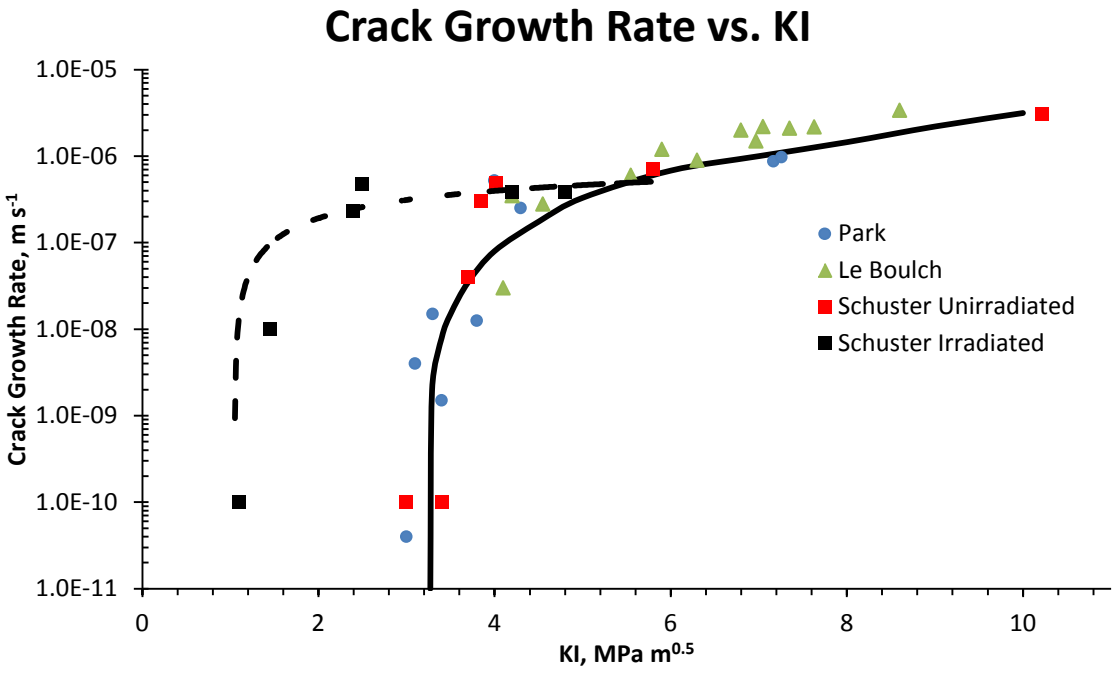

Figure 22: Crack growth rate vs. initial stress intensity factor from three different researchers, reproduced from [37] and [39]

Modelling crack growth using a constant average velocity would result in a constant growth time for every case. In reality as the crack deepens the stress intensity increases, which increases the crack growth rate.

Instead of using a constant growth rate, the growth rate curves from Figure 22 are approximated as the instantaneous crack growth rate based on the current value of K_I. With this assumption, the K_I value is calculated at every time step as the crack grows, and the growth rate increases as the crack deepens. This assumption results in faster growth rates than using a constant average growth rate and is therefore conservative.

The crack growth velocity vs. K_I correlation in Equation (40) (section 5.5.2) is based on the fit line for the irradiated material shown in Figure 22, originally from [39].

6.4.3 EFFECT OF IRRADIATION

Irradiation has an important impact on the fracture properties of Zircaloy. Bombardment of high energy neutrons (E > 1 MeV) creates point defects in the lattice structure, resulting in embrittlement and a reduction in K_{ISCC}. The surface of the sheath is also bombarded with recoiling fission products from the UO_2 fuel. These particles have a penetration depth of approximately 10 um and cause further damage to the inner surface of the sheath [39].

There are relatively little data on fracture properties of irradiated Zircaloy due to the complexity and cost of performing tests on radioactive materials in hot cell facilities. Schuster reports a K_{ISCC} of 1.5 MPa $m^{0.5}$ for fuel sheaths irradiated to a fast neutron fluence of $1.3x10^{21}$ n cm^{-2}, whereas K_{ISCC} for similar, unirradiated samples was 3.2 MPa $m^{0.5}$. Furthermore, growth rates as a function of K_I were lower for the irradiated material compared to unirradiated samples [39] as shown in Figure 22. The degree of reduction in K_{ISCC} is in reasonable agreement with Yaggee *et al.* [48] who report a K_{ISCC} of 2.2 - 3.7 MPa $m^{0.5}$ for irradiated materials compared to 3.9 - 6.0 MPa $m^{0.5}$ for non-irradiated samples, a reduction of about a factor of 1.6.

6.4.4 IMPACT OF CRACK SHAPE

The crack shape has an important impact on the calculation of the stress intensity factor. In Equation (39) in Section 5.5.2 the geometric factor for the calculation of stress intensity is dependent on the crack length-to-depth ratio. An example of post-test examination of the crack surface in Figure 23 shows an elongated elliptical crack [37]. Other experiments report an almost circular crack shape [39]. As a simplification a circular crack shape is assumed in the model. A sensitivity study on crack shape is presented in Section 8.2.5.

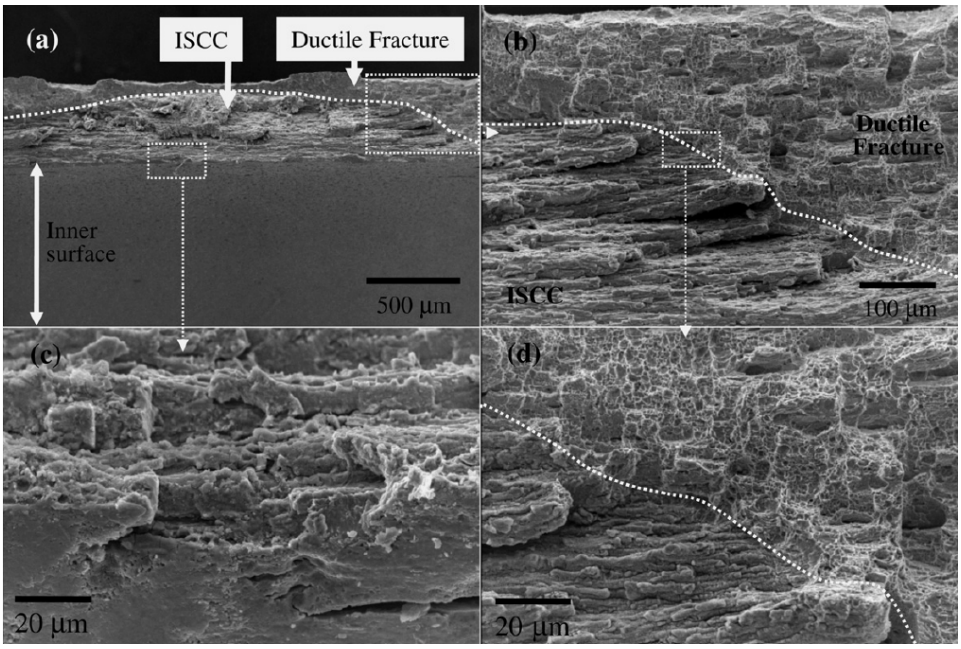

Figure 23: Fracture surface for iodine SCC in unirradiated Zircaloy-4 from an initially smooth surface, the crack shape is roughly elliptical [37]

6.5 CANLUB

CANLUB is a graphite-based industrial lubricant. It is used as a coating on the inner surface of CANDU fuel elements to mitigate SCC. The intention of the developers of CANLUB was to reduce the friction between the fuel pellets and the sheath and thus reduce stresses [55] .

While CANLUB does improve the fuel's resistance to SCC, the mechanism through which this is accomplished is not as originally thought. In a low-moisture environment such as the inside of a nuclear fuel bundle, graphite is a poor lubricant. The impact of CANLUB in SCC mitigation is now believed to be primarily due to its chemical interaction with fission products [55] [56]. The exact mechanism of interaction is still not fully understood, however the graphite itself does not appear to react significantly with iodine.

Chan suggests that ethyl cellulose, a binder residue left over during fuel manufacturing, is the active ingredient [57]. The amount of residual binder in the fuel element is dependent on the temperature at which the coating is baked during manufacturing. Tests to conclusively demonstrate the 'active ingredient' in CANLUB are ongoing.

In the model the chemical influence of CANLUB is based on the Kleczek/Lewis model, which proposes that alkaline metal impurities, principally sodium, react with iodine, reducing its availability to cause SCC [12]. Iodine is assumed to react preferentially with the sodium impurities in the CANLUB, so that the concentration of sodium C_{Na} is subtracted from the net iodine surface concentration in Equation (14). This results in a zero concentration of iodine on the fuel surface until the sodium impurity is 'used up'. The concentration of sodium impurity is defined as [12]:

$$C_{Na} = \frac{\omega_{Na}\rho_{CANLUB}\mathrm{t}_{CANLUB}N_A}{A_{Na}} \tag{59}$$

where ω_{Na} is the measured content by weight of sodium in CANLUB ($137\text{x}10^{-6}$ g g^{-1}) [11], ρ_{CANLUB} is the density of CANLUB (0.9g cm^{-3}), t_{CANLUB} is the coating thickness of CANLUB (typically 5 µm for 'thick' CANLUB), and A_{Na} is the atomic weight of sodium (22.98977 g mol^{-1}).

Even with the simplification of assuming the entire concentration of sodium reacts with iodine before corrosion can take place, the implementation described above has little impact on the predicted failure time for the benchmarking test FFO-104, although it would preclude SCC at lower burnups. A sensitivity study involving the impact of the CANLUB model is described in Section 8.3.

It is apparent from the crack initiation plots for CANLUB and non-CANLUB fuel elements in Section 6.2 that more severe mechanical conditions are required to cause SCC in CANLUB elements. The present treatment of CANLUB as a chemical getter

clearly does not fully account for its interaction with the fuel. The mechanism through which CANLUB mitigates SCC is still not fully understood.

It is known that CANLUB begins to disperse with increasing burnup. PIE of high burnup fuel elements shows a high degree of variability in CANLUB retention, with between 35% to 90% remaining at a burnup of 350 MWh kg(U)$^{-1}$ as shown in Figure 24. The cause of CANLUB dispersal is not fully understood [33]. In the current model the iodine-gettering sodium impurity will be consumed before the fuel reaches these high burnup levels. To account for the potential impact of CANLUB dispersal on the crack initiation criterion, the CANLUB threshold value is linearly scaled down to the non-CANLUB threshold criterion between a burnup of 250 and 500 MWh kg(U)$^{-1}$ as shown in Equation (27) in Section 5.3. This is illustrated below in Figure 25. The limited data for fuel power ramped at burnup above 250 MWh kg(U)$^{-1}$ show no failure for several data points above the threshold line, which suggests that this scaled down limit is conservative.

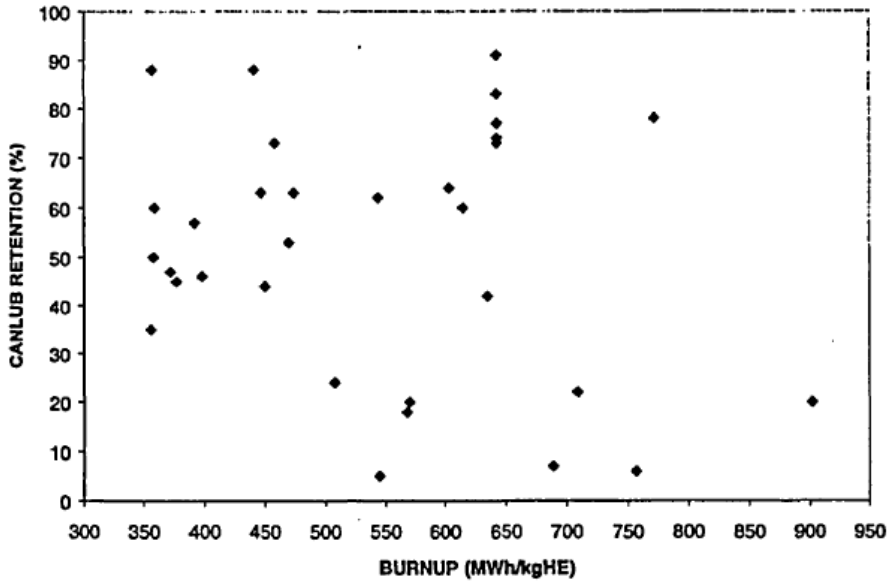

Figure 24: CANLUB retention at high burnup based on PIE examinations, from Floyd [33]

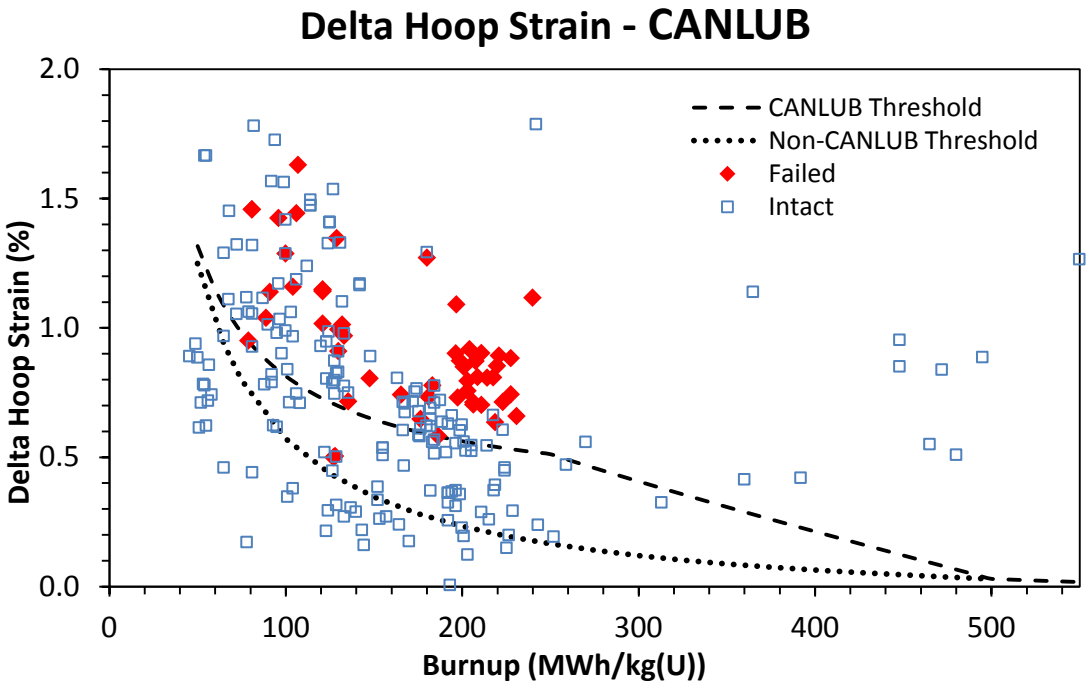

Figure 25: Delta hoop strain ($\Delta\varepsilon_{\phi}$) threshold for CANLUB coated elements at higher burnup

7 MODEL IMPLEMENTATION

The model described in Chapter 5 consists of a series of Ordinary Differential Equations (ODEs), Partial Differential Equations (PDEs) and analytical equations. These are implemented using the commercial software COMSOL Multiphysics©. The details of the implementation of the model are described in the following sections.

7.1 COMSOL

COMSOL is a finite element analysis software designed to solve physics and engineering equations, and is especially well suited for systems of coupled non-linear equations (multiphysics). The software includes built-in packages for many commonly encountered physics such as solid mechanics, heat transfer and fluid dynamics. COMSOL also allows the user to define custom PDEs and ODEs. These equations may be defined on a volume, surface, edge or point for a given solution geometry. Generic coefficient forms for the PDE and ODE, shown in Equations (60) and (61) respectively, are provided which the user may populate with the appropriate coefficients to create the desired equation.

$$e\frac{\partial^2 u}{\partial t^2} + d_a\frac{\partial u}{\partial t} + \nabla \cdot (-c\nabla u - \alpha u + \gamma) + \beta \cdot \nabla u + a_c u = f \tag{60}$$

$$e\frac{\partial^2 u}{\partial t^2} + d_a\frac{\partial u}{\partial t} = f \tag{61}$$

Table 6: Coefficient for generic PDE and ODE

Symbol	Description
e	mass coefficient
d_a	damping coefficient or mass coefficient
c	diffusion coefficient
α	conservative flux convection coefficient
β	convection coefficient
a_c	absorption coefficient
γ	conservative flux source term
f	source term

A COMSOL model may contain one or more components, which represent the geometry on which an equation or set of equations are to be solved. Equations are defined separately for each individual component.

All variables in COMSOL can be assigned with units which are input in square brackets immediately following the variable definition. All input units are converted internally to SI. Unit assignment provides a means of error checking for equation input. In the event of a unit mismatch in an equation (e.g. 300[K] – 0.2[m]), COMSOL will still perform the evaluation, however the equation will be highlighted in yellow in the variable definitions list to alert the user of a possible error in the equation definition.

COMSOL includes several types of variables and operators which can be used to define mathematical relationships. A brief introduction is provided below to assist in the explanation of the model implementation.

Parameters are global values which are position and time independent and apply to all components in the model. Parameters may be defined as a numerical value or as a function of other parameters. Parameters are evaluated once at the beginning of a model run and are not updated as the model progresses. Parameters may be used as to define geometry, mesh and solver setting. Parameters definitions can be defined using a parametric sweep, which facilitates running sensitivity studies and multiple inputs in a set of consecutive runs.

Variables are defined for individual components and may be global values or position dependent values defined on a volume, surface, boundary or point on the component geometry. Variables may be defined as a function of other variables, parameters and dependent variables, and are evaluated as required at each time step. Variables can be passed from one component to another through the use of coupling operators. Variables are evaluated only when required to calculate a dependant variable.

Coupling Operators are used to evaluate variables on a subset of a component geometry. Couplings operators such as maximum, minimum and average can be

used to perform operations on variables over a defined region. Coupling operators are also used to map variables from one component to another.

Functions are mathematical expressions which require one or more inputs to produce an output. Functions can be conditional operators such as min(), max() and if() statements. Functions such as interpolation and piecewise are defined in a tabular form and may be used, for example, to define a property lookup table. Some functions change the behaviour of COMSOL, such as the nojac() function, which instructs the solver to exclude the expression in brackets from the Jacobian matrix, which can under some conditions improve model performance by increasing the sparsity of the Jacobian matrix.

Dependent Variables are the solutions to the PDEs, ODEs and/or analytic equations which COMSOL is solving. Dependent variable are solved at each iteration and tested for convergence. They may be defined globally or on a volume, surface, edge or point.

A time-dependent solver is used in the model. At each time step, the program iterates the solution and compares the values of the dependent variables to the previous iteration. If the difference between the solutions at the current and previous iteration is below a specified tolerance, the solution is considered to be converged and the solver progresses to the next time step.

Time stepping in the model is controlled semi-automatically by an Implicit Differential-Algebraic (IDA) solver, which attempts to take the largest times step possible while still satisfying the defined tolerance. The solver setting in COMSOL allows the user to define a damping factor which reduces the step size at the first iteration of each time step, as well as a restriction in the maximum relative change in step size from one time step to the next.

A small time step is required when model parameters are changing quickly. This is particularly important at the start of a run due to pellet thermal expansion and initial contact with the sheath, and at a power ramp, when the pellet is expanding, iodine

production and diffusion is increasing and crack initiation can potentially occur. During the rest of the irradiation when parameters change more slowly a longer time step may be used. The time step size is controlled in the model by a series of four separate time intervals over which a time step is defined. A step size of 0.5 seconds is used for the first 10 seconds of the run. At the power ramp, the timestep is reduced and then gradually increased as time progresses. The parameters for time step control are listed in Table 7. The time-stepping algorithm in COMSOL is set to 'intermediate', which tells the solver to take smaller time steps if required to meet convergence criteria but not to exceed the defined time step size. Outside of the defined time step intervals, step size is limited by the parameter max_time_step.

Table 7: Time step parameters; time1 is the time of the power ramp

Parameter	Values for FFO-104 Reference Case
timestep_range1_start	0.5[s]
timestep_range1_size	0.5[s]
timestep_range1_end	10[s]
timestep_range2_start	time1-10[s]
timestep_range2_size	5[s]
timestep_range2_end	time1+2*ramping_time
timestep_range3_start	Timestep_range2_end
timestep_range3_size	10[s]
timestep_range3_end	time1+4*ramping_time
timestep_range4_start	timestep_range3_end
timestep_range4_size	60[s]
timestep_range4_end	time1+t_dwell
max_time_step	36*24*3600[s]
solver_initial_damping_factor	0.25
time1	3.38E7[s]
t_dwell	2.5*3600[s]

COMSOL terminates calculation when a maximum time is reached or the model reaches a defined stop condition. Stop conditions are defined for burnup and crack length, such that the model terminates if the simulation reaches the maximum burnup defined in the input or the crack length equals the sheath thickness, which indicates fuel sheath failure.

7.2 MODEL OVERVIEW

The model consists of 3 components. The relationship between them is illustrated in Figure 26. The x-axes in both components 1 and 2 represent pellet radius. The y-axis of component 1 represents axial length along the fuel element, while the y-axis of component 2 represents radial position in an idealized fuel grain, normalized to the average grain radius. Component 3 represents one half length of the fuel element.

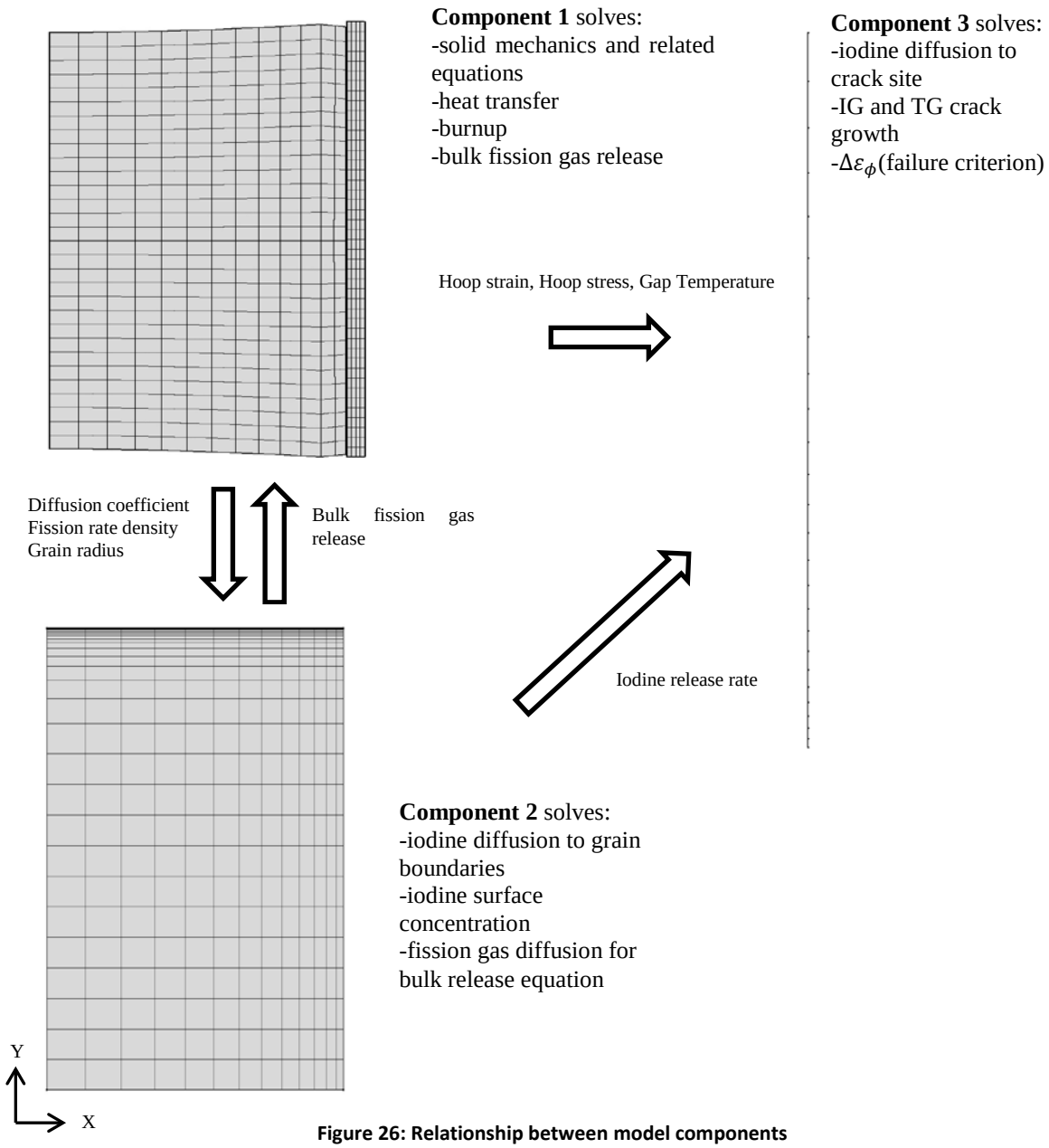

Figure 26: Relationship between model components

7.3 COMPONENT 1

Component 1 contains most of the FAST fuel performance model. A description of the geometry and the equations most relevant to the present model are described here. The model is essentially unchanged from the original model developed by A. Prudil, a full description of which is provided in [8], also in [9] [10].

7.3.1 GEOMETRY AND MESH

The model assumes azimuthal uniformity in the fuel element, allowing the geometry to be reduced to a 2-dimensional cross section symmetric across the pellet centreline. Furthermore, periodic symmetry is assumed in the axial direction (y-axis). While FAST has the capability of modelling a stack of multiple pellets, the single pellet configuration is used in the the present model to reduce computational demands. Axial periodic symmetry assumes that the element is composed of many identical pellets. This assumption precludes the modelling of end caps or axial variations in properties along the fuel element. A representation of the geometry for component 1 is shown in Figure 27, with the parameters used to define the geometry listed in Table 8.

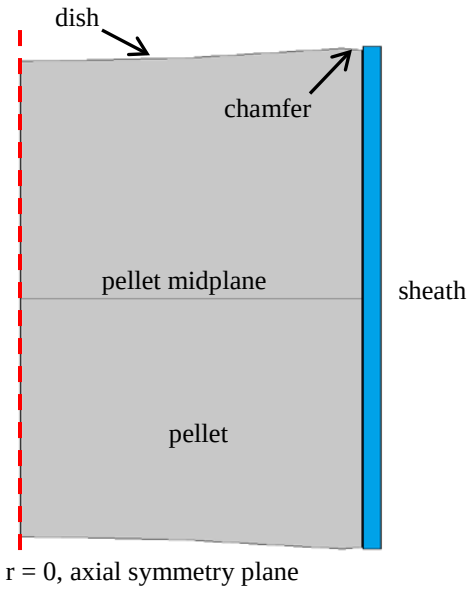

Figure 27: The geometry of component 1 showing the pellet and sheath geometry. The gap is not explicitly meshed.

Table 8: Parameters defining the pellet and sheath geometry

Parameter	Description	Values for 37e Fuel
pellet_radius	Radius of the UO2 pellet	6.105[mm]
pellet_hole_radius	Radius of a central hole in the pellet (typically used for thermocouples in experiments)	0[mm]
radial_chamfer	Length of the pellet chamfer in the radial direction	0.51[mm]
axial_chamfer	Length of the pellet chamfer in the axial direction	0.090[mm]
num_chamfer	Number of chamfered edges per pellet (1 is top only, 2 is top and bottom)	2
land_width	Size of the land between the chamfer and dish	0.0[mm]
dish_depth	Depth of the pellet dish	0.30[mm]
num_dish	Number of dished surfaces per pellet. (1 is top only, 2 is top and bottom)	2
pellet_length	Axial length of the pellet)	16.0[mm]
num_pellets	Number of pellets per element.	30
dish_radius	Radius of the dish sphere. Calculated from the pellet radius, radial chamfer and landwidth	(dish_depth^2+(pellet_radius-land_width-radial_chamfer)^2)/(2*dish_depth)
pellet_sheath_gap	Radial size of the initial pellet-to-sheath clearance	0.05[mm]/2
pellet_pellet_gap	Axial clearance between pellets measured land-to-land	3.56[mm]/num_pellets
sheath_internal_radius	Internal radius of the fuel sheath	pellet_radius+pellet_sheath_gap
sheath_thickness	Radial thickness of the fuel sheath wall	0.38[mm]

The finite element mesh for component 1 is composed of quadrilateral elements and is shown in Figure 28. The ‘mapped mesh’ function in COMSOL produces an evenly spaced mesh in the y-axis which is symmetric in the pellet mid plane. First order elements are used for all the dependent variables except for solid mechanics, which uses second order elements. The mesh density is finer in the radial direction near the pellet surface in order to resolve the steep gradients which occur there. The sheath is meshed with equally sized quadrilateral elements.

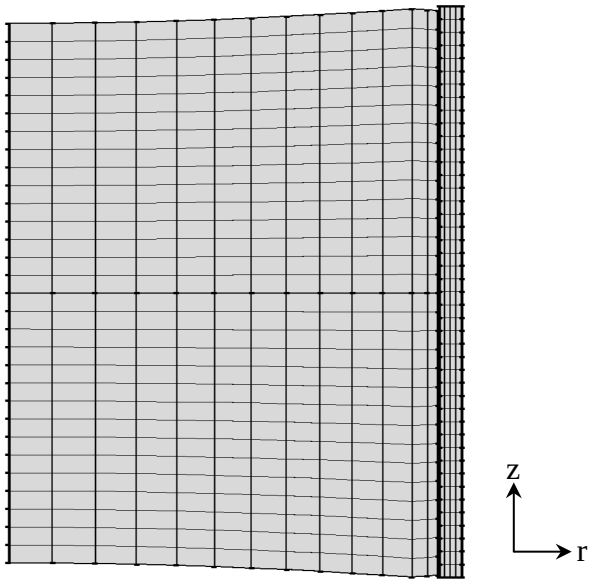

Figure 28: Mesh for component 1

7.4 COMPONENT 2

Component 2 represents the normalized fission grain radius in the y-axis and radial position in the fuel pellet in the x-axis; is a part of the original FAST model. The equations for iodine grain diffusion and surface concentration have been added to this component.

7.4.1 GEOMETRY AND MESH

The fission gas diffusion model is implemented on a 2-dimensional rectangle. This domain does not represent a 'real' geometry: the y-axis is defined between 0 and 1 and represents the normalized fuel grain radius, where y = 0 is at the centre of a spherical grain and y = 1 is the grain boundary. The x-axis represents radial position in the fuel pellet. For example, the top right corner of the domain represents the grain boundary at the pellet surface.

The finite element mesh for component 2 is composed of quadrilateral elements. Second order elements are used for all the equations. The mesh is fine in the y-axis

approaching the grain boundary, as steep gradients of iodine concentration are encountered in that region. The mesh in the x-axis becomes finer towards the pellet surface and corresponds roughly to the mesh density in the component 1 x-axis. The mesh is shown in Figure 29.

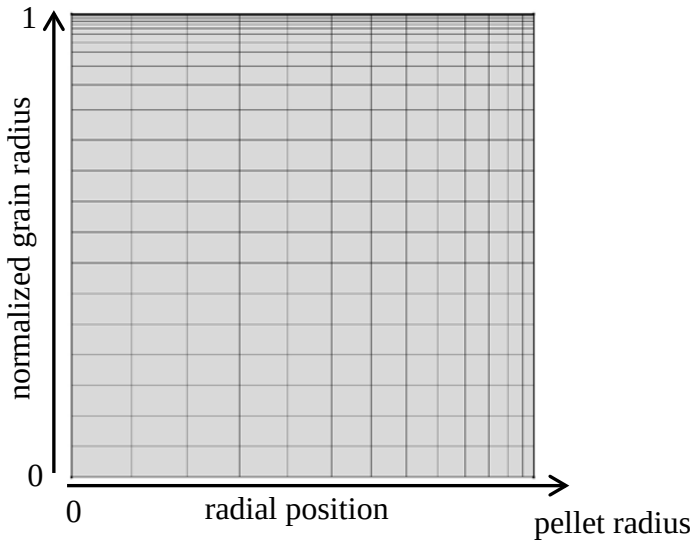

Figure 29: Geometry for component 2

7.4.2 VARIABLES

The variables defined in component 2 are listed in Table 9. These variables are defined at the point at the top right corner of the geometry which represents the grain boundary at the pellet surface.

In COMSOL a spatial derivative is defined by appending a variable with an axis label to indicate the plane of the derivative. For example the variable I_127_grain_concy is the y-axis gradient of the variable I_127_grain_conc.

The component coupling comp1.pellet_mid() is used to evaluate variables in component 1 along the pellet mid plane. The radial position along the pellet mid plane is

mapped to the x-coordinate in component 2, such that values for r=0 in component 1 are mapped to x=0 in component 2, and r=pellet radius in component 1 is mapped to x=pellet radius in component 2. The terms evaluated from component 1 are:

- UO2_grain_radius is the local average grain radius calculated by the FAST model, with units of meters.
- fission_rate_density is the volumetric fission rate calculated by FAST, which has units of m^{-3}.
- fg_diff_coeff is the fission gas diffusion coefficient, which has units [m^2 s^{-1}].

Table 9: Variables defined in component 2

Variable	Expression	Description
I127_release_at_gb	-3[m]*nojac(comp1.pellet_mid(fg_diff_coeff/(UO2_grain_radius)^2)*(I127_grain_concy))	Release rate of iodine 127 to the grain boundary
I129_release_at_gb	-3[m]*nojac(comp1.pellet_mid(fg_diff_coeff/(UO2_grain_radius)^2)*(I129_grain_concy))	Release rate of iodine 129 to the grain boundary
I131_release_at_gb	-3[m]*nojac(comp1.pellet_mid(fg_diff_coeff/(UO2_grain_radius)^2)*(I131_grain_concy))	Release rate of iodine 131 to the grain boundary
I133_release_at_gb	-3[m]*nojac(comp1.pellet_mid(fg_diff_coeff/(UO2_grain_radius)^2)*(I133_grain_concy))	Release rate of iodine 133 to the grain boundary
fg_release_multiplier	A1[m]*exp(-10.0754-0.05*comp1.linear_power[m/kW] +0.0012*comp1.linear_power^2[m^2/kW^2])	The fission gas release multiplier
A1	1.0+if(comp1.burnup_avg>40.8,(comp1.burnup_avg-40.8)/(72.4-40.8)*2.82,0) *if(comp1.burnup_avg>=72.4,0,1) +if(comp1.burnup_avg>=72.4,2.82,0)	The burnup-depend portion of the fission gas release multiplier
sum_I	fg_surface_grain_boundary(I127_surf+I129_surf+I131_surf+I133_surf)-Na_conc-(I_released/(2*pi*pellet_radius*element_length))	The summation of iodine concentration of fuel surface
CsI_surface_thickness	mol_mass_CsI/rho_CsI/N_avogadro* fg_surface_grain_boundary(sum_I)	Thickness of CsI surface layer
recoil_rate	0.25*fission_fragment_range*(2*pi*pellet_radius)*element_length*comp1.pellet_mid_avg(fission_rate_density)*particles_per_fission	Rate of fission fragment recoil at surface
I_net_release_rate	CsI_surface_thickness*recoil_energy_loss*CsI_decomp_energy*recoil_rate*comp3.crack_initiation_flag*radiolysis_multiplier	New Iodine released through radiolysis

7.4.3 GRAIN CONCENTRATION

Iodine isotopic concentration in the fuel grain, e.g. I127_grain_conc (m^{-3}), is defined in section 5.1.1 Equation (7). The equation is implemented using four PDEs, one for each of the isotopes of iodine tracked in the model. These equations are defined on component 2. The coefficients for the general form PDE for I-127 are listed in Table 10.

The diffusion coefficient is defined in matrix form to allow different diffusion rates in different directions. Since diffusion only occurs along the y-axis, c is defined only in position 2,2 of the matrix with the others being zero. Boundary conditions are zero flux at edge y=0 (representing the centre of the spherical fuel grain) and zero concentration at y=1 (representing release to the grain boundary). The initial concentration is zero for the entire domain.

Table 10: Coefficients for grain diffusion equation

e	0
d_a	y[1/m]^2*comp1.pellet_mid(UO2_grain_radius[1/m])^2
a	lambda_I127*(y[1/m])^2*comp1.pellet_mid(UO2_grain_radius[1/m])^2
f	Yield_I127*(y[1/m])^2*comp1.pellet_mid(UO2_grain_radius[1/m])^2*fission_rate_density
c	$\begin{pmatrix} 0 & 0 \\ 0 & y[1/m]\text{^}2 * \text{nojac}(\text{comp1.pellet\_mid}(\text{fg\_diff\_coeff})) \end{pmatrix}$

7.4.4 SURFACE CONCENTRATION

The surface isotopic concentration of iodine, e.g. I127_surf (m^{-2}) is defined by Equation (12) in Section 5.1.2 as the time integral of iodine release rate at the pellet surface. For the surface release model only the iodine concentration at the surface of the pellet is required, therefore the equation is evaluated at the point y=1, r=pellet_radius. The concentration equations for the four iodine isotopes tracked in the model are implemented as four point ODEs. The coefficients for the general form ODE for I-127 are defined in Table 11. The initial concentration is zero.

Table 11: Coefficient for the surface concentration ODE

e	0
d_a	1
f	I127_release_at_gb*fg_release_multiplier-lambda_I127*I127_surf

7.4.5 TOTAL IODINE RELEASED

The cumulative amount of iodine released from the fuel surface, I_released (no units) is expressed in Equation (18) in Section 5.1.3. It is implemented as a point ODE evaluated at the y=0 at the pellet surface. The coefficients for the generic ODE are defined in Table 12. The initial value of I_released is 0.

Table 12: Coefficient for the total iodine released ODE

e	0
d_a	1
F	I_net_release_rate

7.5 COMPONENT 3

Component 3 represents the length of the fuel element over which iodine may diffuse to a crack site. The crack site is located at the centre of the element, which results in the shortest diffusion distance and is therefore represents the worst case scenario. This assumption also allows symmetry to be used to model only half of the length of the element.

7.5.1 GEOMETRY AND MESH

The diffusion of iodine in the fuel-sheath gap is defined on a 1-dimensional domain representing one half length of the fuel element, where x = 0 is the crack site at the centre of the element. The mesh is composed of second order elements and becomes finer closer to the crack site at the element centre. The mesh in relation to the fuel element is shown Figure 30.

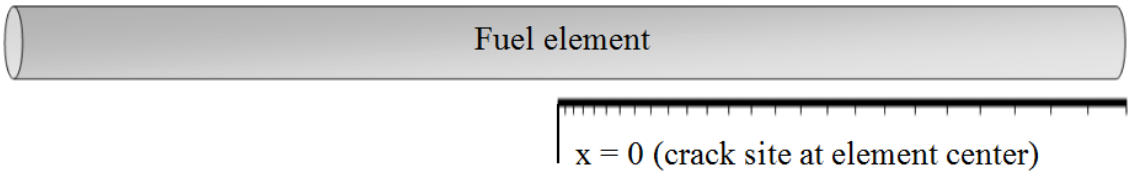

Figure 30: Component 3 mesh in relation to fuel element

7.5.2 VARIABLES

The variables defined in component 3 are listed in Table 13, Table 14 and for domain, boundary and global variables.

The variables in Table 13 are defined along the length of component 3. A maximum function is used in the definition of the gap release rate equations in order to prevent a divide by zero error; on model initiation, when sum_I evaluates to 0, the divisor evaluates to eps, which is the smallest real number which COMSOL can define (~2.22×10^{-16}). This value is small enough that it has a negligible impact on model results. The coupling operator comp2.fg_surface_grain_boundary() passed values from component 2 evaluated at the point y=1, r=pellet_radius.

Table 13: Component 3 variables defined on domain

gap_diffusion_coeff	0.0018583*sqrt(comp1.pellet_surface_avg(T[K^-3])^3 *((1/M_He)+(1/M_I2)))/(p*omega_AB*sigma_AB^2)*1[cm^2/s*K^3]
I127_gap_release_rate	comp2.fg_surface_grain_boundary(I_net_release_rate)/(element_length *2) *comp2.fg_surface_grain_boundary(I127_surf)/max(comp2.fg_surface_grain_boundary(sum_I),eps)
I129_gap_release_rate	comp2.fg_surface_grain_boundary(I_net_release_rate)/(element_length *2) *comp2.fg_surface_grain_boundary(I129_surf)/max(comp2.fg_surface_grain_boundary(sum_I),eps)
I131_gap_release_rate	comp2.fg_surface_grain_boundary(I_net_release_rate)/(element_length *2) *comp2.fg_surface_grain_boundary(I131_surf)/max(comp2.fg_surface_grain_boundary(sum_I),eps)
I133_gap_release_rate	comp2.fg_surface_grain_boundary(I_net_release_rate)/(element_length *2) *comp2.fg_surface_grain_boundary(I133_surf)/max(comp2.fg_surface_grain_boundary(sum_I),eps)

The variables in Table 14 are defined only at the crack site, point x=0. As discussed in Section 7.4.2, appending a variable name with an axis label denotes a spatial derivative, thus I127_gapx denotes the derivative of the variable I127_gap with respect to x.

Table 14: Component 3 variables defined at crack site

I_crack	2*gap_diffusion_coeff*(I127_gapx+I129_gapx+I131_gapx+I133_gapx)
ZrI4_crack	0.5*I_crack*reaction

The variables in Table 15: Component 3 global variables are defined globally (they are not position dependant). The variable K_geo_factor points to the interpolation function geo_factor_Rt20() or geo_factor_Rt15() depending on the value of the parameter bundle_type (bundle_type = 0 indicates a 28 element bundle while 1 indicates

37 element fuel). These functions point to interpolation tables which defines the stress intensity geometric factor based on the crack depth to sheath thickness ratio (Table 16 and Table 17) [34]. The function y=flc1hs(a,b) is a Heaviside function which evaluates to 0 at a-b=0 and 1 at a+b=0, with a smooth transition in between. This function is used to stabilize the transitions between crack growth regimes, as an instantaneous step from 0 to 1 tends to cause convergence problems. The variable strain_rate is the source term for the calculation of the total change in strain at the power ramp, d_strain; it is evaluated if the model time is greater than or equal to the ramp time. The variable sheath_stress is defined as a minimum function which limits the sheath stress to the yield stress of Zircaloy-4, defined by the interpolation function zirc_yield(T). The variable crack_initiation_flag initiate the crack growth model based on the correlations for crack initiation defined in Section 5.3. The variables IG_growth_flag and TG_growth_flag define the transition between crack growth regimes and are used to turn on and off their respective crack growth equations. The variable failure_flag evaluates to 1 when the crack length reaches the sheath thickness or the stress intensity exceeds the fracture toughness, at which point the model is terminated by a stop condition.

Table 15: Component 3 global variables

crack_initiation_flag	flc1hs(d_strain>=critical_dstrain,1,0),0.1)
critical_dstrain	(CANLUB_thickness==0)*(-1.06E-3+0.677/ramp_burnup) +(CANLUB_thickness>0)*(ramp_burnup<=250)*((0.003105+0.503/ramp_burnup)+0.0001) +(CANLUB_thickness>0)*(ramp_burnup>=500)*(-1.06E-3+0.677/ramp_burnup) +(CANLUB_thickness>0)*(ramp_burnup>250)*(ramp_burnup<500) *(((2-ramp_burnup/250)*(0.003105+0.503/ramp_burnup+0.0001))+(((ramp_burnup/250)-1)*(-1.06E-3+0.677/ramp_burnup)))
IG_growth_flag	crack_initiation_flag*abs(TG_growth_flag-1)
K1	K_geo_factor*sheath_stress*(pi*crack_site(crack_length[m^-1]))^0.5
TG_growth_flag	flc1hs(K1[m^2/N]-K_scc,0.01)*(crack_site(crack_length)>crack_length_initial)
TG_growth_rate	max(eps,3E-7*log(K1[m^2/N]/1E6)[m/s]-1E-8[m/s])
failure_flag	if(K1>=K1c_zircaloy||crack_length>=sheath_thickness,1,0)
K_geo_factor	(bundle_type==0)*(geo_factor_Rt_20(comp3.crack_site(crack_length)/sheath_thickness)) +(bundle_type==1)*(geo_factor_Rt_15(comp3.crack_site(crack_length)/sheath_thickness))
IG_crack_length	(2*crack_vol/(pi*crack_width))^0.5
crack_length	IG_crack_length+TG_crack_length+crack_length_initial
IG_crack_vol_ initial	pi/2*crack_width*crack_length_initial^2
strain_rate	comp1.sheath_inside_surface_max(ut/pellet_radius)*flchs(t[s^-1]-time1[s^-1],0.001)
sheath_stress	min(zirc_yield(comp1.sheath_inside_surface_max(T)),comp1.sheath_inside_surface_max(solid.sp1))

Table 16: Geometric factors for K evaluation, 28 element fuel [41]

a/t	f(t)
0	0.684
0.08	0.692
0.2	0.704
0.3	0.714
0.4	0.725
0.5	0.735
0.6	0.745
0.7	0.755
0.8	0.766
0.9	0.775
1.0	0.785

Table 17: Geometric factors for K evaluation, 37 element fuel [41]

a/t	f(t)
0	0.707
0.08	0.716
0.2	0.730
0.3	0.742
0.4	0.755
0.5	0.767
0.6	0.780
0.7	0.793
0.8	0.808
0.9	0.821
1	0.835

7.5.3 GAP DIFFUSION

Concentration of iodine in the fuel-sheath gap, I127_gap (m^{-1}), is defined in Equation (29) Section 5.5.1. This equation is implemented as a series of four PDEs, one for each of the iodine isotopes tracked in the model. The coefficients of the general form PDE for I-127 are shown in Table 18. The initial value of the dependent variables are 0 everywhere. A concentration of 0 is assumed at x=0, representing a perfect sink at the

crack site. A no flux condition at x = element_length/2 represents the solid boundary of the sheath end cap.

Table 18: Coefficient for gap diffusion PDE

e	0
d_a	1
A	lambda_I127
f	I_I127_gap_release_rate
c	gap_diffusion_coeff

7.5.4 DELTA HOOP STRAIN ($\Delta\varepsilon_\phi$)

The change in hoop strain at the ramp, d_strain, is defined in Equation (24) in Section 5.3. The integral is implemented as a global ODE, for which the coefficients are defined in Table 19. The variable strain_rate evaluates to zero before the time of the power ramp.

Table 19: Coefficients for the component 3 ODE for change in strain at ramp

e	0
d_a	1
f	strain_rate

7.5.5 CRACK LENGTH

Crack growth in the intergranular region is predicted by the removal of zirconium from the crack site. A mass balance equation for the zirconium leaving the crack site gives the volume of the crack. The volume is then related to crack length through the IG_crack_length variable in Table 15, assuming the semi-circular crack of width 0.5 μm as detailed in Section 5.5.1. The volume of intergranular crack growth, IG_crack_vol (m^3), is defined in Equation (37). The integral is implemented as a point ODE defined at the crack site x=0. The coefficients for the ODE are defined in Table 20. The initial value IG_crack_vol_initial is based on the user defined initial_crack_length.

Table 20: Coefficients for component 3 ODE for intergranular crack volume

e	0
d_a	1
f	(M_Zr/(rho_Zr*N_avogadro))*crack_site(ZrI4_crack)*IG_growth_flag

The length of the transgranular crack growth region, TG_crack_length (m), is defined in section 5.5.2 by Equation (41) as the time integral of the crack growth rate. It is implemented with a point ODE evaluated at the crack site. The coefficients for the ODE are defined in Table 21. The initial value is zero. Note that the source term evaluates to zero unless the TG_growth_flag is set to 1.

Table 21: Coefficients for component 3 ODE for transgranular crack velocity

e	0
d_a	1
f	TG_growth_flag*TG_growth_rate

8 MODEL VERIFICATION AND SENSITIVITY STUDIES

In the following sections the model is benchmarked against a single available in-reactor power ramp test with well-defined SCC failure time. As there is limited data on SCC failure time in-reactor, a series of sensitivity studies are conducted. These sensitivity studies employ a series of multiplier values which modify the behaviour of different portions of the model. These multipliers are not based on robust theoretical arguments; rather, they demonstrate the sensitivity of the model to changes to different equations, particularly where simplifying assumptions have been made. The results of these studies suggest areas to focus further experimental effort.

Mesh density and time step sensitivity studies are also described.

8.1 CRACK GROWTH TIME VERIFICATION

Ideal model verification would involve comparison of the model predictions against a series of in-reactor power ramp experiments with well-defined failure times. However the failure time for SCC occurring in elements operating in power reactors is not well known. The failure of a fuel element is detected either by radiation sensors in the coolant loop or by coolant sampling and chemical analysis. Detection will not occur until sometime after the element has failed and the coolant activity has reached the detection threshold. The power history database in Appendix B lists dwell times for some of the elements, although this would represent only a rough estimate of failure time.

One well-defined SCC failure time for an in-reactor element is available. Power ramp test FFO-104 was conducted in the X-2 experimental loop of the NRX reactor at Chalk River Laboratories. The test used a fuel design similar to a 37 element fuel bundle; sheath inner diameter was 12.105 mm with a wall thickness of 0.43 mm and a 'thick' layer of CANLUB was applied to the inside surface [12]. The element was irradiated previously to a burnup of 240 MWh $kg(U)^{-1}$ at a power of approximately 30 kW m^{-1}. After a preconditioning period at 30 kW m^{-1}, during which the element achieved a burnup of 278 MWh $kg(U)^{-1}$, the fuel was ramped to a power of 58 kW m^{-1}. A fuel

element failure was detected by an increase in radioactivity in the coolant. The failure time was determined to be approximately 20 minutes after the ramp. The circulation time for the loop was approximately 100 seconds, which gives reasonable certainty in the estimated failure time [26] [58].

The model was set up to run the power history for FFO-104. This initial 'reference' study used the model as described in Chapter 5, without any of the modifications described in the sensitivity studies in the following sections. The input file is provided in Appendix C. The model is run at a power of 30 kW m^{-1} up to a burnup of 278 MWk kgU^{-1}, after which the power is increased to 58 kW m^{-1}. As the ramp rate for the test was not available a ramp time of 20 seconds was assumed, which corresponds to the assumed ramp time for the Pickering elements in the power history database. A maximum timestep of 36 hours was imposed for the pre-ramp period, while a maximum timestep of 5 s is imposed shortly before the start of the power ramp.

The reference model of test FFO-104 predicts a failure time of 14.7 minutes. Cracking begins when $\Delta\varepsilon_{\phi}$ exceeds the threshold value, which occurs approximately 18 s after the start of the ramp. Most of the failure time constitutes the transgranular cracking period, as shown in Figure 31. As discussed in Section 6.3 the intergranular crack growth rate predicted by the model is much higher than would be expected from experimental observations. Therefore a series of sensitivity studies examining key model assumptions were performed to assess how the failure time can be increased to the experimentally measured 20 minutes. These studies are detailed in the next section.

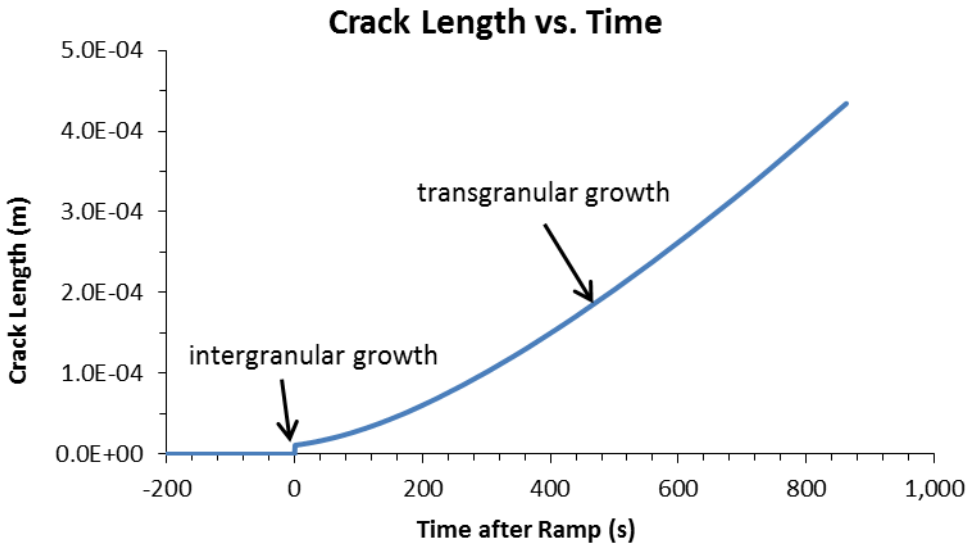

Figure 31: Crack growth prediction for reference run of test FFO-104, t=0 is the start of the power ramp

8.2 Sensitivity to Crack Growth Parameters

8.2.1 Radiolysis Model Sensitivity

The radiolysis model predicts the release of iodine from cesium iodide deposits on the fuel surface. The model assumes that recoiling fission fragments escaping the fuel surface encounter a uniform, monolithic layer of CsI. For the reference run of FFO-104 the calculated surface deposit thickness is approximately 7 nm at the time of the power ramp, which is much smaller than the average range of fission fragments in UO_2 of approximately 7 µm.

In this study, the release rate of iodine from the fuel surface was reduced by inserting a multiplying factor M_{recoil} into Equation (17) for iodine release from the fuel surface:

$$R_{I,} = (M_{recoil} R_{rec}) Y_I \frac{dE}{dx} x_{CsI} \tag{62}$$

A value of M_{recoil} of less than 1.0 simulates a reduced interaction rate between the recoiling fission products and the CsI layer, which reduces the iodine release rate R_I. The results of a sensitivity study on this parameter are shown in Table 22. The results indicate that a reduction to a recoil rate of between 10^{-4} and 10^{-5} would be required to achieve a failure time close to the reported 1200s. This reduction results in an intergranular growth rate on the order of 10^{-8} m s^{-1} which is in the range of $5x10^{-9}$ to $2x10^{-7}$ m s^{-1} estimated in literature (see Section 6.3).

Table 22: Sensitivity study of radiolysis model on intergranular growth rate

M_{recoil}	IG_growth rate avg (m s^{-1})	Failure Time (s)
1.0 (reference)	$3.15x10^{-5}$	881
0.1	$7.21x10^{-6}$	881
0.01	$1.60x10^{-6}$	885
0.001	$3.44x10^{-7}$	910
0.0001	$7.56x10^{-8}$	1028
0.00001	$1.70x10^{-8}$	1581

8.2.2 Absorption Coefficient Sensitivity

A major assumption of the model is that once iodine is released from the fuel it does not redeposit on fuel surfaces, recombine with Cs, or interact with the sheath except at the crack site. Examination of failed fuel sheaths reveal evidence of pitting and small surface flaws in iodine SCC laboratory tests [37], indicating that iodine is interacting all along the inner surface of the sheath.

The interaction of iodine with the fuel and sheath surfaces would be expected to be a function of iodine concentration and can be modelled simplistically as an absorption term in the gap diffusion equation. To study the impact of this parameter the absorption term M_{absorb} was added to Equation (29) to simulate iodine depositing on the sheath and/or fuel as it diffuses through the gap region:

$$\frac{\partial C_{gap,i}}{\partial t} = D_{AB}\frac{\partial^2 C_{gap,i}}{\partial x^2} - (\lambda_i + M_{absorb})C_{gap,i} + R_{gap,i} \quad (63)$$

A value of M_{absorb} greater than 0 increases the rate of iodine loss as it diffuses along the fuel-sheath gap length. The results of a sensitivity study on this parameter are shown in Table 23. The results indicate that a value of M_{absorb} on the order of 10,000 s^{-1} results in a failure time approaching the measured 1200 s.

Table 23: Sensitivity study of absorption coefficient on intergranular growth rate

Multiplier Value (s^{-1})	IG_growth rate avg (m s^{-1})	Failure Time (s)
0.0 (reference)	$3.15x10^{-5}$	881
1.0	$2.99x10^{-5}$	881
10	$1.77x10^{-5}$	881
100	$3.35x10^{-6}$	882
1000	$3.73x10^{-7}$	907
10000	$3.97x10^{-8}$	1170

A high absorption term results in numerical instability in the gap diffusion equation with the default mesh density. Iodine concentration becomes essentially constant across most of the sheath and drops off only very close to the crack site, creating a very steep gradient which results in oscillations in the concentration values around the mesh points. For values of M_{absorb} greater than 100 s^{-1} it was necessary to refine the component 3 mesh by increasing the number of mesh points by a factor of 3 and as well as doubling the element growth factor so that the mesh points cluster more toward the crack site.

8.2.3 Sensitivity of Reaction Rate at Crack Tip

The model assumes an instantaneous reaction at the crack tip. The $Zr_{(s)} + 2I_{2(g)} \rightarrow ZrI_{4(g)}$ reaction is thermodynamically favourable and would be expected to occur rapidly. However other factors may impact the reaction rate at the crack tip. The SCC crack in Figure 10 shows significant pitting along the crack face, indicating iodine is reacting with the crack walls as well as the crack tip.

While a proper reaction rate equation would be based on the iodine concentration at the crack site, this would require modification of the boundary conditions of the gap diffusion equation. In order to demonstrate the impact of a reduction in reaction rate in a simple manner, the reaction multiplier term $M_{reaction}$ is implemented, which reduces the portion of iodine reaching the crack site which reacts to form ZrI_4. It is implemented in the code by modifying Equation (36):

$$R_{Zr} = \frac{1}{2}\left(R_{crack,T}\right)M_{reaction} \tag{64}$$

A $M_{reaction}$ value of less than 1.0 reduces the portion of iodine which reaches the crack tip. The results of a sensitivity study on this parameter are shown in Table 24. The results show that a reduction to between 10^{-4} and 10^{-5} of iodine reacting would produce a failure time close to the experimental 1200s.

Table 24: Sensitivity study of the reaction rate at the crack tip

$M_{reaction}$	IG_growth rate avg (m s^{-1})	Failure Time (s)
1.0 (reference)	$3.15x10^{-5}$	881
0.01	$1.60x10^{-6}$	885
0.001	$3.47x10^{-7}$	910
0.0001	$7.56x10^{-8}$	1028
0.00001	$1.63x10^{-8}$	1579

8.2.4 Impact of Multiple Crack Sites

Another important assumption of the model is that a single crack site exists at which iodine reacts. PIE reveals multiple incipient SCC cracks in addition to the failure location [17]. A sensitivity study was performed assuming that several crack sites are present at each pellet interface plane. This is illustrated in Figure 32.

For this study the domain of component 3 was shortened from half of an element length to half of one pellet length and the term n_{crack} is introduced to Equation (37) to

divide the reacting iodine between the numerous active crack sites. The length of the crack in the intergranular growth phase is then:

$$a_{crack,IG} = \left(\frac{2}{\pi w} \frac{M_{Zr}}{\rho_{Zr} N_A} \int_{t,ramp}^{t,dwell} \frac{R_{Zr}}{n_{cracks}} dt \right)^{0.5} \quad (65)$$

The results of the study are presented in Table 25. The results indicate that while the inclusion of multiple crack sites reduces intergranular crack growth rates, it has very little impact on the overall failure time.

Table 25: Sensitivity study on number of crack sites

n_{cracks}	IG_growth rate avg (m s^{-1})	Failure Time (s)
Ref	3.16×10^{-5}	881
5	1.16×10^{-5}	881
10	7.25×10^{-6}	881
20	4.63×10^{-6}	882

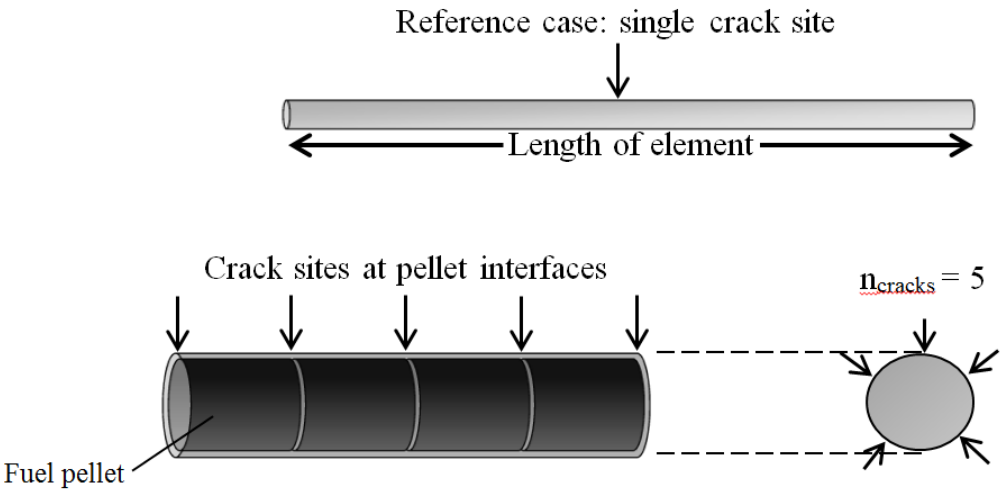

Figure 32: Arrangement of crack sites for reference study and crack site sensitivity study

8.2.5 CRACK SHAPE SENSITIVITY

In the reference analysis a semi-circular crack shape is assumed, however Figure 23 in Section 6.4.4 shows an SCC crack which is much longer than its width. Therefore a sensitivity study was conducted to determine the impact of the crack shape on failure time. The crack shape is defined by the ratio of depth to base-length, a/c, as illustrated in Figure 33. The crack width (the out of plane dimension in Figure 33) remains constant at 0.5 μm.

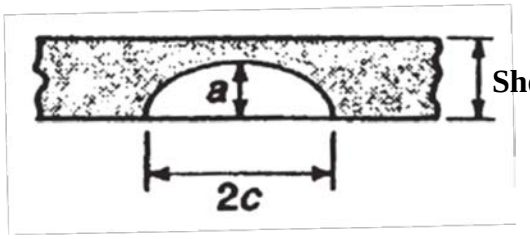

Figure 33: Crack shape is defined by crack depth a and base length c [41]

The crack shape impacts the intergranular growth time in the model in two ways. First, it changes the geometric factor, F, in Equation (38) in the calculation of stress intensity and therefore influences the critical crack depth required to achieve K_{ISCC}. Second, it changes the volume-to-depth ratio of crack and therefore the amount of iodine required to increase the depth of the crack through mass removal.

Two additional crack shapes were modeled in the study, with a/c ratios of 0.6 and 0.2. The tables of geometric factors for these shapes are included in Appendix D. Equation (37) for intergranular crack length is modified by including the ratio a/c:

$$a_{crack,IG} = \left(\frac{2}{\pi w} \left(\frac{a}{c}\right) \frac{M_{Zr}}{\rho_{Zr} N_A} \int_{t,ramp}^{t,dwell} R_{Zr}\, dt \right)^{0.5} \tag{66}$$

The results of the study are presented in Table 26. For lower values of a/c the average intergranular crack velocity decreases slightly because of the larger volume of the crack, however the change in the geometric factor reduces the critical crack length

and the increases the speed of crack growth in the transgranular region. The overall result is a decrease in failure time.

Table 26: Sensitivity study on crack shape

a/c	Critical crack length (μm)	IG_growth rate avg (m s^{-1})	TG_growth_rate_avg (m s^{-1})	Failure Time (s)
Ref 1.0	10.9	$3.16x10^{-5}$	$4.91x10^{-7}$	881
0.6	7.32	$3.50x10^{-5}$	$5.70x10^{-7}$	763
0.2	5.31	$3.78x10^{-5}$	$6.67x10^{-7}$	656

8.2.6 Conclusion of Sensitivity Studies

The sensitivity studies have shown that several of the model assumptions influence the faster than expected failure time of the reference case. Modifications to each of the radiolysis, gap absorption and reaction rate terms were able to reduce the intergranular crack growth rate to within the range estimated in experiments. Reducing the intergranular growth rate to approximately $4.0x10^{-8}$ m s^{-1}, which is within the range of experimental evidence, yielded a failure time close to the 20 minutes observed in the test, which suggests the relative velocities of the crack growth mechanisms are being modelled correctly.

The sensitivity study on multiple active crack sites showed that multiple crack sites did not significantly reduce the failure time. However the number of crack sites may be more significant when combined with other modifications listed above. Modifying the crack shape by assuming a smaller depth to length ratio was shown to decrease the failure time by increasing the growth rate in the transgranular cracking region.

While these studies have examined the impact of the parameters individually, a combination of these factors represents a better physical solution. For example, a study was conducted with $M_{radiolysis} = 0.05$, $M_{absorb} = 200$, $M_{react} = 0.1$, $n_{cracks} = 5$ and $F = 0.6$ which yielded a failure time of 20.3 minutes. This combination of values is simply a guess; more realistic values could be obtained through further experimental and theoretical analysis, as discussed in Chapter 9.

8.3 IMPACT OF THE CANLUB MODEL

The CANLUB layer is modelled assuming that iodine reacts preferentially with sodium impurities, thus there is little iodine available to cause SCC until the sodium is completely reacted. A study was performed on test FIO-104 with and without CANLUB to assess its impact on failure time. The results of the study are shown in Table 27. At the time of the power ramp the iodine concentration on the fuel surface is reduced by approximately 20% by the presence of the CANLUB, however this does not translate into a significant change in intergranular crack growth. The reduction in failure time is due to a higher intergranular crack length. The lower threshold value for the non-CANLUB case results in earlier crack initiation; the stress is lower at this earlier initiation time, therefore the crack must grow deeper to reach K_{ISCC}. Because the intergranular growth rate is very high this results in an overall shorter failure time.

The CANLUB model delays the accumulation of iodine on the fuel surface. In the test a zero iodine concentration is predicted up to a burnup of 122MWh $kg(U)^{-1}$, therefore the model would predict no failure before that burnup.

Table 27: Sensitivity to CANLUB

	Sum_I at power ramp (atoms)	IG growth rate avg. ($m\ s^{-1}$)	Failure time (s)
CANLUB	$5.05x10^{19}$	$3.16x10^{-5}$	881
Non-CANLUB	$6.67x10^{19}$	$3.21x10^{-5}$	856

8.4 MESH SENSITIVITY STUDIES

The finite element method provides a numerical solution to a set of equations by discretizing the model geometry into a mesh of small elements with simple geometries on which the equations are solved. Dependant variables are solved for explicitly at the node points; values in between node points are interpolated based on equations called shape functions to provide a continuous solution. Because the equations are only solved at the mesh points, an improperly designed mesh has the potential to adversely impact

model results. A key factor in a well-designed mesh is a sufficient density of elements to resolve the gradients of the solution variables.

The selection of mesh density requires a balance between accuracy and solution time. A coarse mesh produces a smaller system of equations to solve and thus reduces solution times, but it may be unable to adequately resolve solution gradients or localized effects, leading to inaccurate results. On the other hand a very fine mesh will require increased computational effort due to a larger system of equations, which may lead to unacceptably long solution times. An ideal mesh would be the coarsest one for which the solution does not change appreciably when the mesh is made finer.

In order to test for mesh dependence a sensitivity study was performed by evaluating FFO-104 with 400%, 150%, 50% and 25% of the reference model mesh density. Study results for a set of relevant solution variables are presented in Table 28. The results show that there is not a significant change in results when the mesh is made finer, which suggests that the reference mesh is appropriately sized.

Table 28: Mesh density sensitivity study

Mesh Density	Pre-ramp Hoop Strain (%)	%diff	Sum_I (atoms)	% diff	IG_growth rate avg (m s^{-1})	% diff
400%	0.510	-0.1%	$5.06x10^{-19}$	0.2%	$3.27x10^{-5}$	3.8%
150%	0.517	1.2%	$5.06x10^{19}$	0.2%	$3.17x10^{-5}$	0.6%
Ref	0.511	---	$5.05x10^{19}$	---	$3.15x10^{-5}$	---
50%	0.497	-2.7%	$5.04x10^{19}$	-0.2%	$2.54x10^{-5}$	-19%
25%	0.487	-4.7%	$5.03x10^{19}$	-0.4%	$2.62x10^{-5}$	-17%

8.5 TIME STEP SENSITIVITY

Similar to geometric discretization, the time dependant solution is also discretized in time, with the solution being defined at discrete time steps. The selection of time step size can impact results, particularly at power ramps when parameters are changing on a short time-scale. Selecting too long of a time step can result in the model not properly resolving time-dependant gradients, while short time steps can significantly increase run

times. Time step size is to some degree controlled by the solver and the scheme used in the model is described in Section 7.1.

Two sensitivity studies were conducted. In the first study, the maximum time step taken prior to the power ramp was varied by 50%. Table 29 shows several important pre-ramp parameters: the pre-ramp strain, the centreline temperature, and the surface iodine concentration. The results do not change significantly for the shorter or longer timestep, which indicates that the reference timestep of 24 hours is sufficient and could be increased to 36 hours, which would reduce run times.

Table 29: Max time step before ramp study

Max Timestep	Pre-ramp strain	Pre-ramp centreline T (K)	Pre-ramp surface iodine concentration (atoms m^{-2})
12h	0.005114	1380.9	$5.05x10^{19}$
24h (ref)	0.005111	1380.9	$5.05x10^{19}$
36h	0.005113	1380.9	$5.05x10^{19}$

In the second study the maximum time step at the power ramp was varied by 50%. The results of the study are presented in Table 30 showing the maximum stress and iodine release rates following the ramp, as well as the failure time for each case. The results do not change significantly, which indicates that the reference timestep of 5 seconds is suitable.

Table 30: Timestep at Ramp study

Timestep a Ramp (s)	Max iodine release rate (atoms s^{-1})	Failure Time (s)
5s (ref)	$6.162x10^{15}$	881
10.0s	$6.163x10^{15}$	881
2.5s	$6.160x10^{15}$	881

9 DISCUSSION

9.1 TIME TO FAILURE MODEL

There is a fair degree of uncertainty in the failure time calculation in the model. A number of simplifying assumptions are made with regard to iodine transport and intergranular crack growth, which produces a much faster intergranular growth rate than would be expected based on experimental evidence. While a faster growth rate is conservative, the goal of a mechanistic model is to accurately account for the factors which impact crack growth. Some of the important model assumptions were explored in a series of sensitivity studies in Chapter 8, which suggest several areas for future investigation.

Failure time was shown to be sensitive to the radiolysis, absorption and reaction rate coefficients. These model parameters could be addressed by a more detailed model of iodine interaction with the fuel and sheath surfaces. While this is a very complex problem involving many chemicals, a starting point could be a model for recombination with Cs on the fuel surface.

While the sensitivity study showed that the number of crack sites had little impact on model results, this parameter may have more of an impact when combined with other parameters listed above. SCC cracks are typically observed to occur above cracks in the fuel pellet [17], therefore the number of active crack sites could be correlated with the number of cracks in the pellet. As previously noted the modelling of pellet cracking is a complex problem, although some progress has been made in this area using the cohesive zone model. This method involves placing ‘cohesive surfaces’ along potential crack paths in the fuel pellet, which begin to separate when the principle stress reaches the fracture strength [59]. While it is not able to reproduce all the effects of pellet cracking, this method may serve to provide an estimate of the number of pellet fragments and therefore the number of active crack sites.

9.2 THRESHOLD CORRELATIONS AND CANLUB

From the perspective of power reactor operations, modelling the time to failure of a fuel element is of secondary importance; the more important goal is to prevent fuel failure while still being able to operate the reactor economically. The threshold correlation developed in Section 6.2.4 for change in hoop strain at the power ramp was shown to be more accurate at discerning failure vs non-failure conditions than the FUELOGRAM-based correlations used in the previous Kleczek/Lewis model.

The analysis of the power history database in Section 6.2 shows much more severe mechanical conditions are required to induce SCC in low burnup fuels compared to laboratory tests. It seems likely that the more limiting factor early in the life of the fuel is iodine availability as opposed to mechanical limits. In the model, the assumption that iodine reacts preferentially with the CANLUB sodium impurities results in zero concentration of iodine at lower burnups and thus no SCC failures. It is expected that NaI in the gap undergoes radiolysis in a similar fashion to CsI, thus radiolysis and recombination for both these species could be part of a more detailed model of the chemical interactions in the gap, which would allow for a more realistic prediction of iodine concentrations.

The treatment of CANLUB as a chemical getter due to impurities may not account completely for its impact on fuel performance; an understanding of the exact role of CANLUB in preventing SCC is clearly needed.

9.3 FAILURE PROBABILITY

From the power history database there are clear instances where one fuel bundles experience SCC failure while a similar bundle having a similar power history does not fail by SCC. There appears to be a probabilistic aspect to SCC occurrence.

Probability models have been suggested by various authors. For example in the SCC model of Jernkvist, a critical crack size for SCC is determined based on sheath

stress, and a statistical analysis of manufacturing data determines the probability of a defect of the critical size existing on fuel sheath surface and therefore the probability of SCC failure [60]. A similar type of probabilistic fracture mechanics methodology is used for failure prediction in nuclear reactor piping systems by codes such as PRAISE (Pipe Reliability Analysis Including Seismic Events) [61].

Previous work has been performed at RMCC on statistical analysis of fuel manufacturing data [62]. The difficulty of implementing this type of methodology is that, in the present model, the absence of an initial surface flaw does not preclude SCC initiation because intergranular crack growth may occur from a smooth surface.

The FUELOGRAM correlations determine the SCC failure probability by evaluating, for a given interval of burnup and power, the percentage of failed vs. intact elements in a database of power histories. A similar approach could potentially be adopted for the threshold correlations in the present model. However, the number of intact power histories for non-CANLUB coated fuels in the database is insufficient to draw statistically meaningful conclusions. It is noted that the FUELOGRAM correlations are based on a larger database of power histories than what is presently available in the open literature [7].

9.4 Factors not Considered in Model

The chemistry of the fuel-sheath gap is a complex environment. There are other factors which influence the occurrence of SCC which are not considered in the model. These are beyond the scope of this work but could represent areas for future improvement.

9.4.1 Incubation Time

Experiments have demonstrated an incubation period for SCC, which is believed to be the time required to develop the correct chemical conditions at the crack tip to

initiate growth (detailed in section 5.4). However the exact mechanisms involved in the initiation process of SCC remains poorly understood. Research in this area is ongoing, such recent work from Los Alamos National Laboratory which investigates, from a theoretical perspective, the interaction of iodine with the oxide layer and zirconium at a molecular level, including the formation and fracture of ZrI_x films on sheath surface [36]. While the most recent published results do not provide a useful model for crack initiation, future developments in this area will be of interest for SCC modelling efforts.

9.4.2 OXYGEN POTENTIAL

After cracking due to power ramp strain, the oxide layer on the inside surface of the sheath has the potential to regrow by reacting with any oxygen available in the fuel-sheath gap. This will re-passivate the sheath and mitigate iodine corrosion. The re-passivation rate would be expected to depend on oxygen availability and temperature [63]. While it may be expected that most oxygen remains in the fuel as hypo-stoichiometric UO_{2+x}, a model of the oxygen available in the gap would provide a means of assessing the potential for re-passivation.

9.4.3 HYDROGEN

Hydrogen has been considered in the model with respect to its impact on reducing the fracture toughness of the sheath. If hydrogen is present in sufficient concentrations, zirconium hydrides may form, which can serve as initiation sites for SCC [37]. Hydriding is especially significant when a decrease in temperature reduces the hydrogen solubility limit, causing some of the dissolved hydrogen to precipitate in a ZrH phase. Modelling of hydrogen concentration would be useful for SCC and could also be used to predict delayed hydride cracking failures.

9.4.4 TEXTURE

Texture has been demonstrated to have an important effect on SCC [17]. Transgranular cracking occurs preferentially along basal planes, therefore the degree to which these planes align with the crack growth direction strongly impacts SCC susceptibility [39]. The power history database does not at present contain information on sheath texture. By examining the failure conditions of sheaths with different textures a new texture dependant value of K_{ISCC} could be implemented in the model.

9.5 ADDITIONAL AREAS FOR FUTURE IMPROVEMENT

The mechanical response of the fuel sheath is influenced by the pellet shape, including the size of the dishes and chamfers [64]. For the power reactor elements in the power history database the pellet geometry is well known. However for the research reactor power histories non-standard pellet sizes are used; in the analysis for threshold failure values the dish and chamfer sizes had to be estimated based on power reactor fuel design. If a more detailed pellet geometry were available for these data points a more accurate qualification of sheath mechanical state could be made, which may or may not impact the definition of the failure threshold.

The calculated SCC threshold values are only as accurate as the fuel performance model used to derive them. While FAST has been shown to compare favourably to existing IST codes, further improvements could be made. For example, a multi-pellet implementation of FAST has been developed [9]. Extension of the model to include the element end caps could improve results by more accurately capturing the axial loading resulting from constrained axial expansion.

The model of crack growth could be carried past sheath rupture to calculate crack opening displacement in the sheath and the ingress of coolant into the element. Previous work at RMCC on defect fuel modelling [65] [66] could be incorporated to create a more

complete model of fuel behaviour and estimate the radiological consequences of an SCC event.

10 SUMMARY AND CONCLUSION

Modelling of SCC is a complicated problem due to the complexity of the chemical environment in nuclear fuel, the difficulty of recreating reactor conditions in laboratory and the lack of a clear understanding of all the exact mechanisms involved in SCC in-reactor. The model presented in this thesis builds on the ISCC model developed by Kleczek and Lewis and the FAST model of Prudil. Several aspects of the model have been improved:

The FAST fuel performance model has been integrated to provide mechanical analysis of the fuel sheath system within a single code. In the Kleczek/Lewis model the mechanical condition of the fuel were not explicitly modeled.

The crack initiation thresholds are now based on mechanical parameters as opposed to power levels. This approach was shown to be more accurate at distinguishing between failure and non-failure cases in the power history database than the FUELOGRAM-based correlations used in the Kleczek/Lewis model.

The empirical diffusion coefficient for iodine release has been replaced with the more mechanistic diffusion coefficient used in FAST. This model was benchmarked against the results of a series of in-reactor sweep gas tests to produce a surface release multiplier term which correlate predicted and experimentally observed release rates.

A model of transgranular crack propagation has been implemented based on a fracture mechanics analysis of the growing crack. Threshold stress intensity and crack growth rates are based on values reported from laboratory tests of irradiated materials.

Benchmarking the model against power ramp test FFO-104 conducted at the NRX reactor yields a failure time prediction of approximately 14 minutes. By adjusting parameters related to simplifying assumption in the iodine transport model, the failure time can be made to match the 20 minutes observed in the test. This represents an improvement over the Kleczek/Lewis model.

Areas in which the model could be improved include, in particular, a more detailed chemical analysis of the fuel-sheath gap which could provide a better model of iodine diffusion to a crack site. An improved understanding of the initiating mechanism for SCC and the role of the CANLUB layer would also greatly benefit model efforts.

The COMSOL report for the implemented model for this thesis is provided in Appendix E.

11 REFERENCES

[1] Independant Electricity Supply Operator, "Supply Overview," [Online]. Available: http://www.ieso.ca/imoweb/media/md_supply.asp. [Accessed 13 2 2015].

[2] Canadian Nuclear Association, "CANDU technology," CNA, 2013. [Online]. Available: https://cna.ca/technology/energy/candu-technology/. [Accessed 08 04 2015].

[3] Cameco Inc., "Uranium 101," Cameco Inc., [Online]. Available: http://www.cameco.com/uranium_101/uranium_science/nuclear_fuel/. [Accessed 27 March 2013].

[4] S. Wenhui and A. Manzer, "CANDU Fuel Performance," AECL, Shanghai Nuclear Design and Research Institute, Available online: https://canteach.candu.org/Content%20Library/20054409.pdf.

[5] D. Urjan, "Foreign Material Exclusion Program at CNE Cernavoda Nuclear Generating Station," in *International Youth Nucelar Congress*, Interlaken, Switzerland, 2008.

[6] R. Sejnoha, "Hydrogen Gas in CANDU Fuel Elements," in *CANDU Fuel Conference*, Niagara Falls, 1999.

[7] W. Penn, R. Lo and J. Wood, "CANDU Fuel - Power Ramp Performance Criterion," *Nuclear Technology*, vol. 34, pp. 249 - 268, 1977.

[8] A. Prudil, "FAST: A Fuel And Sheath modeling Tool for CANDU Fuel," PhD Thesis, Royal Military College of Canada, Kingston, 2014.

[9] A. Prudil, B. Lewis, P. Chan and J. Baschuk, "Developement and testing of the FAST fuel performance code: Normal operating conditions (Part 1)," *Nuclear Engineering and Design*, vol. 282, pp. 158-168, 2015.

[10] A. Prudil, B. Lewis, P. Chan, J. Baschuk and D. Wowk, "Development and testing of the FAST fuel performance code: Transient conditions (Part 2)," *Nuclear Engineering and Design*, vol. 282, pp. 169-177, 2015.

[11] M. Kleczek, "Thermodynamic and Kinetic Modelling of Iodine Induced Stress Corrosion Cracking in Nuclear Fuel Sheathing, M.A.Sc Thesis," Royal Military Colllege of Canada, Kingston, Canada, 2010.

[12] B. Lewis, W. Thompson, M. Kleczek, K. Shaheen, M. Juhas and F. Iglesias, "Modelling of iodine-induced stress corrosion cracking in CANDU fuel," *Journal of Nuclear Materials*, vol. 408, pp. 209-223, 2010.

[13] R. Cottis, "Guides to Good Practice in Corrosion Control - Stress Corrosion Cracking," National Physical Laboratory, 2000.

[14] R. W. Hertzberg, Deformation and Fracture Mechanics of Engineering Materials, Hoboken, New Jersey: John Wiley & Sons Inc., 1996.

[15] M. Tayal, M. Floyd, D. Rattan, A. Xu, J. Manzer and E. Kohn, "Load-Following Performance and Assessment of CANDU Fuel," in *6th International Conference on CANDU Fuel*, Niagara Falls, Canada, 1999.

[16] IAEA, "Fuel failure in water reactors: Causes and mitigation," in *Proceedings of the Technical Meeting*, Bratislava, Slovakia, June 2002.

[17] B. Cox, "Pellet-Cladding Interatction (PCI) Failures of Zirconium Alloy Fuel Cladding - A Review," *Journal of Nuclear Materials*, vol. 172, pp. 249-292, 1990.

[18] R. daSilva, "CAFÉ: A Probabilistic Model for Predicting CANDU Fuel Power Ramping Performance," in *unpublished Ontario Hydro CNS report*, December 1986.

[19] R. daSilva, "CAFE - A Probabilistic Model for Predicting CANDU Fuel SCC Power Ramp Failures," in *Third International Conference on CANDU Fuel*, Pembroke, Ontario, 1992.

[20] M. Tayal, K. Hallgrimson, J. MacQuarria, P. Alavi, S. Seto, K. Y. and T. Nishimura, "INTEGRITY: A Semi-Mechanistic Model for Stress Corrosion Cracking of Fuel," AECL-10792, 1994.

[21] EPRI, "Fuel Analysis and Licensing Code: Falcon Mod01, Theoretical and Numerical Bases, vol. 1," 2006.

[22] J. Turnbull, A. Friskney, R. Findlay, F. Johnson and A. Walter, "The diffusion coefficients of gaseous and volatile species during the irradiation of uranium dioxide," *Journal of Nuclear Materials*, vol. 107, p. 168–184, 1982.

[23] C. Friskney, J. Turnbull, F. Johnson, A. Walter and J. Findlay, "The characteristics of gas release from monocrystalline uranium dioxide during irradiation," *Journal of Nuclear Materials*, vol. 68, p. 186–192, 1977.

[24] J. Turnbull, C. Friskney, F. Johnson, A. Walter and J. Findlay, "The release of radioactive gases from uranium dioxide during irradiation," *Journal of Nuclear Materials*, vol. 67, pp. 301-306, 1977.

[25] R. White and M. Tucker, "A new fission gas release model," *Journal of Nuclear Materials*, vol. 118, pp. 1-38, 1983.

[26] B. Lewis, C. Hunt and F. Iglesias, "Source Term of Iodine and Noble Gas Fission products in the Fuel-to-Sheath Gap of Intact Operating Nuclear Fuel Elements," *Journal of Nuclear Materials*, vol. 172, pp. 197-205, 1990.

[27] D. Olander, Fundamental Aspects of Nuclear Reactor Fuel Elements, Oak Ridge, Tennessee: ERDA Technical Information Center, 1976.

[28] S. Shann and D. Olander, "Stress Corrosion Cracking of Zircaloy by Cadmium, Iodine, and Metal Iodides," *Journal of Nuclear Materials*, vol. 113, pp. 234-248, 1983.

[29] P. Sidky, "Iodine stress corrosion cracking of Zircaloy reactor cladding: iodine chemistry (a review)," *Journal of Nuclear Materials,* vol. 256, pp. 1-17, 1998.

[30] B. Lewis, "Fission product release from nuclear fuel by recoil and knockout," *Journal of Nuclear Materials,* vol. 148, p. 28, 1987.

[31] N. Marchal, C. Campos and C. Garnier, "Finite element simulation of Pellet-Cladding Interaction (PCI) in nuclear fuel rods," *Computational Materials Science,* vol. 45, pp. 821-826, 2009.

[32] SCDAP/RELAP5-3D Code Development Team, "SCDAP/RELAP5-3D© CODE MANUALVOLUME 4: MATPRO - A LIBRARY OF MATERIALS PROPERTIES FOR LIGHT-WATER-REACTOR ACCIDENT ANALYSIS," Idaho National Engineering and Environmental Laboratory, Idaho Falls, 2003.

[33] M. Floyd, "Extended-Burnup CANDU Fuel Performance," in *7th International CNS CANDU Fuel Conference*, Kingston, Ontario, 2001.

[34] B. Cox, "Environmentally-Induced Cracking of Zirconium Alloys - A review," *Journal of Nuclear Materials,* vol. 170, pp. 1-23, 1990.

[35] A. Garlick and P. Wolfenden, "Fracture of Zirconium Alloys in Iodine Vapour," *Journal of Nuclear Materials,* vol. 41, pp. 274-292, 1971.

[36] C. D. T. Matthew L. Rossi, "First-principles insights into the nature of zirconium–iodine interactions and the initiation of iodine-induced stress–corrosion cracking," *Journal of Nuclear Materials,* vol. 458, pp. 1-10, 2015.

[37] S. Park, J. Kim, M. Lee and Y. Jeong, "Effects of Microstructure and alloying elements on the iodine-induced stress-corrosion cracking behaviour of nuclear fuel claddings," *Journal of Nuclear Materials,* vol. 376, pp. 98-107, 2008.

[38] M. Fregonese, C. Olagnon, N. Godin, A. Hamel and T. Douillard, "Stain-hardening influence on iodine induce stress corrosion cracking of zircaloy-4," *Journal of Nuclear Materials,* vol. 373, pp. 59-70, 2008.

[39] I. Schuster, C. Lemaigna and J. Jacques, "Testing and modelling the influence of irradiation on iodine-induced stress corrosion cracking of Zircaloy-4," *Nuclear Engineering and Design,* vol. 156, pp. 343-349, 1995.

[40] R. Haddad and B. Cox, "On the Initiation of Cracks in Zircaloy Tubes by I2 and Cs/Cd Vapours," *Journal of Nuclear Materials,* vol. 138, pp. 81-88, 1986.

[41] A. Liu, "Summary of Stress-Intensity Factors," in *ASM Handbook Volume 19, Fatigue And Fracture (ASM International),* ASM International, 1996, pp. 980-991.

[42] The Electric Power Research Institute, "Fracture Toughness Data for Zirconium Alloys," ERPI, Palo Alto, 2001.

[43] T. Lampman and P. Gillespie, "Cracking in Used CANDU Fuel Bundles during Dry Storage," Nuclear Waste Management Organization, Toronto, 2010.

[44] I. Hastings, C. Hunt, J. Lipsett and R. Delaney, "Shirt-lived Fission Product Release from UO2: Annular versus Solid Pellets," *Journal of Nuclear Materials,* vol. 135, pp. 115-121, 1985.

[45] G. Pastore and e. al., "Uncertainty and sensitivity analysis of fission gas behavior in engineering-scale fuel modeling," *Journal of Nuclear Materials,* vol. 456, pp. 398-408, 2015.

[46] UNENE, "The Essential CANDU - A Textbook about the CANDU Reactor," 11 12 2014. [Online]. Available: http://www.nuceng.ca/candu/.

[47] B. Cox and R. Haddad, "Recent Studies of Crack Initiation During Stress Corrosion Cracking of Zirconium Alloys," in *Zirconium in the Nuclear Industry: Seventh International Symposium*, Strasbourg, France, 1985.

[48] F. Yaggee, R. Mattas and L.A.Neimark, "Characterization of Irradiated Zircaloys: Suseptibility to Stress-Corrosion Cracking," Electric Power Research Institute, Palo Alto, California, 1979.

[49] S. Park, J. Kim, M. Lee and Y. Jeong, "Stress-corrosion crack initiation and propagation behavior of Zircaloy-4 cladding under an iodine environment," *Journal of Nuclear Materials,* vol. 372, pp. 293-303, 2008.

[50] H. Knaab, M. Gartner and F. Sontheimer, "KWU'S Experimental Basis FOR POWER RAMPING AND CYCLING PERFORMANCE OF LWR FUEL," in *Power Ramping, Cycling and Load Following Behaviour of Water Reactor Fuel: Proceedings of the Technical Committee Meeting Organized by the IAEA*, Lyon, France, 1987.

[51] R. Williford, "The Iodine-Induced Strain Rate Sensitivity of Zircaloy Fuel Rod Cladding," *Nuclear Engineering and Design,* vol. 78, pp. 23-36, 1984.

[52] T. Carter and P. Fehrenbach, "The Load Following Capability of CANDU Fuel," AECL-7098, Chalk River, Ontario, 1983.

[53] R. Jones, D. Cubicciotti and B. Syrett, "Effects of test temperature, alloy composition, and heat treatment on iodine-induced stress corrosion cracking of unirradiated zircaloy tubing," *Journal of Nuclear Materials,* vol. 91, pp. 277-292, 1980.

[54] R. J. D. Cubicciottim S.M. Howard, *Journal of Nuclear Materials,* vol. 78, p. 2, 1978.

[55] P. Chan and K. Kaddatz, "How Does CANLUB Work?," in *15th Annual Conference of the Canadian Nuclear Society*, Toronto, 1994.

[56] T. Do, K. G. Irving and W. H. Hocking, "Microchemical study of high-burnup CANDU® fuel by imaging-XPS," *Journal of Nuclear Materials,* vol. 383, pp. 34-40, 2008.

[57] P. Chan, "Protective Coating to Reduce Stress Corrosion Cracking in Zirconium Alloy Sheathing". United States Patent CA9600907, 8 09 1998.

[58] B. Lewis, Interviewee, *Private Correspondence.* [Interview]. 04 12 2014.

[59] R. W. D. Knoll, "Simulating Dynamic Fracture in Oxide Fuel Pellets Using Cohesive Zone Models," in *20th International Conference on Structural Mechanics in Reactor Technology (SMiRT 20)*, Espoo, Finland, 2009.

[60] L. Jernkvist, "A Model for Predicting Pellet-cladding Interaction-Induced Fuel Rod Failure," *Nuclear Engineering and Design*, vol. 156, pp. 393-399, 1995.

[61] G. Holman and C. Chou, "Probability of Failure in BWR Coolant Piping Vol 1, NUREG/CR-4792," Lawrence Livermore National Laboratory , Livermore, California, 1988.

[62] T. Cunning, P. Chan, M. D. Pandey and A. Pant, "An Examination of CANDU Fuel Performance Margins Derived from a Statistical Assessment of Industrial Manufacturing Data," *Nuclear Technology*, vol. 187, pp. 270-281, 2014.

[63] L. Jeurgens, A. Lyapin and E. Mittemeijer, "The initial oxidation of zirconium - oxide-film microstructure and growth mechanism," *Surface and Interface Analysis*, vol. 38, pp. 727-730, 2006.

[64] T. Carter, "Experimental Investigation of Various Pellet Geometries to Reduce Strains in Zirconium Alloy Cladding," *Nuclear Technology*, vol. 45, pp. 166-176, 1979.

[65] K. Shaheen, "A thermomechanical model of CANDU fuel, MASc Thesis," Royal Military College of Canada, 2007.

[66] J. Higgs, B. Lewis, W. Thompson and Z. He, "A conceptual model for the fuel oxidation of defective fuel," *Journal of Nuclear Materials*, vol. 366, pp. 99-128, 2007.

[67] S. Mettu, I. Raju and R. Forman, "Stress Intensity Factors for Part-Through Surface Cracks in Hollow Cylinders," Lockheed Engineering & Service Company and Nasa Johnson Space Centre, July 1992.

APPENDICES

APPENDIX A: DERIVATION OF DIFFUSION COEFFICIENT

The derivation of the diffusion coefficient for fission gas in the UO_2 implemented in the FAST code is presented here. The following derivation is largely reproduced from [8].

Net diffusion of fission gas atoms through the solid UO_2 matrix is given by:

$$D = \frac{D_0 b'}{b' + g_a} \tag{67}$$

where b' is the intergranular resolution rate (s^{-1}), g_a is the trapping rate (s^{-1}) and D_0 is the single atom diffusion coefficient for a full density UO_2 crystal . b' and g_a are defined as:

$$b' = 3.03\pi F_{rate} l_f (R_b + Z_0)^2 \tag{68}$$

$$g_a = 4\pi R_B D_0 \left(\frac{1.52\alpha_{fgb}}{\pi l_f (R_B + Z_0)^2} \right) \tag{69}$$

where l_f is the average distance travelled by a fission fragment in the fuel, $\alpha_{fgb} \approx 12$ is the number of fission gas bubbles which are nucleated by each fission event and Z_0 is the average range of the impact of the fission spike. R_B is the average radius of the intragranular pores:

$$R_B = 5x10^{-10} \left(1 + 106\, exp\left(\frac{-8702.7}{T} \right) \right) \tag{70}$$

D_0 is calculated as the weighted sum of the diffusion coefficients due to three difference mechanisms:

$$D_0 = D_{thermal} + 4D_{irr} + 4D_{athermal} \tag{71}$$

Where $D_{thermal}$, D_{irr} and $D_{athermal}$ are the diffusion coefficients due to thermal processes, irradiation induced vacancies and athermal processes, respectively, all in units of $m^2 s^{-1}$. They are defined as:

$$D_{thermal} = 7.6x10^{-9} exp\left(\frac{-2.93x10^5}{R_g T}\right) \tag{72}$$

$$D_{irr} = 10^{13}\Omega^{2/3} C_v^0 \frac{\Omega^{2/3}\mu_s^2 + Z_n C_v^0}{2Z_n} \sqrt{1 + \frac{2x10^6 F_{rate}\Omega Z_n}{v_n(\Omega^{2/3}\mu^2 + Z_n C_v^0)}} \tag{73}$$

$$D_{athermal} = 2x10^{-40} F_{rate} \tag{74}$$

Where R_g=8.314 J K^{-1} mol^{-1} is the ideal gas constant, T is temperature (K), Ω is the atomic volume in m^3 given by:

$$\Omega = \frac{M_U}{\rho_{UO2STP} N_A} \tag{75}$$

C^0_v is the vacancy concentration of unirradiated UO_2 and is given by:

$$C_v^0 = exp\left(\frac{-27780}{T}\right) \tag{76}$$

$\mu_s = 10^{15}\,m^{-2}$ is the sink strength for crystallographic point defect, $v_v = 10^{13} C^0_v$ is the vacancy jump frequency, $Z_n \approx 100$ is the average number of sites available for recombination around defect which will inevitably recombine, F_{rate} is the fission rate density, $M_U = 238.03$ g mol^{-1} is the molar mass of natural uranium, $\rho_{STPUO2} = 10980$ kg m^3 is the density of UO_2 at STP and N_A is Avogadro's number.

APPENDIX B: DATABASE OF SCC POWER HISTORIES

The power history database is presented here along with the calculated change in strain at the power ramp and failure predictions for the ISCC and $\Delta\varepsilon_{\phi,c}$ threshold criteria. The database has been separated into non-CANLUB and CANLUB fuels.

NON-CANLUB

Identification	Sheath Inner Diameter (mm)	Burnup (MWh kg(U)$^{-1}$)	Initial Power (kW m^{-1})	Ramped Power (kW m^{-1})	Dwell Time (h)	Failure?	Calculated $\Delta\varepsilon_{\phi}$	ISCC Correct?	$\Delta\varepsilon_{\phi}$ Threshold Correct?
D.P.(103)	14.409	85	27.4	43.9	2.5	NO	0.533556	NO	YES
D.P.(117)	14.409	82	26.2	44.7	2.5	NO	0.607383	NO	YES
D.P.(137)	14.409	50	28.6	49.4	2.5	NO	0.745726	YES	YES
D.P.(170)	14.409	89	23.5	46.1	2.5	NO	0.76089	NO	NO
D.P.(230)	14.409	185	20.2	31.1	2.5	NO	0.284212	YES	NO
D.P.(243)	14.409	178	27.1	38.3	2.5	NO	0.337128	NO	NO
D.P.(269)	14.409	159	25.2	35.8	2.5	NO	0.300924	NO	YES
D.P.(282)	14.409	196	21.9	31.2	2.5	NO	0.246374	YES	NO
D.P.(296)	14.409	210	24.8	37.4	2.5	NO	0.377272	NO	NO
D.P.(307)	14.409	215	26.9	37.3	2.5	NO	0.314866	NO	NO
D.P.(318)	14.409	219	25.8	35.9	2.5	NO	0.298031	NO	NO
D.P.(328)	14.409	256	24.5	34.7	2.5	NO	0.300581	NO	NO
D.P.(331)	14.409	243	24.8	36.2	2.5	NO	0.34216	NO	NO
D.P.(334)	14.409	240	24.9	36.9	2.5	NO	0.363612	NO	NO
D.P.(347)	14.409	231	24.6	36.4	2.5	NO	0.352126	NO	NO
D.P.(75)	14.409	83	27.1	42.7	2.5	NO	0.493446	NO	YES
PNGS-1/1972/OE/01	14.409	51	12.6	43.5	0.3	NO	0.897859	YES	YES
PNGS-1/1972/OE/06	14.409	46	9.8	45.8	0.3	NO	1.064237	YES	YES
PNGS-1/1972/OE/08	14.409	52	8.8	46.3	0.3	NO	1.10647	YES	YES
PNGS-1/1972/OE/10	14.409	119	24.8	41.6	0.3	NO	0.500929	YES	NO
PNGS-1/1972/OE/11	14.409	124	23.8	42.1	0.3	NO	0.545404	YES	NO
PNGS-1/1972/OE/15	14.409	54	13.6	48.4	0.3	NO	1.089453	YES	YES
PNGS-1/1972/OE/16	14.409	56	13.6	42.8	0.3	NO	0.842032	YES	YES
PNGS-1/1972/OE/17	14.409	97	25.8	45.8	0.3	NO	0.629752	YES	NO
PNGS-1/1972/OE/22	14.409	107	22.1	43.3	0.3	NO	0.634862	YES	NO
D.P.(357)	14.409	225	21.9	34.7	2.5	YES	0.363702	NO	YES

D.P.(358)	14.409	213	21.6	34.9	2.5	YES	0.375603	YES	YES
D.P.(359)	14.409	212	28.1	40.7	2.5	YES	0.404072	YES	YES
D.P.(360)	14.409	205	22.2	35.5	2.5	YES	0.378781	YES	YES
D.P.(361)	14.409	200	23.1	35.1	2.5	YES	0.340259	YES	YES
D.P.(362)	14.409	199	25	40.6	2.5	YES	0.490254	YES	YES
D.P.(363)	14.409	189	26.2	41.6	2.5	YES	0.4925	YES	YES
D.P.(364)	14.409	170	28.9	41.7	2.5	YES	0.408304	YES	YES
D.P.(365)	14.409	172	27.4	44.3	2.5	YES	0.564022	YES	YES
D.P.(366)	14.409	150	28.8	45.9	2.5	YES	0.583618	YES	YES
D.P.(368)	14.409	151	34.1	44.3	2.5	YES	0.353923	YES	YES
D.P.(369)	14.409	150	34.8	44.6	2.5	YES	0.345997	YES	YES
D.P.(375)	14.409	102	25.3	53.5	2.5	YES	1.079431	YES	YES
Exp-NPD-3709/BX/OE	14.330	104	24.21	51.65	2.5	YES	1.016835	YES	YES
NRU(01)	14.409	224	53.5	68.8	2.5	YES	0.717386	YES	YES
NRU(02)	14.409	207	22.9	54.4	2.5	YES	1.236353	YES	YES
NRU(03)	14.409	196	42.4	61.7	2.5	YES	0.914468	YES	YES
NRU(04)	14.409	179	42.3	62.6	2.5	YES	0.964521	YES	YES
NRU(05)	14.409	109	27.6	57.8	2.5	YES	1.228951	YES	YES
NRU(06)	14.409	107	37.7	56.5	2.5	YES	0.830486	YES	YES
NRU(16)	14.409	46	45.9	73.6	2.5	YES	1.372429	YES	YES
PNGS-1/1972/OE/02	14.409	131	24.5	54	0.3	YES	1.027051	YES	YES
PNGS-1/1972/OE/03	14.409	135	26.5	58.3	0.3	YES	1.17547	YES	YES
PNGS-1/1972/OE/04	14.409	138	26.3	52.2	0.3	YES	0.888152	YES	YES
PNGS-1/1972/OE/05	14.409	145	27.7	56.1	0.3	YES	1.029809	YES	YES
PNGS-1/1972/OE/07	14.409	50	9.8	54.3	0.3	YES	1.480779	YES	YES
PNGS-1/1972/OE/09	14.409	58	12.9	53.2	0.3	YES	1.340082	YES	YES
PNGS-1/1972/OE/12	14.409	129	24.8	49.1	0.3	YES	0.794062	YES	YES
PNGS-1/1972/OE/13	14.409	133	23.5	47.2	0.3	YES	0.750836	YES	YES
PNGS-1/1972/OE/14	14.409	137	24.6	47.6	0.3	YES	0.73678	YES	YES
PNGS-1/1972/OE/18	14.409	134	25.8	48.4	0.3	YES	0.734689	YES	YES
PNGS-1/1972/OE/19	14.409	137	27.1	52.8	0.3	YES	0.891692	YES	YES
PNGS-1/1972/OE/20	14.409	144	25.6	49.3	0.3	YES	0.781574	YES	YES
PNGS-1/1972/OE/21	14.409	152	29.3	55.2	0.3	YES	0.932804	YES	YES
PNGS-1/1972/OE/23	14.409	126	27	47.5	0.3	YES	0.662872	YES	YES
PNGS-1/1972/OE/24	14.409	128	25.6	47.6	0.3	YES	0.70623	YES	YES
PNGS-1/1972/OE/25	14.409	132	26.9	48.7	0.3	YES	0.714133	YES	YES

PNGS-1/1972/OE/26	14.409	134	27.9	46.9	0.3	YES	0.611462	YES	YES
PNGS-1/1972/OE/27	14.409	136	27.9	51.5	0.3	YES	0.805108	YES	YES
PNGS-1/1972/OE/28	14.409	137	29.1	50.5	0.3	YES	0.724194	YES	YES

CANLUB

Identification	Sheath Inner Diameter (mm)	Burnup (MWh kg(U)$^{-1}$)	Initial Power (kW m^{-1})	Ramped Power (kW m^{-1})	Dwell Time (h)	Failure?	Calculated $\Delta\varepsilon_{\varphi}$	ISCC Correct?	$\Delta\varepsilon_{\varphi}$ Threshold Accurate?
BDL-402/NS/02 PA7	12.184	81	32	45	>2.5	NO	0.440163	YES	YES
BDL-402/NS/O3 PA8	12.191	81	32	62	>2.5	NO	1.318676	NO	NO
BDL-406/ PA10	12.221	218	39	48	>2.5	NO	0.371765	NO	YES
BDL-406/ PA9	12.242	170	30	36	>2.5	NO	0.1741	YES	YES
BDL-406/AAM (12)	12.251	124	5.244	20.064	>2.5	NO	0.293321	YES	YES
BDL-406/GH (07)	12.251	155	9.823	30.283	>2.5	NO	0.507543	YES	YES
BDL-406/XY (10)	12.251	223	8.253	31.573	>2.5	NO	0.605466	YES	NO
BDL-406/ZN (11)	12.251	157	4.603	17.633	>2.5	NO	0.269972	YES	YES
BDL-406/ZR (09)	12.251	270	7.696	29.446	>2.5	NO	0.558331	YES	NO
BDL-412/KD/IE PA1	13.735	360	28	40	>2.5	NO	0.41343	NO	YES
BDL-412/KD/OE PA1	13.735	465	40	52	>2.5	NO	0.549665	NO	NO
BDL-412/KE/IE PA1	13.735	365	28	54	>2.5	NO	1.138838	NO	NO
BDL-412/KF/02 (16)	13.7363	448	49	68.7	>2.5	NO	0.849888	NO	NO
BDL-412/KF/IE PA15	13.735	392	28	40	>2.5	NO	0.419162	NO	YES
BDL-412/KF/OE PA16	13.7363	448	49	68.7	>2.5	NO	0.95255	NO	NO
BDL-414/SA/IE PA1	14.369	51	20.88	40.89	>2.5	NO	0.61412	YES	YES
BDL-414/SA/OE PA1	14.379	99	34.8	68.73	>2.5	NO	1.562421	NO	NO
BDL-415/AAA/IE PA1	12.223	79	21	50	>2.5	NO	1.06223	NO	NO
BDL-415/AAA/OE PA	12.223	96	22.62	53.07	>2.5	NO	1.169954	NO	NO
BDL-415/AAB/IE PA2	12.223	87	21	51	>2.5	NO	1.115463	NO	NO
BDL-415/AAB/OE PA	12.223	106	23.49	53.94	>2.5	NO	1.187081	NO	NO
BDL-416/AAV/22 PA2	12.222	52.1	20.43	42.63	>2.5	NO	0.710528	YES	YES
BDL-416/AAW/06 PA3	12.215	155	57.12	70.22	>2.5	NO	0.536302	NO	YES
BDL-416/AAW/11 PA3	12.215	155	57.12	70.22	>2.5	NO	0.536302	NO	YES
BDL-416/AAW/22 PA2	12.222	104	42.48	51.156	>2.5	NO	0.378726	YES	YES
BDL-416/PA27	12.222	101	33	43	>2.5	NO	0.346855	YES	YES

BDL-416/PA29	12.215	142	36	61	>2.5	NO	1.170959	NO	NO
BDL-416/PA32	12.914	142	36	61	>2.5	NO	1.164135	NO	NO
BDL-418/AAZ/IE PA3	12.222	88	23	46	>2.5	NO	0.780922	NO	YES
BDL-418/AAZ/IE PA3	12.201	127	33	66	>2.5	NO	1.535	NO	NO
BDL-418/AAZ/INTER	12.225	100	26	52	>2.5	NO	0.98886	NO	NO
BDL-421 PA38	12.221	58	20	43	>2.5	NO	0.741741	YES	YES
BDL-421 PA39	12.221	94	35	71	>2.5	NO	1.725729	NO	NO
BDL-423 PA47	14.35	64	19	40	>2.5	NO		YES	YES
BDL-423 PA48	14.35	78	31	37	>2.5	NO	0.171361	YES	YES
BDL-423 PA50	14.35	65	26	41	>2.5	NO	0.458703	YES	YES
BDL-423 PA52	14.35	137	30	40	>2.5	NO	0.305171	YES	YES
BDL-423 PA53	14.35	214	39	52	>2.5	NO	0.543977	NO	YES
BDL-423 PA54	14.35	49	11	42	>2.5	NO	0.938098	NO	YES
BDL-423 PA55	14.35	82	17	64	>2.5	NO	1.780972	NO	NO
BDL-423 PA56	14.35	56	11	37	>2.5	NO	0.717809	YES	YES
BDL-423 PA58	14.35	54	12	39	>2.5	NO	0.776738	YES	YES
BDL-423 PA59	14.35	92	18	58	>2.5	NO	1.566063	NO	NO
BDL-423 PA60	14.35	123	33	40	>2.5	NO	0.213866	YES	YES
BDL-423/TE/OE	14.35	167	50	60	>2.5	NO	0.466243	NO	YES
BDL-423/WS/1,4,7	14.35	148	34.8	55.68	2.5	NO	0.88947	NO	NO
BDL-423/WY/2,5,8	14.35	192	41	50	2.5	NO	0.36175	NO	YES
BDL-423/WY/2,5,8	14.35	192	41	50	2.5	NO	0.361741	NO	YES
BDL-423/WZ/1,4,7	14.35	95	13.05	44.37	2.5	NO	0.980054	NO	NO
BDL-427/KA/IE PA62	14.29	313	34	43	2.5	NO	0.324794	NO	YES
DME-147/4700/01	14.34	100	42.12	71.28	2.5	NO	1.417456	NO	NO
DME-148/4800/01	14.22	259	60.5	72	2.5	NO	0.469763	NO	YES
DME-149/4900/11	14.34	104	44	64	2.5	NO	0.965954	NO	NO
DME-170/7000/01	14.346	100	39	66	2.5	NO	1.286977	NO	NO
DME-172/7200/31	12.17	103	40	62	2.5	NO	1.060532	NO	NO
DME-177/7700/15	14.404	550	34.4	60.1	2.5	NO	1.264427	NO	NO
DME-180/8000/01	12.207	114	30.4	63.9	2.5	NO	1.473818	NO	NO
DME-180/8000/23	12.206	114	30.42	63.89	2.5	NO	1.472412	NO	NO
DME-180/8000/35	12.194	132	31.34	57.25	2.5	NO	1.101876	NO	NO
DME-185/8500/01	12.251	114	30.72	64.53	2.5	NO	1.495258	NO	NO
DME-185/8500/11	12.251	180	27.29	57.77	2.5	NO	1.292184	NO	NO
DME-185/8500/21	12.251	106	43.9	59.47	2.5	NO	0.744482	NO	YES
DME-197/9700 PA94	12.221	112	37	63	2.5	NO	1.238123	NO	NO
DME-197/9700/OE2	12.221	125	34	64	2.5	NO	1.408472	NO	NO

DME-197/9700/OE3	12.221	125	34	64	2.5	NO	1.408472	NO	NO
DME-197/9700/OE4	12.221	125	34	64	2.5	NO	1.408472	NO	NO
DME-206/E206/AH17	12.444	72.4	27.65	59.3	2.5	NO	1.32132	NO	NO
HB-LVRF/AKG/MIDDLE	10.777	176	28.6	45.4	2.5	NO	0.580063	NO	YES
NPD-40/KD (34)	13.716	480	35	47	2.5	NO	0.508917	NO	NO
NPD-40/KE (35)	14.38	472	51.8	69.5	2.5	NO	0.837376	NO	NO
NPD-40/KF (36)	13.716	495	31.3	51	2.5	NO	0.886291	NO	NO
NRU-129 PA100	14.34	65	38	65	2.5	NO	1.28975	NO	NO
NRU-129 PA97	14.34	93	51	64	2.5	NO	0.622742	YES	YES
NRU-129 PA98	14.34	95	41	55	2.5	NO	0.616365	YES	YES
NRU-129 PA99	14.34	65	38	59	2.5	NO	0.967681	YES	YES
NRU-129/2900/02	14.34	55	34	51	2.5	NO	0.621828	YES	YES
NRU-130/3000/03,07	14.417	68	25	60	2.5	NO	1.451024	NO	NO
NRU-130/3000/19	14.404	55	19	60	2.5	NO	1.665114	NO	NO
NRU-130/3000/22	14.403	108	40	56	2.5	NO	0.708557	NO	YES
NRU-130/3000/23	14.404	54	19	60	2.5	NO	1.665803	NO	NO
NRU-234/3400/01,04	14.31	131	35	64	2.5	NO	1.328426	NO	NO
PNGS-1/1988/OE/04	14.409	126.54	36.85217	56.38381	0.7	NO	0.788136	NO	NO
PNGS-1/1988/OE/05	14.409	127.65	36.68422	55.39318	0.7	NO	0.745144	NO	NO
PNGS-1/1988/OE/06	14.409	129.87	37.01913	58.86041	0.7	NO	0.908098	NO	NO
PNGS-1/1988/OE/07	14.409	133.2	39.1012	57.86977	0.7	NO	0.774717	NO	NO
PNGS-1/1988/OE/08	14.409	152.07	35.0851	44.90892	0.7	NO	0.333868	YES	YES
PNGS-1/1988/OE/09	14.409	163.17	33.12194	54.31999	0.7	NO	0.805043	NO	NO
PNGS-1/1988/OE/10	14.409	166.5	35.11337	51.26552	0.7	NO	0.603376	NO	YES
PNGS-1/1988/OE/11	14.409	167.61	34.43336	52.33871	0.7	NO	0.673316	NO	NO
PNGS-1/1988/OE/12	14.409	175.38	34.10039	52.1736	0.7	NO	0.677565	NO	NO
PNGS-1/1988/OE/13	14.409	176.49	35.283	51.51318	0.7	NO	0.610282	NO	NO
PNGS-1/1988/OE/14	14.409	182.04	34.45219	51.67828	0.7	NO	0.646493	NO	NO
PNGS-1/1988/OE/15	14.409	184.26	32.66674	53.24679	0.7	NO	0.775425	NO	NO
PNGS-1/1988/OE/16	14.409	188.7	33.18209	51.10041	0.7	NO	0.636517	NO	NO
PNGS-1/1988/OE/17	14.409	192.03	33.66121	43.42297	0.7	NO	0.324079	YES	YES
PNGS-1/1988/OE/18	14.409	194.25	31.50375	42.84509	0.7	NO	0.36648	YES	YES
PNGS-1/1988/OE/19	14.409	196.47	31.68585	43.09275	0.7	NO	0.370858	YES	YES
PNGS-1/1988/OE/20	14.409	198.69	34.02529	50.35743	0.7	NO	0.602598	NO	NO
PNGS-1/1988/OE/21	14.409	200.91	42.15326	47.63318	0.7	NO	0.194224	YES	YES
PNGS-1/1988/OE/23	14.409	205.35	33.24744	48.54126	0.7	NO	0.546294	NO	YES
PNGS-1/1988/OE/25	14.409	217.56	33.78163	51.34807	0.7	NO	0.662555	NO	NO
PNGS-1/1988/OE/28	14.409	224.22	32.49433	45.81701	0.7	NO	0.45899	NO	YES

PNGS-1/1988/OE/29	14.409	226.44	40.69726	46.39488	0.7	NO	0.198697	YES	YES
PNGS-1/1988/OE/31	14.409	241.98	42.20979	48.54126	0.7	NO	1.786247	YES	NO
PNGS-1/1988/OE/32	14.409	77.7	37.96457	63.40083	0.7	NO	1.117294	NO	NO
PNGS-1/1988/OE/33	14.409	81.03	36.73616	58.77786	0.7	NO	0.927213	YES	YES
PNGS-1/1988/OE/35	14.409	96.57	38.47385	62.32764	0.7	NO	1.03262	NO	NO
PNGS-1/1988/OE/36	14.409	102.12	38.27979	55.8885	0.7	NO	0.711176	YES	YES
PNGS-1/1988/OE/37	14.409	112.11	35.40074	60.18126	0.7	NO	2.736297	NO	NO
PNGS-1/1988/OE/38	14.409	123.21	35.73948	58.61275	0.7	NO	0.946677	NO	NO
PNGS-1/1988/OE/39	14.409	126.54	37.11789	49.36679	0.7	NO	0.446301	YES	YES
PNGS-1/1988/OE/40	14.409	127.65	37.07005	58.19998	0.7	NO	0.872635	NO	NO
PNGS-1/1988/OE/41	14.409	128.76	35.02613	49.03658	0.7	NO	0.500887	YES	YES
PNGS-1/1988/OE/43	14.409	133.2	46.44513	53.4119	0.7	NO	0.270046	YES	YES
PNGS-1/1988/OE/44	14.409	135.42	37.31403	55.97105	0.7	NO	0.74928	NO	NO
PNGS-1/1988/OE/45	14.409	139.86	35.55112	44.08339	0.7	NO	0.288736	YES	YES
PNGS-1/1988/OE/46	14.409	143.19	37.81923	44.2485	0.7	NO	0.218248	YES	YES
PNGS-1/1988/OE/48	14.409	153.18	36.70546	44.4136	0.7	NO	0.261475	YES	YES
PNGS-1/1988/OE/49	14.409	164.28	43.50193	50.02722	0.7	NO	0.239527	YES	YES
PNGS-1/1988/OE/50	14.409	172.05	33.54708	52.66892	0.7	NO	0.715477	NO	NO
PNGS-1/1988/OE/51	14.409	175.38	36.08093	51.59573	0.7	NO	0.584961	NO	YES
PNGS-1/1988/OE/52	14.409	179.82	35.09914	51.59573	0.7	NO	0.621134	NO	NO
PNGS-1/1988/OE/54	14.409	182.04	34.58308	51.18296	0.7	NO	0.619379	NO	NO
PNGS-1/1988/OE/55	14.409	184.26	32.96902	52.09105	0.7	NO	0.709984	NO	NO
PNGS-1/1988/OE/56	14.409	192.03	34.11469	51.51318	0.7	NO	0.629204	NO	NO
PNGS-1/1988/OE/57	14.409	194.25	34.72737	52.09105	0.7	NO	0.66041	NO	NO
PNGS-1/1988/OE/60	14.409	203.13	43.56973	47.05531	0.7	NO	0.122661	YES	YES
PNGS-1/1988/OE/61	14.409	205.35	33.88721	48.45871	0.7	NO	0.52326	NO	YES
PNGS-1/1988/OE/64	14.409	215.34	43.41158	50.35743	0.7	NO	0.259104	YES	YES
PNGS-1/1988/OE/65	14.409	224.22	32.6085	45.6519	0.7	NO	0.448716	NO	YES
PNGS-1/1988/OE/67	14.409	81.03	38.83056	62.90551	0.7	NO	1.05482	NO	NO
PNGS-1/1988/OE/68	14.409	119.88	35.22269	58.11743	0.7	NO	0.929345	NO	NO
PNGS-1/1988/OE/69	14.409	123.21	37.74635	57.37445	0.7	NO	0.80374	NO	NO
PNGS-1/1988/OE/70	14.409	124.32	35.23251	59.19062	0.7	NO	0.985072	NO	NO
PNGS-1/1988/OE/71	14.409	127.65	38.10567	57.53956	0.7	NO	0.797533	NO	NO
PNGS-1/1988/OE/72	14.409	128.76	36.35515	56.71403	0.7	NO	0.824545	NO	NO
PNGS-1/1988/OE/78	14.409	173.16	33.27925	53.24679	0.7	NO	0.751871	NO	NO
PNGS-1/1988/OE/79	14.409	182.04	32.34861	43.67063	0.7	NO	0.370257	YES	YES
PNGS-1/1988/OE/81	14.409	184.26	35.44591	50.68765	0.7	NO	0.56722	NO	YES
PNGS-1/1988/OE/83	14.409	192.03	40.29714	47.55063	0.7	NO	0.255706	YES	YES

PNGS-1/1988/OE/84	14.409	196.47	33.60172	43.0102	0.7	NO	0.311132	YES	YES
PNGS-1/1988/OE/85	14.409	198.69	31.79826	42.92765	0.7	NO	0.356594	YES	YES
PNGS-1/1988/OE/86	14.409	199.8	34.18477	50.93531	0.7	NO	0.62484	NO	NO
PNGS-1/1988/OE/88	14.409	202.02	34.47467	48.95403	0.7	NO	0.525319	NO	YES
PNGS-1/1988/OE/92	14.409	210.9	41.41533	49.28424	0.7	NO	0.287305	YES	YES
PNGS-1/1988/OE/96	14.409	243.09	41.84592	48.54126	0.7	NO	0.237488	YES	YES
PNGS-1/1988/OE/97	14.409	53.28	39.1712	58.36509	0.7	NO	0.781496	YES	YES
PNGS-1/1988/OE/98	14.409	56.61	38.14712	58.36509	0.7	NO	0.855778	YES	YES
PNGS-1/1988/OE/99	14.409	67.71	38.14354	63.31828	0.7	NO	1.110384	YES	NO
PNGS-1/1988/OE/100	14.409	72.15	36.41184	61.1719	0.7	NO	1.053332	YES	NO
PNGS-1/1988/OE/102	14.409	89.91	35.98725	60.09871	0.7	NO	1.011844	NO	NO
PNGS-1/1988/OE/103	14.409	92.13	35.58146	56.21871	0.7	NO	0.819076	YES	YES
PNGS-1/1988/OE/104	14.409	97.68	39.13235	60.26381	0.7	NO	0.901323	NO	NO
PNGS-1/1988/OE/105	14.409	101.01	37.06904	57.45701	0.7	NO	0.838958	NO	NO
PNGS-1/1988/OE/106	14.409	122.1	35.55683	49.77956	0.7	NO	0.518313	YES	YES
PNGS-1/1988/OE/107	14.409	128.76	45.1244	53.24679	0.7	NO	0.314932	YES	YES
PNGS-1/1988/OE/108	14.409	129.87	36.46098	56.87913	0.7	NO	0.828553	NO	NO
PNGS-1/1988/OE/109	14.409	133.2	35.0851	58.94296	0.7	NO	0.977682	NO	NO
PNGS-1/1988/OE/110	14.409	144.3	37.03934	41.85446	0.7	NO	0.160025	YES	YES
PNGS-1/1988/OE/111	14.409	152.07	33.26587	44.90892	0.7	NO	0.385373	YES	YES
PNGS-1/1988/OE/112	14.409	166.5	34.24625	53.08169	0.7	NO	0.713436	NO	NO
PNGS-1/1988/OE/113	14.409	167.61	33.38934	52.42126	0.7	NO	0.706558	NO	NO
PNGS-1/1988/OE/114	14.409	174.27	34.87342	54.40254	0.7	NO	0.764483	NO	NO
PNGS-1/1988/OE/116	14.409	182.04	32.49878	51.34807	0.7	NO	0.689173	NO	NO
PNGS-1/1988/OE/117	14.409	183.15	35.15726	50.27488	0.7	NO	0.558595	NO	YES
PNGS-1/1988/OE/118	14.409	184.26	36.49089	50.35743	0.7	NO	0.513795	NO	YES
PNGS-1/1988/OE/119	14.409	187.59	33.17801	52.42126	0.7	NO	0.720627	NO	NO
PNGS-1/1988/OE/120	14.409	190.92	36.67036	50.60509	0.7	NO	0.519184	NO	YES
PNGS-1/1988/OE/121	14.409	193.14	34.57996	49.44935	0.7	NO	0.005228	NO	YES
PNGS-1/1988/OE/122	14.409	196.47	36.06578	50.85275	0.7	NO	0.553624	NO	YES
PNGS-1/1988/OE/124	14.409	199.8	42.13801	48.45871	0.7	NO	0.227181	YES	YES
PNGS-1/1988/OE/125	14.409	200.91	35.09953	50.19233	0.7	NO	0.558882	NO	YES
PNGS-1/1988/OE/130	14.409	218.67	34.32474	45.6519	0.7	NO	0.392578	YES	YES
PNGS-1/1988/OE/131	14.409	225.33	45.2149	49.28424	0.7	NO	0.14923	YES	YES
PNGS-1/1988/OE/132	14.409	228.66	32.89126	41.7719	0.7	NO	0.291722	YES	YES
PNGS-1/1988/OE/133	14.409	251.97	39.75587	45.32169	0.7	NO	0.191991	YES	YES
BDL-415/AAA/INTE	12.223	96	26	60	2.5	YES	1.4239	YES	YES
BDL-415/AAB/INTE	12.223	106	27	61	2.5	YES	1.442744	YES	YES

BDL-416/AAV/07	12.23	80.8	30.67	63.97	2.5	YES	1.458075	YES	YES
BDL-416/AAV/18	12.233	80.8	30.67	63.97	2.5	YES	1.458063	YES	YES
BNGS/J64728C/OE	12.239	196.71	11.52	44.61	2.5	YES	1.09041	YES	YES
BNGS/J79473C/OE	12.22	127.14	49.01	59.66	2.5	YES	0.499134	NO	NO
BNGS/J85181C/OE	12.22	128.06	49.17	59.91	2.5	YES	0.5033	NO	NO
DME-148/4800/03	14.22	121	41	65	2.5	YES	1.016157	YES	YES
DME-150/5000/05	14.36	104	42	66	2.5	YES	1.157658	YES	YES
DME-150/5000/20	14.36	121	41	65	2.5	YES	1.145297	YES	YES
DME-151/5100/07	14.37	121	40.71	64.69	2.5	YES	1.141244	YES	YES
DME-152/5200/07	14.37	121	40.89	64.97	2.5	YES	1.148663	YES	YES
DME-166 PA74	14.389	107	35	70	2.5	YES	1.629461	YES	YES
DME-172/7200/14	12.17	91	37	61	2.5	YES	1.13808	YES	YES
DME-178/7800/06	12.221	132	36	58	2.5	YES	1.011708	YES	YES
DME-178/7800/12	12.221	338	28.2	61	2.5	YES	1.542821	YES	YES
DME-180/8000/29	12.199	180	26.97	57.15	2.5	YES	1.270506	YES	YES
DME-187/8700/01	12.213	129	30.06	61.14	2.5	YES	1.345858	YES	YES
FFO 104	12.150	240	30	58	0.3	YES	1.115717	YES	YES
PNGS-1/1988/OE/22	14.409	203.13	35.01937	54.98041	0.7	YES	0.794693	YES	YES
PNGS-1/1988/OE/24	14.409	210.9	34.99647	57.04424	0.7	YES	0.901821	YES	YES
PNGS-1/1988/OE/26	14.409	218.67	36.38033	52.75147	0.7	YES	0.63524	YES	YES
PNGS-1/1988/OE/27	14.409	220.89	32.67933	55.22807	0.7	YES	0.892562	YES	YES
PNGS-1/1988/OE/30	14.409	230.88	34.45219	51.67828	0.7	YES	0.658012	YES	YES
PNGS-1/1988/OE/34	14.409	88.8	36.06787	60.59403	0.7	YES	1.037653	YES	YES
PNGS-1/1988/OE/42	14.409	129.87	37.51467	59.27318	0.7	YES	0.910076	YES	YES
PNGS-1/1988/OE/47	14.409	147.63	34.46595	55.14552	0.7	YES	0.804316	YES	YES
PNGS-1/1988/OE/53	14.409	180.93	34.89748	53.74211	0.7	YES	0.732718	YES	YES
PNGS-1/1988/OE/58	14.409	196.47	33.02127	55.80594	0.7	YES	0.901138	YES	YES
PNGS-1/1988/OE/59	14.409	197.58	34.35277	53.24679	0.7	YES	0.729786	YES	YES
PNGS-1/1988/OE/62	14.409	207.57	32.72643	54.98041	0.7	YES	0.870737	YES	YES
PNGS-1/1988/OE/63	14.409	210.9	35.70015	53.90722	0.7	YES	0.7013	YES	YES
PNGS-1/1988/OE/66	14.409	227.55	32.70578	51.34807	0.7	YES	0.742187	YES	YES
PNGS-1/1988/OE/73	14.409	129.87	35.07288	59.27318	0.7	YES	0.994225	YES	YES
PNGS-1/1988/OE/74	14.409	130.98	37.32619	60.84169	0.7	YES	0.998583	YES	YES
PNGS-1/1988/OE/75	14.409	133.2	34.93768	58.6953	0.7	YES	0.969212	YES	YES
PNGS-1/1988/OE/76	14.409	135.42	39.11312	56.71403	0.7	YES	0.715547	YES	YES
PNGS-1/1988/OE/77	14.409	165.39	33.805	53.4119	0.7	YES	0.741477	YES	YES
PNGS-1/1988/OE/80	14.409	183.15	32.71739	53.32935	0.7	YES	0.777452	YES	YES
PNGS-1/1988/OE/82	14.409	186.48	34.84313	50.52254	0.7	YES	0.5814	YES	YES

PNGS-1/1988/OE/87	14.409	200.91	33.32146	54.98041	0.7	YES	0.849178	YES	YES
PNGS-1/1988/OE/89	14.409	204.24	34.21481	56.79658	0.7	YES	0.916348	YES	YES
PNGS-1/1988/OE/90	14.409	206.46	35.5908	53.74211	0.7	YES	0.711343	YES	YES
PNGS-1/1988/OE/91	14.409	208.68	34.15637	54.6502	0.7	YES	0.809383	YES	YES
PNGS-1/1988/OE/93	14.409	219.78	32.57637	54.40254	0.7	YES	0.853083	YES	YES
PNGS-1/1988/OE/94	14.409	223.11	33.76691	52.33871	0.7	YES	0.712826	YES	YES
PNGS-1/1988/OE/95	14.409	227.55	33.72172	55.64084	0.7	YES	0.882388	YES	YES
PNGS-1/1988/OE/101	14.409	78.81	39.73204	61.58466	0.7	YES	0.949818	NO	YES
PNGS-1/1988/OE/115	14.409	176.49	34.90503	52.0085	0.7	YES	0.646778	YES	YES
PNGS-1/1988/OE/123	14.409	198.69	33.46884	55.55828	0.7	YES	0.872978	YES	YES
PNGS-1/1988/OE/126	14.409	203.13	34.12548	53.57701	0.7	YES	0.755548	YES	YES
PNGS-1/1988/OE/127	14.409	206.46	36.34556	54.15488	0.7	YES	0.703003	YES	YES
PNGS-1/1988/OE/128	14.409	214.23	34.84998	55.06296	0.7	YES	0.806919	YES	YES
PNGS-1/1988/OE/129	14.409	217.56	33.02127	53.82467	0.7	YES	0.808552	YES	YES
R-r/DME+#146/4600/01	14.16	100	39	66	2.5	YES	1.286723	YES	YES

Prediction accuracy calculations

FUELOGRAMS-based Correlations

Non-CANLUB

# Correct Predictions of Failed vs. Intact	Total # power histories	% Correctly Predicted
53	65	80%

CANLUB

# Correct Predictions of Failed vs. Intact	Total # power histories	% Correctly Predicted
120	237	51%

Total

# Correct Predictions of Failed vs. Intact	Total # power histories	% Correctly Predicted
173	303	57%

Delta Strain Threshold

Non-CANLUB

# Correct Predictions of Failed vs. Intact	Total # power histories	% Correctly Predicted
50	65	76%

CANLUB

# Correct Predictions of Failed vs. Intact	Total # power histories	% Correctly Predicted
141	237	60%

Total

# Correct Predictions of Failed vs. Intact	Total # power histories	% Correctly Predicted
191	302	63%

APPENDIX C: INPUT FILE

Table 31 shows the input file for the reference case for test FIO-104. COMSOL reads input files in text file format with spaces separating the entries on each line. Model parameters which are not changed between studies may be omitted from the input file; they will be assigned the default value coded into the model. Multiple cases may be defined in an input file by listing multiple values in each row, separated by a space.

Table 31: Sample input file

case_index_number	5000
linear_power_parm	-101
coolant_temperature_parm	566[K]
coolant_pressure_parm	8.50e6[Pa]
sheath_thickness	0.43[mm]
fg_release_damping_constant	300[s]
contact_penalty_factor	1e13[Pa/m]
contact_pressure_est	15[MPa]
axial_contact_penalty_factor	1e14[Pa/m]
axial_contact_pressure_est	100[MPa]
cracked_model_flag	1
max_time_step	36*3600
solver_initial_damping_factor	0.25
solver_damping_growth_rate	2
periodic_bc_flag	1
fg_Pext_param	-2
pellet_axial_constraint_location_flag	1
sheath_inner_diameter	12.105[mm]
ramp_burnup	278
initial_power	30
ramped_power	58
dwell_time	1.0[h]
CANLUB_thickness	5[um]
ramping_time	10[s]
time1	3.38E7[s]
timestep_at_ramp	5[s]
comp_3_domain	element_length/2
crack_radius	0.5[um]

APPENDIX D: MATERIAL PARAMETERS

Yield Strength of Zircaloy-4

The yield strength of Zircaloy-4 as a function of temperature is input in the model in tabular form from MATPRO [32], shown in Figure 30. A linear interpolation is made between data points.

Table 32: Yield Strength of Zircaloy-4

Temperature (°C)	Yield Strength (MPa)
290	655.4
400	525.1
500	450.5
600	388.8
700	321.8

Geometric Factors

The geometric factor F for the calculation of the stress intensity factor, as detailed in 5.5.2, is determined through a weight function method. The weighting terms G_0, G_1, G_2, G_3 represent uniform tension, linear, quadratic and cubic loading conditions along the crack face. The values of the weighting function and Q for a given crack can be obtained by comparison against numerical reference solutions [67]. The calculation of all of these parameters can be cumbersome, therefore tables for the value of F based on (a/c), (a/R_{in}) and (R_{in}/t) are given in [41]. The geometric definitions of these parameters are illustrated in Figure 34. For a 28 element fuel bundle the element R_{in}/t = 7.2mm/0.38mm ≈ 20, while for a 37 element fuel bundle R_{in}/t = 6.105mm/0.38mm ≈ 15. Tabulated values of F for R_{in}/t = 20 and R_{in}/t = 15 for the three a/c values investigated in 8.2.5 are provided in Table 33 and Table 34. A linear interpolation is made between data points in the tables.

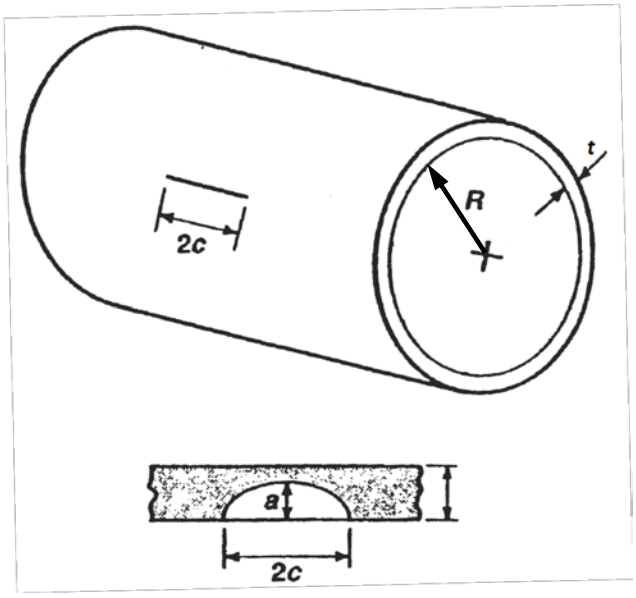

Figure 34: Illustration of the geometric parameters of the crack and body [41]

Table 33: Geometric factors for $R_{in}/t = 20$

a/t	a/c 0.2	a/c 0.6	a/c 1.0
0	0.972	0.833	0.684
0.08	1.05	0.86	0.692
0.2	1.167	0.901	0.704
0.3	1.278	0.935	0.714
0.4	1.39	0.969	0.725
0.5	1.501	1.003	0.735
0.6	1.631	1.037	0.745
0.7	1.762	1.071	0.755
0.8	1.893	1.105	0.766
0.9	2.033	1.138	0.775
1	2.175	1.171	0.785

Table 34: Geometric factors for $R_{in}/t = 15$

a/t	a/c 0.2	a/c 0.6	a/c 1.0
0	1.020	0.864	0.707
0.08	1.093	0.891	0.716
0.2	1.202	0.931	0.730
0.3	1.320	0.968	0.742
0.4	1.438	1.005	0.755
0.5	1.556	1.042	0.767
0.6	1.709	1.083	0.780
0.7	1.863	1.124	0.793
0.8	2.019	1.166	0.808
0.9	2.197	1.210	0.821
1	2.378	1.253	0.835

APPENDIX E: COMSOL MODEL REPORT

The following report is generated by COMSOL to describe the model setup. Due to the length of the report, component 1 has been removed; all of the model development in this thesis is implemented in components 2 and 3.

GLOBAL DEFINITIONS

PARAMETERS

Name	Expression
pellet_radius	sheath_inner_diameter/2
radial_chamfer	0.43[mm] + 0.08[mm]*bundle_type
axial_chamfer	radial_chamfer*tan(0.175)
land_width	0.0[mm]
dish_depth	0.584[mm] - 0.284[mm]*bundle_type
pellet_length	22.99[mm] - 6.99[mm]*bundle_type
pellet_sheath_gap	0.05[mm]/2
pellet_pellet_gap	(2.29[mm] + 1.27[mm]*bundle_type)/num_pellets
pellet_hole_radius	0[mm]
pellet_hole_free_vol_fraction	0
v0_ends	0.864[cm^3]
v0_total	(v0_gap + v0_disk + v0_chamfer*num_chamfers + v0_dish*num_dishes)*num_pellets + v0_ends
sheath_thickness	0.38[mm]
mf0_He	1
mf0_Ne	0
mf0_Ar	0
mf0_Kr	0
mf0_Xe	0
mf0_N2	0
mf0_O2	0
linear_power_parm	55[kW/m]
coolant_pressure_parm	9.98e6[Pa]
coolant_temperature_parm	557[K]
sheath_coolant_ht_coef_parm	50[kW/m^2/K]
gas_pressure_forced_parm	0

T_ends_parm	-140[K]
t_max	timestep_range4_end
burnup_max	burnup3
UO2_pore_fraction_initial	1 - 10.60/10.98
UO2_roughness	1[um]
Zir_roughness	0.5[um]
s_dev	0
U235_percent	0.71
num_pellets	21 + 9*bundle_type
UO2_grain_diameter_int	9[um]
dish_radius	(dish_depth^2 + (pellet_radius - land_width - radial_chamfer)^2)/(2*dish_depth)
sheath_internal_radius	pellet_radius + pellet_sheath_gap
RMS_surf_roughness	sqrt((UO2_roughness^2 + Zir_roughness^2)/2)
v0_gap	pi*(pellet_length + pellet_pellet_gap)*(sheath_internal_radius^2 - pellet_radius^2)
v0_chamfer	axial_chamfer*pi*radial_chamfer*(pellet_radius - axial_chamfer/3)
v0_disk	pi*pellet_pellet_gap*pellet_radius^2
v0_dish	pi*(dish_depth - dish_radius)*((pellet_radius - radial_chamfer - land_width)^2 - pellet_hole_radius^2) - 2*pi/3*((dish_radius^2 - (pellet_radius - radial_chamfer - land_width)^2)^(3/2) - (dish_radius^2 - (pellet_hole_radius)^2)^(3/2))
v0_pellet_hole	pi*pellet_hole_radius^2*pellet_length*pellet_hole_free_vol_fraction
v0_pellet	v0_gap + v0_chamfer*num_chamfers + v0_disk + v0_dish*num_dishes + v0_pellet_hole
P0_fill	1[atm]
T0_fill	293.15[K]
m0_gas_element	P0_fill*v0_total/8.314[J/mol/K]/T0_fill
T_geom_ref	293.15[K]
energy_per_fission	200[MeV]
rho_UO2_theory	10980[kg/m^3]
pellet_solid_volume	(pi*(pellet_radius^2 - pellet_hole_radius^2)*pellet_length - num_dishes*v0_dish - num_dishes*v0_chamfer)
mass_UO2_pellet	rho_UO2_theory*(1 - UO2_pore_fraction_initial)*(pi*(pellet_radius^2 - pellet_hole_radius^2)*pellet_length - num_dishes*v0_dish - num_dishes*v0_chamfer)
mass_U_pellet	mass_UO2_pellet*238/(238 + (2 + s_dev)*16)
sheath_length_initial	(pellet_length + pellet_pellet_gap)*num_pellets_model
missing_vol_ratio	(v0_disk + v0_dish*num_dishes + v0_chamfer*num_chamfers + v0_pellet_hole*pellet_hole_free_vol_fraction)/v0_pellet_cylinder

v0_pellet_cylinder	pi*(pellet_radius^2 - pellet_hole_radius^2*pellet_hole_free_vol_fraction)*(pellet_length + pellet_pellet_gap)
num_neutron_per_fission	2.42
num_dishes	2
num_chamfers	2
mesh_nodes_pellet_dish	11
mesh_nodes_pellet_chamfer	2
mesh_nodes_pellet_axial	30
mesh_nodes_sheath_radial	4
mesh_nodes_sheath_axial	44
timestep_range1_start	0.5[s]
timestep_range1_size	0.5[s]
timestep_range1_end	15[s]
timestep_range2_start	time1 - 20[s]
timestep_range2_size	timestep_at_ramp
timestep_range2_end	time1 + 2*ramping_time
timestep_range3_start	timestep_range2_end
timestep_range3_size	timestep_at_ramp*2
timestep_range3_end	timestep_range3_start + 4*ramping_time
timestep_range4_start	timestep_range3_end
timestep_range4_size	timestep_at_ramp*6
timestep_range4_end	time1 + dwell_time
max_time_step	2*24*3600
solver_initial_damping_factor	1/2^3
solver_damping_growth_rate	2
fg_release_damping_constant	12*3600[s]
contact_penalty_factor	1e13[Pa/m]
contact_pressure_est	15[MPa]
contact_error_tol	1e7[Pa]
peripheral_tc_location	7.35[mm]
peripheral_tc_raidius	0.65[mm]
cracked_model_flag	1
gas_pressure_set_time	9e99[s]
gas_pressure_set_value	1[Pa]
case_index_number	0
UO2_add_TC	0
UO2_mul_Texp	1

UO2_mul_FGDiff	1
UO2_mul_FGGBSat	1
Zir_add_TC	0
Zir_add_YoungsM	0
Zir_mul_Texp	1
num_pellets_model	1
axial_contact_pressure_est	100[MPa]
axial_contact_penalty_factor	1e14[Pa/m]
axial_contact_offset_dist	1e-5[m]
pellet_pellet_gap_model	pellet_pellet_gap/10*0
periodic_bc_flag	1
fg_Pext_param	0
pellet_axial_constraint_location_flag	0
thermal_to_fission_power_ratio	0.925
burnup_avg_flag	1
transient_start	387972[s]
burnup1	ramp_burnup
burnup2	ramp_burnup + dwell_time*ramped_power*burnup_to_time_conversion
burnup3	burnup2
linear_power1	initial_power
linear_power2	ramped_power
linear_power3	linear_power2
Yield_I127	1.24657e-3
lambda_I127	0[s^ - 1]
Yield_I129	7.17849e-3
lambda_I129	1.399e-15[s^ - 1]
Yield_I131	2.88e-2
lambda_I131	1.000229e-6[s^ - 1]
Yield_I132	4.30e-2
lambda_I132	8.38958e-5[s^ - 1]
Yield_I133	6.70e-2
lambda_I133	9.25677e-6[s^ - 1]
Yield_I134	7.71e-2
lambda_I134	2.20e-4[s^ - 1]
Yield_I135	6.30e-2
lambda_I135	2.93061e-5[s^ - 1]

fission_fragment_range	7.67e-6[m]
particles_per_fission	2
CsI_decomp_energy	0.230[eV^ - 1]
recoil_energy_loss	463.5e8[eV/cm]
mol_mass_CsI	259.8[g/mol]
rho_CsI	4.5[g/cm^3]
N_avogadro	6.022e23[mol^ - 1]
Tg	640
M_He	4.003
M_I2	253.8
p	10
sigma_AB	3.78
omega_AB	1
M_Zr	91.2[g/mol]
rho_Zr	6.5[g/cm^3]
element_length	0.477[m]
rho_CANLUB	0.9[g/cm^3]
CANLUB_Na_content	137e-6[g/g]
M_Na	22.9898[g/mol]
CANLUB_thickness	5[um]
CANLUB_mass	2*pi*pellet_radius*element_length*CANLUB_thickness*rho_CANLUB
Na_content	CANLUB_mass*CANLUB_Na_content*N_avogadro/M_Na
Na_conc	Na_content/element_length/(2*pi*pellet_radius)
crack_radius	0.5[um]
bundle_type	if(sheath_inner_diameter<=13.2[mm], 1, 0)
Yield_Xe133	0.067
lambda_Xe133	1.52e-6[s^ - 1]
Xe133_R_B	7.06E-4
Yield_Kr85m	0.013
lambda_Kr85m	4.31E-5[s^ - 1]
Kr85m_R_B	5.37E-5
Yield_Kr88	0.0355
lambda_Kr88	6.86e-5[s^ - 1]
Kr88_R_B	8.82E-5
Yield_Kr87	0.0252
lambda_Kr87	1.52e-4[s^ - 1]
Kr87_R_B	2.90E-5

Yield_Xe135m	0.011
lambda_Xe135m	7.55e-4[s^ - 1]
Xe135m_R_B	1.80E-5
Yield_Xe138	0.0642
lambda_Xe138	8.14e-4[s^ - 1]
Xe138_R_B	1.36E-5
burnup_to_time_factor	1.8942E-7 + 0.7062E-7*bundle_type
t_ramp_starts	burnup1/(burnup_to_time_factor*initial_power)
t_ramp_ends	t_ramp_starts + dwell_time
sheath_inner_diameter	14.409[mm]
ramp_burnup	278
initial_power	30
ramped_power	58
dwell_time	0.7[h]
burnup_to_time_conversion	(7.39827 + 0.7062*bundle_type)*10^ - 6[s^ - 1]
time1	1[s]*ramp_burnup/(linear_power1*(2.7984386E-2*pellet_radius^2[m^ - 2] - 4.3727734E-4*pellet_radius[m^ - 1] + 1.9003858E-6))
time2	time1 + ramping_time+1e-6[s]
time3	time2 + dwell_time
ramping_time	0.001[s]
K_scc	1.5e6
strain_threshold	9e9
stress_threshold	300e6[Pa]
fuel_surface_area	2*pi*pellet_radius*element_length
timestep_at_ramp	5[s]
crack_length_initial	0[m]
K1c_zircaloy	50e6
sheath_hydrogen_content	101
comp_3_domain	element_length/2
radiolysis_multiplier	1.0
absorption	0[s^ - 1]
reaction	1
TG_growth_mod	1
fg_multi_mod	1
time_before_ramp	10
threshold	(CANLUB_thickness==0)*(5.65E-4 + 0.579/ramp_burnup) + (CANLUB_thickness>=0)*(ramp_burnup<=250)*((3.337E-3 + 0.419/ramp_burnup) + 0.0001) + (ramp_burnup>=500)*(5.65E-4 +

	0.579/ramp_burnup) + (ramp_burnup>250)*(ramp_burnup<500)*(((2 - ramp_burnup/250)*(0.003337 + 0.419/ramp_burnup + 0.0001)) + (((ramp_burnup/250) - 1)*(0.000565 + 0.573/ramp_burnup)))
n_cracks	1
F	1

FUNCTIONS

Function name	K1c
Function type	Piecewise

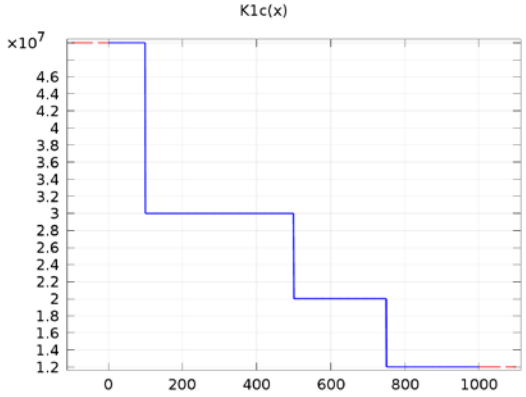

Definition	
Name	**Value**
Intervals	{{0, 100, 50e6}, {100, 500, 30E6}, {500, 750, 20E6}, {750, 1000, 12e6}}

Function name	zirc_yield
Function type	Interpolation

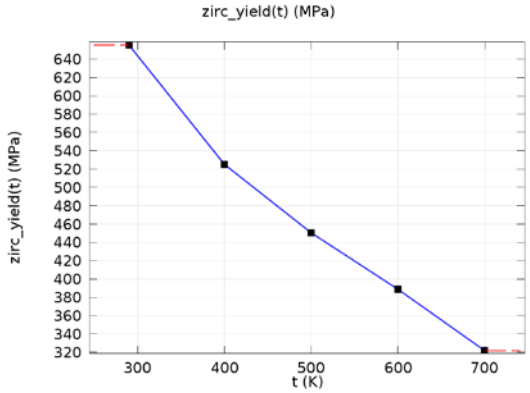

Function name	geo_factor_Rt_20_ac_1
Function type	Interpolation

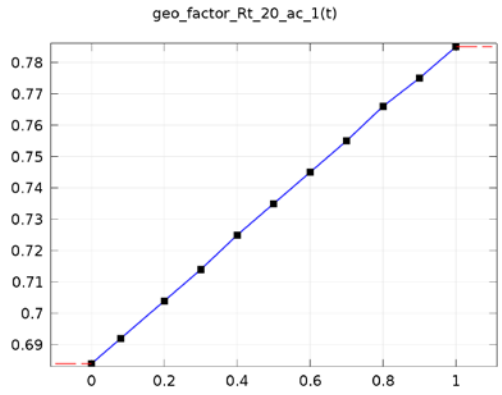

Interpolation 17

1.2.4. Interpolation 20

Function name	geo_factor_Rt_20_ac_06
Function type	Interpolation

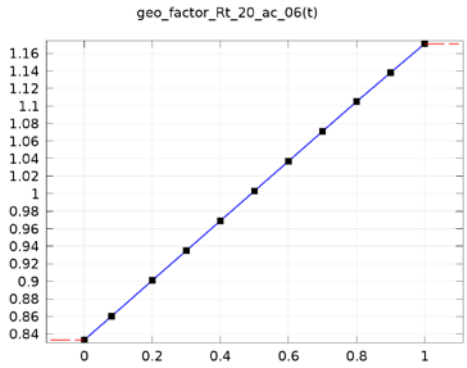

Interpolation 20

1.2.5. Interpolation 19

Function name	geo_factor_Rt_20_ac_02
Function type	Interpolation

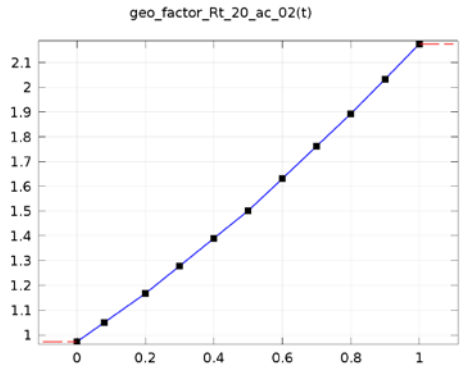

Interpolation 19

1.2.6. Interpolation 21

Function name	geo_factor_Rt_15_ac_1
Function type	Interpolation

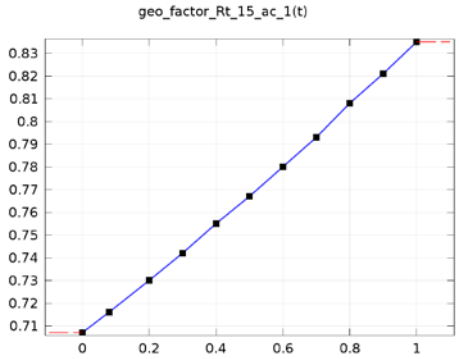

Interpolation 21

1.2.7. Interpolation 22

Function name	geo_factor_Rt_15_ac_06
Function type	Interpolation

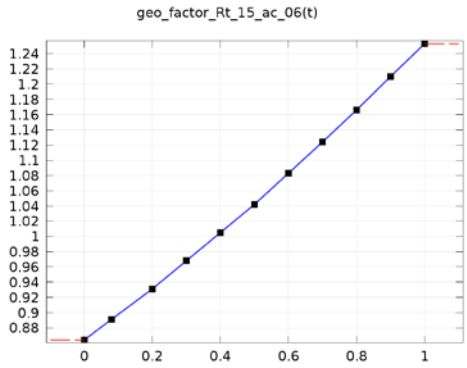

Interpolation 22

1.2.8. Interpolation 23

Function name	geo_factor_Rt_15_ac_02
Function type	Interpolation

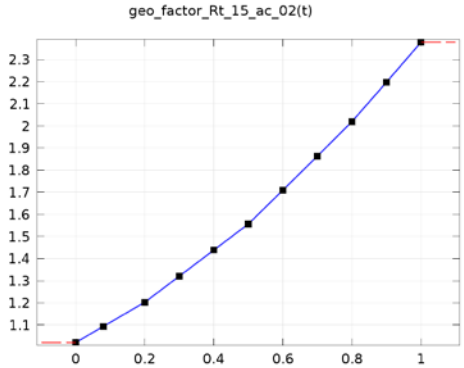

Interpolation 23

COMPONENT 2

VARIABLES

SCC GRAIN BOUNDARY VARIABLES

Selection	
Geometric entity level	Boundary
Selection	Boundary 3

Name	Expression
I127_release_at_gb	-3[m]*nojac(comp1.pellet_mid(fg_diff_coeff/(UO2_grain_radius)^2) *(I127_grain_concy))
I129_release_at_gb	-3[m]*nojac(comp1.pellet_mid(fg_diff_coeff/(UO2_grain_radius)^2) *(I129_grain_concy))
I131_release_at_gb	-3[m]*nojac(comp1.pellet_mid(fg_diff_coeff/(UO2_grain_radius)^2) *(I131_grain_concy))
I133_release_at_gb	-3[m]*nojac(comp1.pellet_mid(fg_diff_coeff/(UO2_grain_radius)^2) *(I133_grain_concy))
A1	1.0 + if(comp1.burnup_avg>40.8, (comp1.burnup_avg - 40.8)/(72.4 - 40.8)*2.82, 0)*if(comp1.burnup_avg>=72.4, 0, 1) + if(comp1.burnup_avg>=72.4, 2.82, 0)
fg_release_multiplier	A1[m]*exp(-10.0754 - 0.05*comp1.linear_power[m/kW] + 0.0012*comp1.linear_power^2[m^2/kW^2])*fg_multi_mod

SURFACE GRAIN BOUNDARY VARIABLES

Selection	
Geometric entity level	Point
Selection	Point 4

Name	Expression
sum_I	max(0, fg_surface_grain_boundary(I127_surf + I129_surf + I131_surf + I133_surf) - Na_conc - (I_released/(2*pi*pellet_radius*element_length)))
CsI_surface_thickness	mol_mass_CsI/rho_CsI/N_avogadro*fg_surface_grain_boundary(sum_I)
recoil_rate	0.25*fission_fragment_range*(2*pi*pellet_radius)*element_length*comp1.pellet_mid_avg(fission_rate_density)*particles_per_fission
I_net_release_rate	CsI_surface_thickness*recoil_energy_loss*CsI_decomp_energy*recoil_rate*radiolysis_multiplier*comp3.crack_initiation_flag

COMPONENT COUPLINGS

Coupling type	Maximum
Operator name	fg_surface_grain_boundary

Source selection	
Geometric entity level	Point
Selection	Point 4

GEOMETRY 2

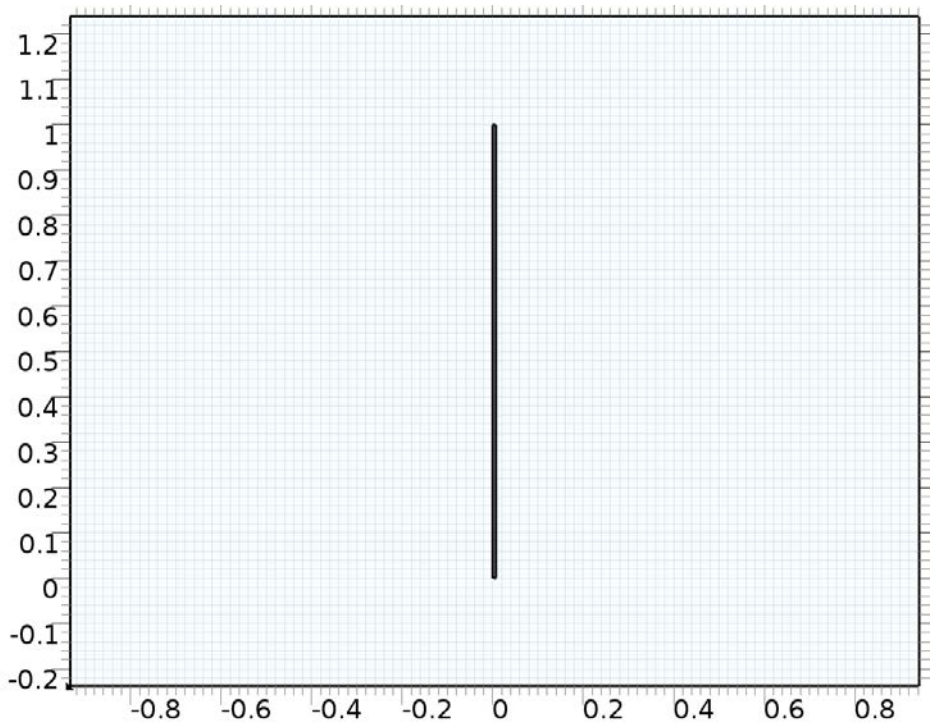

Units	
Length unit	m
Angular unit	deg

Geometry statistics	
Property	**Value**
Space dimension	2
Number of domains	1
Number of boundaries	4
Number of vertices	4

FISSION GAS GRAIN BOUNDARY (C)

COEFFICIENT FORM PDE 1

Settings	
Description	**Value**
Diffusion coefficient	{{0, 0}, {0, (y[1/m])^2*nojac(comp1.pellet_mid(fg_diff_coeff))}}
Absorption coefficient	0
Source term	(y[1/m])^2*0.251 *nojac(comp1.pellet_mid((UO2_grain_radius[1/m])^2*fission_rate_density))

Mass coefficient	0
Damping or mass coefficient	(y[1/m])^2*nojac(comp1.pellet_mid((UO2_grain_radius[1/m])^2))
Conservative flux convection coefficient	{0, 0}
Convection coefficient	{0, 0}
Conservative flux source	{0, 0}

SHAPE FUNCTIONS

Name	Shape function	Unit	Description	Shape frame	Selection
fg_grain_conc	Lagrange (Quadratic)	1/m^3	Dependent variable fg_grain_conc	Material	Domain 1

INITIAL VALUES

Settings	
Description	**Value**
Initial value for fg_grain_conc	0
Initial time derivative of fg_grain_conc	0

DIRICHLET BOUNDARY CONDITION 1

Settings	
Description	**Value**
Value on boundary	0
Prescribed value of fg_grain_conc	On
Apply reaction terms on	Individual dependent variables
Use weak constraints	Off

CUMULATIVE I RELEASED (PODE8)

DISTRIBUTED ODE 1

Settings	
Description	**Value**
Source term	I_net_release_rate
Damping or mass coefficient	1
Mass coefficient	0

SHAPE FUNCTIONS

Name	Shape function	Unit	Description	Shape frame	Selection
I_released	Discontinuous Lagrange (Quadratic)	1	Dependent variable I_released	Material	Point 4

INITIAL VALUES 1

Settings	
Description	**Value**
Initial value for I_released	0
Initial time derivative of I_released	0

I127 GRAIN DIFFUSION (I127_DIFF)

COEFFICIENT FORM PDE 1

Settings	
Description	**Value**
Diffusion coefficient	{{0, 0}, {0, (y[1/m])^2*nojac(comp1.pellet_mid(fg_diff_coeff))}}
Absorption coefficient	lambda_I127*(y[1/m])^2*comp1.pellet_mid((UO2_grain_radius[1/m])^2)
Source term	Yield_I127*(y[1/m])^2*comp1.pellet_mid((UO2_grain_radius[1/m])^2*fission_rate_density)
Mass coefficient	0
Damping or mass coefficient	(y[1/m])^2*comp1.pellet_mid((UO2_grain_radius[1/m])^2)
Conservative flux convection coefficient	{0, 0}
Convection coefficient	{0, 0}
Conservative flux source	{0, 0}

SHAPE FUNCTIONS

Name	Shape function	Unit	Description	Shape frame	Selection
I127_grain_conc	Lagrange (Quadratic)	1/m^3	Dependent variable I127_grain_conc	Material	Domain 1

INITIAL VALUES 1

Settings	
Description	**Value**
Initial value for I127_grain_conc	0
Initial time derivative of I127_grain_conc	0

DIRICHLET BOUNDARY CONDITION 1

Settings	
Description	**Value**
Value on boundary	0
Prescribed value of I127_grain_conc	On
Apply reaction terms on	Individual dependent variables
Use weak constraints	Off

I129 GRAIN DIFFUSION (I129_DIFF)

COEFFICIENT FORM PDE 1

Settings	
Description	**Value**
Diffusion coefficient	{{0, 0}, {0, (y[1/m])^2*nojac(comp1.pellet_mid(fg_diff_coeff))}}
Absorption coefficient	lambda_I129*(y[1/m])^2*comp1.pellet_mid((UO2_grain_radius[1/m])^2)
Source term	Yield_I129*(y[1/m])^2*comp1.pellet_mid((UO2_grain_radius[1/m])^2*fission_rate_density)
Mass coefficient	0
Damping or mass coefficient	(y[1/m])^2*comp1.pellet_mid((UO2_grain_radius[1/m])^2)
Conservative flux convection coefficient	{0, 0}
Convection coefficient	{0, 0}
Conservative flux source	{0, 0}

SHAPE FUNCTIONS

Name	Shape function	Unit	Description	Shape frame	Selection
I129_grain_conc	Lagrange (Quadratic)	1/m^3	Dependent variable I129_grain_conc	Material	Domain 1

INITIAL VALUES 1

Settings	
Description	**Value**
Initial value for I129_grain_conc	0
Initial time derivative of I129_grain_conc	0

DIRICHLET BOUNDARY CONDITION 1

Settings	
Description	**Value**
Value on boundary	0
Prescribed value of I129_grain_conc	On
Apply reaction terms on	Individual dependent variables
Use weak constraints	Off

I131 GRAIN DIFFUSION (I131_DIFF)

COEFFICIENT FORM PDE 1

Settings	
Description	**Value**
Diffusion coefficient	{{0, 0}, {0, (y[1/m])^2*nojac(comp1.pellet_mid(fg_diff_coeff))}}
Absorption coefficient	lambda_I131*(y[1/m])^2*comp1.pellet_mid((UO2_grain_radius[1/m])^2)
Source term	Yield_I131*(y[1/m])^2*comp1.pellet_mid((UO2_grain_radius[1/m])^2*fission_rate_density)
Mass coefficient	0
Damping or mass coefficient	(y[1/m])^2*comp1.pellet_mid((UO2_grain_radius[1/m])^2)
Conservative flux convection coefficient	{0, 0}
Convection coefficient	{0, 0}
Conservative flux source	{0, 0}

SHAPE FUNCTIONS

Name	Shape function	Unit	Description	Shape frame	Selection
I131_grain_conc	Lagrange (Quadratic)	1/m^3	Dependent variable I131_grain_conc	Material	Domain 1

INITIAL VALUES 1

Settings	
Description	**Value**
Initial value for I131_grain_conc	0
Initial time derivative of I131_grain_conc	0

DIRICHLET BOUNDARY CONDITION 1

Settings	
Description	**Value**
Value on boundary	0
Prescribed value of I131_grain_conc	On
Apply reaction terms on	Individual dependent variables
Use weak constraints	Off

I133 GRAIN DIFFUSION (I133_DIFF)

COEFFICIENT FORM PDE 1

Settings	
Description	**Value**
Diffusion coefficient	{{0, 0}, {0, (y[1/m])^2*nojac(comp1.pellet_mid(fg_diff_coeff))}}
Absorption coefficient	lambda_I133*(y[1/m])^2*comp1.pellet_mid((UO2_grain_radius[1/m])^2)
Source term	Yield_I133 *(y[1/m])^2*comp1.pellet_mid((UO2_grain_radius[1/m])^2*fission_rate_density)
Mass coefficient	0
Damping or mass coefficient	(y[1/m])^2*comp1.pellet_mid((UO2_grain_radius[1/m])^2)
Conservative flux convection coefficient	{0, 0}
Convection coefficient	{0, 0}
Conservative flux source	{0, 0}

SHAPE FUNCTIONS

Name	Shape function	Unit	Description	Shape frame	Selection
I133_grain_conc	Lagrange (Quadratic)	1/m^3	Dependent variable I133_grain_conc	Material	Domain 1

INITIAL VALUES 1

Settings	
Description	**Value**
Initial value for I133_grain_conc	0
Initial time derivative of I133_grain_conc	0

DIRICHLET BOUNDARY CONDITION 1

Settings	
Description	**Value**
Value on boundary	0

Prescribed value of I133_grain_conc	On
Apply reaction terms on	Individual dependent variables
Use weak constraints	Off

I127 PELLET SURFACE CONCENTRATION (PODE)

DISTRIBUTED ODE 1

Settings	
Description	**Value**
Source term	I127_release_at_gb*fg_release_multiplier - lambda_I127*I127_surf
Damping or mass coefficient	1
Mass coefficient	0

SHAPE FUNCTIONS

Name	Shape function	Unit	Description	Shape frame	Selection
I127_surf	Discontinuous Lagrange (Linear)	1/m^2	Dependent variable I127_surf	Material	Point 4

INITIAL VALUES 1

Settings	
Description	**Value**
Initial value for I127_surf	0
Initial time derivative of I127_surf	0

I129 PELLET SURFACE CONCENTRATION (PODE2)

DISTRIBUTED ODE 1

Settings	
Description	**Value**
Source term	I129_release_at_gb*fg_release_multiplier - lambda_I129*I129_surf
Damping or mass coefficient	1
Mass coefficient	0

SHAPE FUNCTIONS

Name	Shape function	Unit	Description	Shape frame	Selection
I129_surf	Discontinuous Lagrange (Linear)	1/m^2	Dependent variable I129_surf	Material	Point 4

INITIAL VALUES 1

Settings	
Description	**Value**
Initial value for I129_surf	0
Initial time derivative of I129_surf	0

I131PELLET SURFACE CONCENTRATION (PODE3)

DISTRIBUTED ODE 1

Settings	
Description	**Value**
Source term	I131_release_at_gb*fg_release_multiplier - lambda_I131*I131_surf
Damping or mass coefficient	1
Mass coefficient	0

SHAPE FUNCTIONS

Name	Shape function	Unit	Description	Shape frame	Selection
I131_surf	Discontinuous Lagrange (Linear)	1/m^2	Dependent variable I131_surf	Material	Point 4

INITIAL VALUES 1

Settings	
Description	**Value**
Initial value for I131_surf	0
Initial time derivative of I131_surf	0

I133 PELLET SURFACE CONCENTRATION (PODE4)

DISTRIBUTED ODE 1

Settings	
Description	**Value**
Source term	I133_release_at_gb*fg_release_multiplier - lambda_I133*I133_surf
Damping or mass coefficient	1
Mass coefficient	0

SHAPE FUNCTIONS

Name	Shape function	Unit	Description	Shape frame	Selection
I133_surf	Discontinuous Lagrange (Linear)	1/m^2	Dependent variable I133_surf	Material	Point 4

INITIAL VALUES 1

Settings	
Description	**Value**
Initial value for I133_surf	0
Initial time derivative of I133_surf	0

MESH 2

Mesh statistics	
Property	**Value**
Minimum element quality	0.005155
Average element quality	0.1319
Quadrilateral elements	338
Edge elements	78
Vertex elements	4

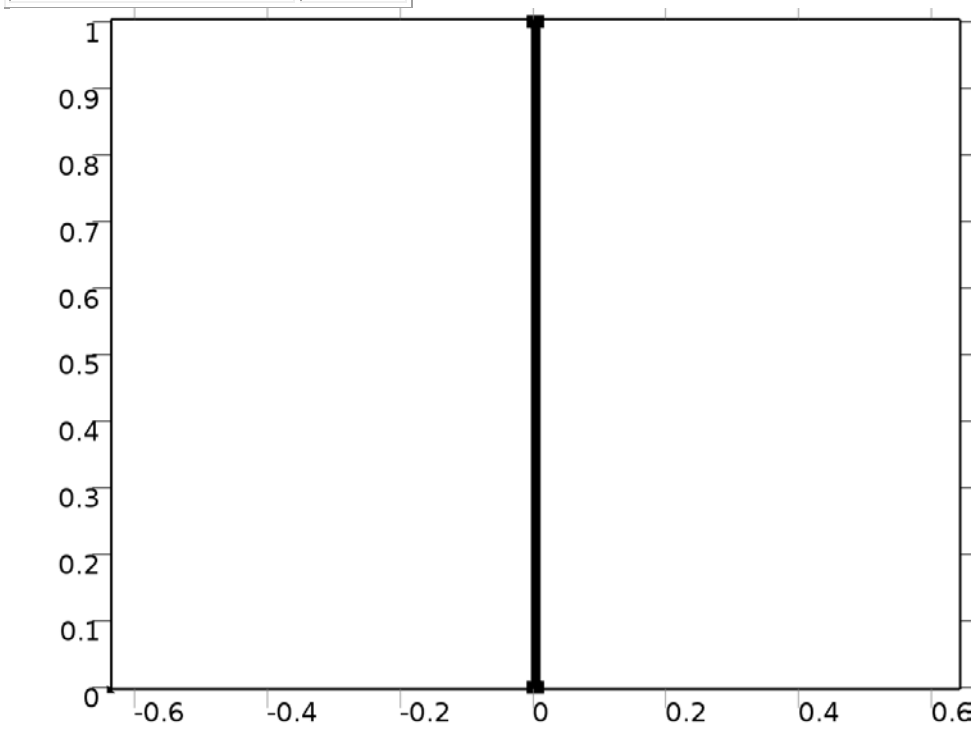

Mesh 2

COMPONENT 3

VARIABLES

GAP VARIABLES

Selection	
Geometric entity level	Domain
Selection	Domain 1

Name	Expression
gap_diffusion_coeff	0.0018583*sqrt(comp1.pellet_surface_avg(T[K^ - 3])^3*((1/M_He) + (1/M_I2)))/(p*omega_AB*sigma_AB^2)*1[cm^2/s*K^3]
I127_gap_release_rate	comp2.fg_surface_grain_boundary(I127_surf)/max(comp2.fg_surface_grain_boundary(sum_I), eps) *comp2.fg_surface_grain_boundary(I_net_release_rate)/element_length
I129_gap_release_rate	comp2.fg_surface_grain_boundary(I129_surf)/max(comp2.fg_surface_grain_boundary(sum_I), eps) *comp2.fg_surface_grain_boundary(I_net_release_rate)/element_length
I131_gap_release_rate	comp2.fg_surface_grain_boundary(I131_surf)/max(comp2.fg_surface_grain_boundary(sum_I), eps) *comp2.fg_surface_grain_boundary(I_net_release_rate)/element_length
I133_gap_release_rate	comp2.fg_surface_grain_boundary(I133_surf)/max(comp2.fg_surface_grain_boundary(sum_I), eps) *comp2.fg_surface_grain_boundary(I_net_release_rate)/element_length

CRACK SITE VARIABLES

Selection	
Geometric entity level	Boundary
Selection	Boundary 1

Name	Expression	Description
I_crack	2*gap_diffusion_coeff*(I127_gapx + I129_gapx + I131_gapx + I133_gapx)	
ZrI4_crack	0.25*I_crack*reaction	

CRACK GROWTH VARIABLES

Selection	
Geometric entity level	Entire model

Name	Expression
crack_initiation_flag	(crack_site(d_strain)>=critical_dstrain)
critical_dstrain	(CANLUB_thickness==0)*(-1.06E-3 + 0.677/ramp_burnup) + (CANLUB_thickness>0)*(ramp_burnup<=250)*((0.003105 + 0.503/ramp_burnup) + 0.0001) + (CANLUB_thickness>0)*(ramp_burnup>=500)*(-1.06E-3 + 0.677/ramp_burnup) + (CANLUB_thickness>0)*(ramp_burnup>250)*(ramp_burnup<500)*(((2 - ramp_burnup/250)*(0.003105 + 0.503/ramp_burnup + 0.0001)) + (((ramp_burnup/250) - 1)*(-1.06E-3 + 0.677/ramp_burnup)))

IG_growth_flag	crack_initiation_flag*abs(TG_growth_flag - 1)
K1	K_geo_factor*sheath_stress*(pi*crack_site(crack_length[m^ - 1]))^0.5
TG_growth_flag	flc1hs(K1[m^2/N] - K_scc, 0.0001)*(crack_site(crack_length)>crack_length_initial)
TG_growth_rate	max(eps, 3E-7*log(K1[m^2/N]/1E6)[m/s] - 1E-8[m/s])*TG_growth_mod
failure_flag	if(K1>=K1c_zircaloy||crack_length>=sheath_thickness, 1, 0)
saved	2E-6*log(K1[m^2/N])[m/s] - 2E-6[m/s]
K_geo_factor	(bundle_type==0)*if(F==1,geo_factor_Rt_20_ac_1(comp3.crack_site(crack_length)/sheath_thickness), 0) + if(F==0.2,geo_factor_Rt_20_ac_02(comp3.crack_site(crack_length)/sheath_thickness), 0) + if(F==0.6,geo_factor_Rt_20_ac_06(comp3.crack_site(crack_length)/sheath_thickness), 0) +(bundle_type==1)*if(F==1,geo_factor_Rt_15_ac_1(comp3.crack_site(crack_length)/sheath_thickness), 0) + if(F==0.2,geo_factor_Rt_15_ac_02(comp3.crack_site(crack_length)/sheath_thickness), 0) + if(F==0.6,geo_factor_Rt_15_ac_06(comp3.crack_site(crack_length)/sheath_thickness), 0)
IG_crack_length	(2*crack_vol/(pi*crack_radius))^0.5
crack_length	crack_length_initial + IG_crack_length + TG_crack_length
sheath_stress	min(zirc_yield(comp1.sheath_inside_surface_max(T)), comp1.sheath_inside_surface_max(solid.sp1))
strain_rate	comp1.sheath_inside_surface_max(ut/pellet_radius)*flc1hs(t[s^ - 1] - time1[s^ - 1], 0.001)

COMPONENT COUPLINGS

Coupling type	Maximum
Operator name	crack_site

Source selection	
Geometric entity level	Boundary
Selection	Boundary 1

GEOMETRY 3

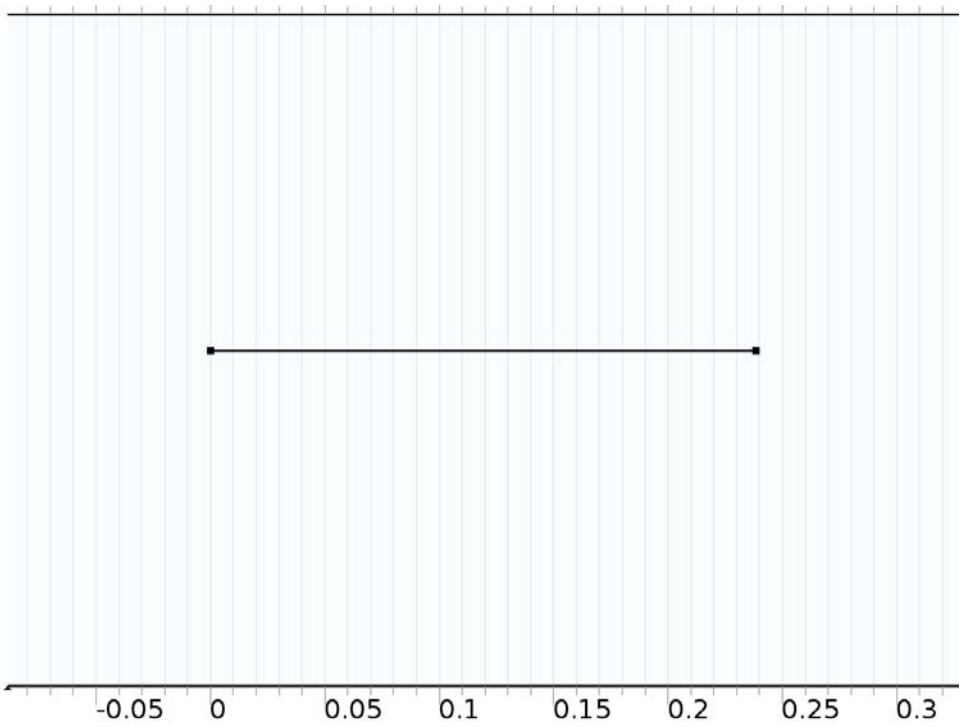

Units	
Length unit	m
Angular unit	deg

Geometry statistics	
Property	**Value**
Space dimension	1
Number of domains	1
Number of boundaries	2

GAP DIFFUSION I-127 (I127_GAP)

COEFFICIENT FORM PDE 1

Settings	
Description	**Value**
Diffusion coefficient	gap_diffusion_coeff
Absorption coefficient	lambda_I127 + absorption
Source term	I127_gap_release_rate
Mass coefficient	0
Damping or mass coefficient	1

Conservative flux convection coefficient	0
Convection coefficient	0
Conservative flux source	0

SHAPE FUNCTIONS

Name	Shape function	Unit	Description	Shape frame	Selection
I127_gap	Lagrange (Quadratic)	1/m	Dependent variable I127_gap	Material	Domain 1

INITIAL VALUES 1

Settings	
Description	**Value**
Initial value for I127_gap	0
Initial time derivative of I127_gap	0

DIRICHLET BOUNDARY CONDITION 1

Settings	
Description	**Value**
Value on boundary	0
Prescribed value of I127_gap	On
Apply reaction terms on	Individual dependent variables
Use weak constraints	Off

GAP DIFFUSION I-129 (I129_GAP)

COEFFICIENT FORM PDE 1

Settings	
Description	**Value**
Diffusion coefficient	gap_diffusion_coeff
Absorption coefficient	lambda_I129 + absorption
Source term	I129_gap_release_rate
Mass coefficient	0
Damping or mass coefficient	1
Conservative flux convection coefficient	0
Convection coefficient	0
Conservative flux source	0

SHAPE FUNCTIONS

Name	Shape function	Unit	Description	Shape frame	Selection
I129_gap	Lagrange (Quadratic)	1/m	Dependent variable I129_gap	Material	Domain 1

INITIAL VALUES 1

Settings	
Description	**Value**
Initial value for I129_gap	0
Initial time derivative of I129_gap	0

DIRICHLET BOUNDARY CONDITION 1

Settings	
Description	**Value**
Value on boundary	0
Prescribed value of I129_gap	On
Apply reaction terms on	Individual dependent variables
Use weak constraints	Off

GAP DIFFUSION I-131 (I131_GAP)

COEFFICIENT FORM PDE 1

Settings	
Description	**Value**
Diffusion coefficient	gap_diffusion_coeff
Absorption coefficient	lambda_I131 + absorption
Source term	I131_gap_release_rate
Mass coefficient	0
Damping or mass coefficient	1
Conservative flux convection coefficient	0
Convection coefficient	0
Conservative flux source	0

SHAPE FUNCTIONS

Name	Shape function	Unit	Description	Shape frame	Selection
I131_gap	Lagrange (Quadratic)	1/m	Dependent variable I131_gap	Material	Domain 1

INITIAL VALUES 1

Settings	
Description	**Value**
Initial value for I131_gap	0
Initial time derivative of I131_gap	0

DIRICHLET BOUNDARY CONDITION 1

Settings	
Description	**Value**
Value on boundary	0
Prescribed value of I131_gap	On
Apply reaction terms on	Individual dependent variables
Use weak constraints	Off

GAP DIFFUSION I-133 (I133_GAP)

COEFFICIENT FORM PDE 1

Settings	
Description	**Value**
Diffusion coefficient	gap_diffusion_coeff
Absorption coefficient	lambda_I133 + absorption
Source term	I133_gap_release_rate
Mass coefficient	0
Damping or mass coefficient	1
Conservative flux convection coefficient	0
Convection coefficient	0
Conservative flux source	0

SHAPE FUNCTIONS

Name	Shape function	Unit	Description	Shape frame	Selection
I133_gap	Lagrange (Quadratic)	1/m	Dependent variable I133_gap	Material	Domain 1

INITIAL VALUES 1

Settings	
Description	**Value**
Initial value for I133_gap	0
Initial time derivative of I133_gap	0

DIRICHLET BOUNDARY CONDITION 1

Settings	
Description	**Value**
Value on boundary	0
Prescribed value of I133_gap	On
Apply reaction terms on	Individual dependent variables
Use weak constraints	Off

IG CRACK VOLUME (CRACK_VOL)

DISTRIBUTED ODE 1

Settings	
Description	**Value**
Source term	(M_Zr/(rho_Zr*N_avogadro))*crack_site(ZrI4_crack)/n_cracks*IG_growth_flag
Damping or mass coefficient	1
Mass coefficient	0

SHAPE FUNCTIONS

Name	Shape function	Unit	Description	Shape frame	Selection
crack_vol	Discontinuous Lagrange (Linear)	m^3	Dependent variable crack_vol	Material	Boundary 1

INITIAL VALUES 1

Settings	
Description	**Value**
Initial value for crack_vol	crack_length_initial
Initial time derivative of crack_vol	0

TG CRACK LENGTH (TG_CRACK_LENGTH)

DISTRIBUTED ODE 1

Settings	
Description	**Value**
Source term	TG_growth_flag*TG_growth_rate
Damping or mass coefficient	1
Mass coefficient	0

SHAPE FUNCTIONS

Name	Shape function	Unit	Description	Shape frame	Selection
TG_crack_length	Discontinuous Lagrange (Linear)	m	Dependent variable TG_crack_length	Material	Boundary 1

INITIAL VALUES 1

Settings	
Description	**Value**
Initial value for TG_crack_length	0
Initial time derivative of TG_crack_length	0

D_STRAIN (BODE2)

DISTRIBUTED ODE 1

Settings	
Description	**Value**
Source term	strain_rate
Damping or mass coefficient	1
Mass coefficient	0

SHAPE FUNCTIONS

Name	Shape function	Unit	Description	Shape frame	Selection
d_strain	Discontinuous Lagrange (Linear)	1	Dependent variable d_strain	Material	Boundary 1

INITIAL VALUES 1

SETTINGS

Settings	
Description	**Value**
Initial value for d_strain	0.00001
Initial time derivative of d_strain	0

MESH 3

Mesh statistics	
Property	**Value**
Minimum element quality	1.0
Average element quality	1.0
Edge elements	25
Vertex elements	2

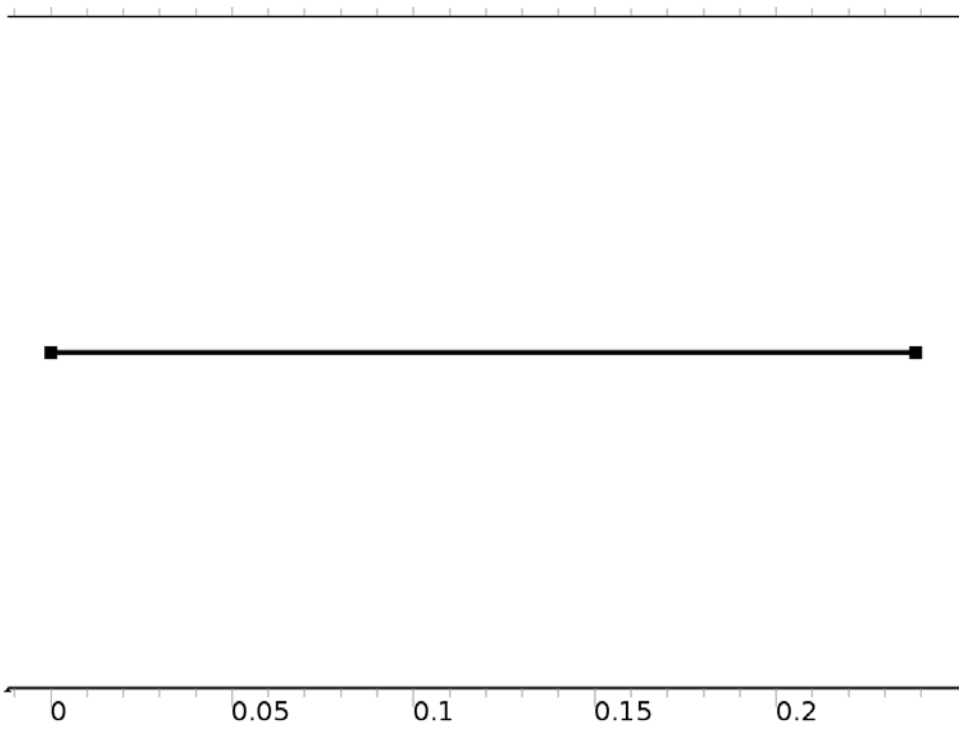

STUDY 1

TIME DEPENDENT

Times: 0 range(timestep_range1_start,timestep_range1_size,timestep_range1_end) range(timestep_range2_start,timestep_range2_size,timestep_range2_end) range(timestep_range3_start,timestep_range3_size,timestep_range3_end) range(timestep_range4_start,timestep_range4_size,timestep_range4_end) t_max

DIRECT (DDEF)

General	
Name	**Value**
Solver	PARDISO
Multithreaded forward and backward solve	On

FULLY COUPLED 1 (FC1)

General	
Name	**Value**
Linear solver	Direct

Method and termination	
Name	**Value**
Nonlinear method	Automatic (Newton)
Initial damping factor	solver_initial_damping_factor

Minimum damping factor	solver_initial_damping_factor
Restriction for step-size update	solver_damping_growth_rate
Use recovery damping factor	Off

STOP CONDITION 1 (ST1)

Stop events	
Name	**Value**
Implicit event	{comp1.ev3.impl1.event, comp1.ev3.impl2.event}